



UNIVERSIDAD
NACIONAL
DE COLOMBIA

Modelamiento de la adsorción de gases del proceso de Acoplamiento Oxidativo de Metano (OCM) sobre tamices moleculares de zeolita X

Cristian Camilo Rodriguez Paez

Universidad Nacional de Colombia
Facultad de Ingeniería
Departamento de Ingeniería Química y Ambiental
Bogotá, Colombia
2019



UNIVERSIDAD
NACIONAL
DE COLOMBIA

Gas Adsorption Modelling of the Oxidative Coupling of Methane (OCM) Process on Zeolite X Molecular Sieves

Cristian Camilo Rodriguez Paez

Universidad Nacional de Colombia
Facultad de Ingeniería
Departamento de Ingeniería Química y Ambiental
Bogotá, Colombia
2019

Modelamiento de la adsorción de gases del proceso de Acoplamiento Oxidativo de Metano (OCM) sobre tamices moleculares de zeolita X

Cristian Camilo Rodriguez Paez

Tesis presentada como requisito parcial para optar al título de
Magister en Ingeniería – Ingeniería Química

Director:

Alvaro Orjuela Londoño, Ph.D.

Codirector:

Gerardo Rodriguez Niño, Ph.D.

Línea de investigación:

Modelamiento y Simulación.

Grupo de Investigación de Procesos Químicos y Bioquímicos

Universidad Nacional de Colombia
Facultad de Ingeniería
Departamento de Ingeniería Química y Ambiental
Bogotá, Colombia
2019

Education is the great engine of personal development- It us through education that the daughter of a peasant can become a doctor, that the son of a mineworker can become the head of the mine, that the child of farm workers can become the president of a great nation.

Nelson Mandela

Acknowledgements

I would like to thank the support received during the development of this work to:

Alvaro Orjuela Londoño for allow me to be part of his work group, for his support and accurate advice.

Gerardo Rodriguez Niño for his willingness and support at opportune moments.

Karen Giovanna Bastidas for her unconditional friendship, patience and support in good and difficult times. Thank kogui.

Daniel Alejandro Jaimes for his support and good group work in the master courses.

The National University of Colombia for its academic and financial support, through its teaching staff and the "Auxiliary Teaching Scholarship" program of the Department of Chemical and Environmental Engineering.

EU CELAC R&I funding agencies through the ERANet-LAC 2ns Joint Call on Research and Innovation with the project "Bio-Empowered Oxidative Coupling of Methane (OCM) Process - BIOCM"

The Technische Universität Berlin, for the support for the development of this work.

To Professor Jens-Uwe Repke, to Doctors Hamid Reza Godini and Erik Esche and to PhD student Alberto Penteado for their great contributions to the development of this work.

Abstract

In this work was studied the modeling of the adsorption of effluent gases from the methane oxidative coupling process (OCM) on CaX zeolite for the separation of ethylene. To describe the adsorption process, a mathematical model was implemented within the Aspen Adsorption software based on Mass, Energy and Momentum balances, and the Linear Driving Force adsorption rate model. The transport parameters were adjusted from dynamic experimental data in order to validate the proposed mathematical model, to be used in the design of a pressure swing adsorption system (PSA) on an industrial scale. The PSA system can be an alternative to cryogenic distillation for the separation of methane because the methane is not adsorbed on CaX zeolite, and also the zeolite CaX presents selectivity for ethane and ethylene. The ethylene purification process was carried out with cryogenic distillation columns. However, the substitution of the demethanizer unit with a PSA system resulted in an energy saving of 30% and a reduction in utility costs of 18% compared to the traditional cryogenic distillation process.

Keywords: Pressure swing adsorption, Oxidative Coupling of Methane, Cryogenic Distillation, Breakthrough Curve, and Ethylene Separation.

Resumen

En este trabajo se estudió el modelamiento de la adsorción de gases efluentes del proceso de acoplamiento oxidativo de metano (OCM) sobre zeolita CaX para la separación de etileno. Para describir el proceso de adsorción un modelo matemático fue implementado dentro del software Aspen Adsorption basado en los balances de Masa, Energía y Momentum, y el modelo de velocidad de adsorción de fuerza impulsora lineal. Los parámetros de transporte fueron ajustados a partir de datos experimentales dinámicos con el fin de validar el modelo matemático propuesto, para ser utilizado en el diseño de un sistema de adsorción por oscilación de presión (PSA) a escala industrial. El sistema de PSA puede ser una alternativa a la destilación criogénica para la separación de metano debido a que la zeolita CaX no adsorbe metano, y además presenta selectividad por el etano y etileno. El proceso de purificación de etileno se llevó a cabo con columnas de destilación criogénica. Sin embargo, al sustituir la unidad demetanizadora por un sistema PSA se presentó un ahorro de energía del 30% y una reducción de costos de utilidad del 18% en comparación con el proceso de destilación criogénica tradicional.

Palabras clave: Adsorción por oscilación de presión, oxidación acoplada de metano, destilación criogénica, curva de ruptura, separación de etileno.

Contents

	Pág.
1. Chapter One: Introduction	3
1.1 Relevance and Motivation	3
1.2 Oxidative Coupling of Methane Process.....	6
1.2.1 Reaction section	7
1.2.2 CO ₂ removal section	10
1.2.3 Ethylene purification section	10
1.3 Alternative separation in the OCM process.....	11
1.4 Project description.....	13
2. Chapter Two: Fundamental concepts	14
2.1 Adsorption	14
2.1.1 Steric effects.....	14
2.1.2 Adsorption equilibria	15
2.1.3 Adsorption kinetics.....	17
2.2 Adsorbent materials	19
2.2.1 Alumina	20
2.2.2 Silica gel	21
2.2.3 Activated carbon.....	21
2.2.4 Zeolites	22
2.3 Adsorption processes.....	27
2.3.1 Breakthrough curves.....	28
2.3.2 Pressure swing Adsorption	31
3. Chapter three: Modeling of pressure swing adsorption process	37
3.1 Mathematical model	38
3.1.1 Adsorption equilibrium model.....	39
3.1.2 Mass transport model	41
3.1.3 Energy balance.....	43
3.1.4 Momentum balance	48
3.1.5 Mass transfer rate.....	48
3.1.6 Model solution.....	49
3.2 Model validation	52
3.3 Pressure Swing Adsorption (PSA) process operation.....	61
3.3.1 Feed composition	62
3.3.2 Temperature	63
3.3.3 Pressure	63

3.3.4 Size	63
4. Chapter four: Simulation process of the downstream section in the OCM process	69
4.1 Pressure swing adsorption process.....	69
4.1.1 Implementation in Aspen Adsorption®	70
4.1.2 Separation of methane from ethane/ethylene mixture.....	72
Parametric study	75
4.1.3 Purification of ethylene	84
4.2 Comparison with conventional process separation.....	92
4.2.1 Separation of ethylene using demethanizer and deethanizer columns	92
4.2.2 Energy consumption.....	96
4.2.3 Preliminary economic evaluation	97
5. Conclusions and perspectives	109
5.1 Conclusions	109
5.2 Perspectives	110

List of Figures

	Pág.
Figure 1. Relative energy comparison by different technologies [6].	5
Figure 2. General flow diagram for the OCM process [9].	7
Figure 3. OCM reaction scheme [11].	7
Figure 4. General flow diagram of absorption process for CO ₂ removal [12].	10
Figure 5. Separation factor for the ethylene/methane mixture in different adsorbents [14].	12
Figure 6. Molecular sieving effect for linear and branched paraffins in 5A zeolite [19].	15
Figure 7. The five types of van der Waals adsorption isotherms [22].	16
Figure 8. Schematic representation of the three transfer mass resistance [24].	18
Figure 9. Comparison of pore size in different types of zeolites [29].	23
Figure 10. Framework structure of the zeolite LTA [32].	24
Figure 11. Framework structure of the zeolite FAU [32].	25
Figure 12. Cation sites in FAU zeolite [34].	26
Figure 13. Adsorption selectivity for C ₂ olefins compared with methane over zeolite CaX at 298 K and different pressures [35].	27
Figure 14. Typical adsorbate concentration profile along a packing bed during adsorption process [37].	28
Figure 15. The mass transfer zone moving along the bed [38].	30
Figure 16. Breakthrough curve for (a) narrow and (b) wide MTZ [38].	30
Figure 17. Adsorbent's working capacity in the PSA process. Adapted from [39].	32
Figure 18. Pressure swing adsorption scheme.	34
Figure 19. Pseudo-homogeneous control volume [44].	38
Figure 20. Adsorption isotherms for CH ₄ , C ₂ H ₄ and C ₂ H ₆ on CaX zeolite at 298 K [45].	41
Figure 21. Control volume for mass material balance.	41
Figure 22. Control volume for gas phase energy balance	44
Figure 23. Control volume for solid phase energy balance	46
Figure 24. Representation of a fixed-bed into a mesh of discrete points.	50
Figure 25. Breakthrough curves evaluated with different nodes: (a) 20 nodes; (b) 40 nodes; (c) 60 nodes and (d) 80 nodes. %E: Percentage of error.	51
Figure 26. Representation of initial and boundary conditions in a fixed-bed.	52
Figure 27. Breakthrough curves of methane, ethane and ethylene at 308 K [16].	54
Figure 28. Electrostatic maps of ethylene, ethane and methane. Electrostatic maps taken from [55].	55

Figure 29. Individual mass transfer resistances as a percentage of the overall resistance.	57
Figure 30. Ethane breakthrough curve at 303.15 K and 2 bar.	59
Figure 31. Methane breakthrough curves at 303.15 K: a) 2 bar and b) 5 bar.	61
Figure 32. Schematic representation of LUB using a diameter of 2 m and a height of 9m. Adapted from Thomas and Barry Crittenden [61]	64
Figure 33. General procedure for simulating PSA columns in Aspen Adsorption	71
Figure 34. Steps used in the PSA cycle for the separation of methane from C2 components	72
Figure 35. Step 1: Bed pressurization at 8.8 bar.....	73
Figure 36. Step 2: Separation of methane from olefin mixture by adsorption of ethane and ethylene.	74
Figure 37. Step 3: Blowdown of the bed	74
Figure 38. Step 4: Desorption of strongly adsorbed components at atmospheric pressure.	75
Figure 39. Different feed flows evaluated in the adsorption time proposed. a) 20 mol/s; b) 40 mol/s; c) 60 mol/s and d) 80 mol/s.....	76
Figure 40. Olefins recovery and purity with respect to ratio of pressurization time to adsorption time. a) ethylene; b) ethane.	78
Figure 41. Methane recovery and purity with respect to the ratio of pressurization time to adsorption time.	78
Figure 42. Performance of methane separation (a), and ethane recovery (b) in PSA column at different purge flows.	79
Figure 43. Evaluation of performance of PSA column using different purge flows. a) Results on methane separation performance; b) Results on ethylene separation performance.....	81
Figure 44. Separation performance of PSA column using a feed flow of 60 mol/s. a) Results on methane separation performance; b) Results on ethylene separation performance.....	81
Figure 45. Structure of PSA cycle (cycle 31) and time schedule.....	83
Figure 46. Temperature profile in the packed bed of CaX zeolite during PSA process ...	83
Figure 47. Liquid-vapor equilibria of Methane-Ethylene system at 186.14 K.....	85
Figure 48. Alternative sequences for the separation of four components [68].....	86
Figure 49. Representation of sequence 3 for ethylene separation	87
Figure 50. General flow diagram for the downstream section	91
Figure 51. Sequence of separation established for traditional separation of ethylene.	93
Figure 52. Process diagram of traditional cryogenic distillation for ethylene separation ..	95
Figure 53. Performance of the separation schemes evaluated	97
Figure 54. Global ethylene prices [77]	105
Figure 55. Comparison of the total annualized cost and the sale price of ethylene in the different markets for the evaluated processes. US: United States; NEW: North west of Europe; and Asia.	107

List of Tables

Pág.

Table 1. Distribution of ethylene consumption according to final uses at 2016 (in %) [2] ...3	
Table 2. Ethylene requirements for polymer application.4	
Table 3. Reactions considered in the kinetic model [5, 10].8	
Table 4. Kinetic parameters of the OCM kinetic model [11].9	
Table 5. Typical column specifications in the separation of OCM gases [3].11	
Table 6. Typical characteristics of γ -alumina [23].20	
Table 7. Typical characteristics of Silica gel [23].21	
Table 8. Typical characteristics of Activated Carbon [23].22	
Table 9. Effect of cation exchange on diffusivity in Zeolite 5A for different gases [30]25	
Table 10. Elementary Steps [36].33	
Table 11. Description of Skarstrom cycle35	
Table 12. Adsorption equilibrium and kinetic parameters of OCM gases on CaX zeolite .40	
Table 13. Reported column specifications on the breakthrough experiments of OCM gases using CaX zeolite52	
Table 14. Adsorption equilibrium and kinetic parameters for PSA simulation using CaX zeolite.....54	
Table 15. Maximum adsorption capacity for CaX zeolite at 1.01325 bar.57	
Table 16. Column specifications for column fixed bed using CaX zeolite58	
Table 17. Adsorption condition for ethane breakthrough curve.....58	
Table 18. Adsorption equilibrium and kinetic parameters obtained from ethane breakthrough curve.59	
Table 19. Adsorption condition for methane breakthrough curve at 2 bar.60	
Table 20. Adsorption equilibrium and kinetic parameters obtained from methane breakthrough curves.....61	
Table 21. Molar composition for OCM effluent gases based on Stansch Reaction.62	
Table 22. Commercial flow and molar compositions.....62	
Table 23. Percentage of unused bed.64	
Table 24. Maximum allowable stress [64].66	
Table 25. Column and adsorbent characteristics.....66	
Table 26. Evaluation of the adsorption time in the bed regeneration process.77	
Table 27. Simulation conditions of PSA unit at different purge flows79	
Table 28. Ethylene purity and recovery for different conditions using CaX zeolite.80	

Table 29. Operating parameter used in PSA cycle for methane separation and ethylene recovery.....	82
Table 30. Results obtained from simulation based on operating parameters proposed...	84
Table 31. Boiling temperatures of OCM gases.....	86
Table 32. Heat duty of reboiler heating and condenser cooling.....	87
Table 33. Operating parameters for Shortcut model	88
Table 34. Results obtained from shortcut simulations in Aspen Plus	89
Table 35. Operating parameter used in RADFRAC model.....	89
Table 36. Results obtained from rigorous model for deethanizer column	90
Table 37. Mass balance for separation process proposed	91
Table 38. Energy and heat requirements for the PSA + Cryogenic distillation scheme ...	92
Table 39. Operating parameters used in shortcut model for traditional separation scheme	93
Table 40. Initial parameters for distillation design in RADFRAC model	94
Table 41. Operating parameter used to simulation of ethylene separation.....	94
Table 42. Results obtained from rigorous simulation for deethanizer column.....	95
Table 43. Mass balance for traditional separation scheme.....	95
Table 44. Energy and heat requirements for the traditional Cryogenic Distillation scheme	96
Table 45. Data for estimation cost of column packing	98
Table 46. Cost of a PSA column.....	99
Table 47. Equipment cost results obtained by Aspen Economic Analyzer	99
Table 48. CE index for the years involve in this study	99
Table 49. Actualization cost for separation alternatives proposed.....	100
Table 50. Multipliers for installed costs of process equipment from the ethylene separation.....	100
Table 51. Total capital cost for separation schemes proposed.....	101
Table 52. Utility cost coefficients.....	102
Table 53. Coefficient of reversible performance at different temperatures	102
Table 54. Refrigerant cost at different temperature.....	102
Table 55. Utilities required to operation of equipment in the ethylene separation in 1 h.	103
Table 56. Annualized cost of utilities.....	104
Table 57. Total annualized cost for separation schemes proposed.....	105
Table 58. Ethylene sale price in the US, EU and Asia markets	106

List of Symbols and Abbreviations

Symbols with Latin letters

Symbol	Term	SI Unit	Definition
A	Area	m^2	
b	Constant of Langmuir equation	$\frac{1}{bar}$	Eq. 18
C	Gas concentration	$kmol/m^3$	
C_p	Heat Capacity at constant pressure	$J kmol^{-1} K^{-1}$	
C_p	Heat Capacity at constant volume	$J kmol^{-1} K^{-1}$	
D	Diameter	m^2	
D_{az}	Axial dispersion	$\frac{m^2}{s}$	Eq. 30
D_{eff}	Effective diffusion	$\frac{m^2}{s}$	Eq. 58
D_k	Knudsen diffusion	$\frac{m^2}{s}$	
D_m	Molecular diffusion	$\frac{m^2}{s}$	Eq. 65
e	Specific energy	$\frac{J}{m^3}$	
E_a	Activation energy	$\frac{J}{kmol}$	
H	Height	m	
H_w	Heat transfer coefficient between gas phase and wall column	W/m^2K^{-1}	Eq. 39
HTC	Heat transfer coefficient between gas phase and adsorbent material	W/m^2K^{-1}	Eq. 51
j	Colburn factor		Eq. 52
K	Thermal conductivity	W/m^1K^{-1}	
K_0	Pre-exponential factor for Arrhe	$m s^{-1}$	
k_f	Film mass transfer coefficient	m/s	Eq. 57
M_w	Molecular weight	$Kg/kmol$	
MTC	Mass transfer coefficient	s^{-1}	Eq. 12
P	Pressure	bar	
q	Equilibrium loading	$Kmol/kg$	Eq. 7
q_m	Maximum adsorption capacity	$Kmol/kg$	
Q_{gs}	Heat flow from solid to gas phase	W	Eq. 32
Q_{gw}	Heat flow from the gas to wall column	W	Eq. 33
Q_{ext}	Heat flow to the outside	W	
R	Gas universal constant	$J kmol^{-1} K^{-1}$	
Re	Reynolds number		
Sc	Schmitd number		Eq. 64
Sh	Sherwood number		Eq. 63
t	Time	s	

Symbol	Term	SI Unit	Definition
T	Temperature	°C or K	
t_b	Breakthrough time	s	Eq. 15
t_p	Thickness for pressure effect	M or in	Eq. 72
v_s	Superficial velocity	m/s	
Y	Molar fraction		
Z	Axial coordinate	m	
ΔH_{ads}	Heat of adsorption	J kmol ⁻¹	
\bar{K}_H	Henry's coefficient		Eq. 60

Symbols with Greek letters

Símbolo	Término	Unidad SI	Definición
ε	Interparticle porosity	$\frac{m^3(pore)}{m^3(bed)}$	
μ	Dynamic viscosity	N s m ⁻²	
ρ	Molar density	kmol/m ³	
Δ	Difference		
σ_{AB}	Collision diameter	Å	Eq. 67

Subscripts

Subscript	Term
B	Bed
C	Crystal - micropore
0	Initial
g	gas
i	Component i
p	Particle
S	Solid
W	Wall

Superscripts

Superscripts	Term
*	Symmetrical point

Abbreviations

Abbreviation	Term
ADS	Adsorption
CD	Cryogenic distillation
LDF	Linear driving force
OCM	Oxidative coupling of methane
PDE	Partial differential equation
PSA	Pressure swing adsorption

PROLOGUE

The manuscript is constructed in four main chapters and the conclusions sections. Chapter one is a brief introduction and description of the oxidative coupling of the methane process, as well as explains the aim of this study.

Chapter two includes fundamental concepts of adsorption, adsorbent materials, and dynamic processes. This helps to provide the required tools that the reader will require to understand the analysis carried out in the following sections.

Chapter three developed the mathematical models required to describe the performance of a PSA system. The constructed models are simulated and validated using experimental data. Once validated, the computer model is explored to assess the effect of the different operating variables of the PSA system in the separation of OCM gases.

Chapter four describes a methodology to define the operating conditions of the PSA system to achieve the separation of the OCM gases. A comparison between different separation alternatives (PSA, and traditional cryogenic distillation) was also performed. In the final section, conclusions and recommendations for further studies are included

1. Chapter One: Introduction

1.1 Relevance and Motivation

Ethylene is a main building block in the petrochemical industry with a large global demand. According to recent data, approximately 146 million of tons were produced in 2017 [1]. Ethylene is mainly used as feedstock for polymers, because it is suitable for films production, blow and injection molding, and for coatings. The distribution of ethylene consumption according to the final use is presented in Table 1. As observed, around 60% is used for polyethylene products, and the remaining is used to synthesize monomers and other chemicals, such as ethylene oxide, ethylene dichloride (precursor of vinyl chloride monomer) and ethyl benzene (precursor of styrene).

Table 1. Distribution of ethylene consumption according to final uses at 2016 (in %) [2]

Use	World
Polymerization to low-density polyethylene (LDPE)	19
Polymerization to linear low-density polyethylene (LLDPE)	60 14
Polymerization to high-density polyethylene (HDPE)	27
Ethylene Oxide/Ethylene Glycol	15
Ethylene Dichloride	10
Ethyl Benzene/Styrene Monomer	6
Others	9

The large-scale ethylene production is carried out by different processes, but the most widely used is the steam cracking of hydrocarbons. Cracking occurs in a fired tubular reactor where the hydrocarbons feedstock (e.g. naphtha) is cracked into smaller molecules at high temperatures (500 to 875 °C). The major products of this process are ethylene, ethane, di-olefins and other compounds [2]. Another source of ethylene is the Fluidized Catalytic Cracking (FCC), where ethylene is recovered from FCC off-gas. However, a major limitation of this process is the simultaneous production of nitrogen oxides that can generate

explosive compounds. Alternatively, there are new processes being developed in recent years. In the mid-1990s UOP identified the possibility to obtain ethylene from methanol, and since the early 2010s different Chinese companies have implemented industrial facilities using a similar technology. Using a different approach, Brazchem built a 200 kt/yr. commercial plant for green ethylene via dehydration of fermentation-based ethanol. Also, newer routes have been explored, including dehydrogenation of ethane, and methane coupling either oxidatively or non-oxidatively [2].

Specifically, the oxidative coupling of methane (OCM) as alternative route for ethylene has been widely studied owing to its potential to exploit low-cost raw materials such as natural gas, shale gas and biogas. Nevertheless, a major drawback of the OCM process is that the conversion of methane in the reactor is only about 30% [3]. This creates a major challenge for the downstream separation taking into account the large amount of unreacted methane, and the high content of other gases including ethylene, ethane, carbon dioxide, carbon monoxide, hydrogen, and other hydrocarbons.

As the major application of ethylene is for polymers production, high purity grades are required. The presence of minor impurities in the ethylene monomer creates serious difficulties in the polymerization process. In that regard, the separation operations required in an OCM process must satisfy the mentioned requirements to deliver a product under specifications described in Table 2.

Table 2. Ethylene requirements for polymer application.

Composition	Polymer Grade
Ethylene	> 99.9 % vol.
Carbon Monoxide	< 5 vol. ppm
Oxygen	< 2 vol. ppm
Carbon Dioxide	< 6 vol. ppm
Sulphur	< 3 vol. ppm
Hydrogen	< 5 vol. ppm
Acetylene	< 5 vol. ppm
C3 and heavier	< 5 vol. ppm
Methane + Ethane	< 1000 vol. ppm
Water	< 5 vol. ppm
Methanol	< 3 vol. ppm

Data obtained from Repsol [4]

Traditionally ethylene purification in the different industrial processes is done through cryogenic distillation. This separation process operates under high pressures ($P > 30$ bar), low temperatures (173 - 273 K), and with large reflux ratio. Also, the distillation columns require a large number of separation plates, as well as a high refrigeration capacity. Thus, this represents major limitations when used as downstream separation alternative for the OCM process due to the low ethylene concentrations. For this reason, when incorporating cryogenic distillation, the energy consumption constitutes almost 97% of utility cost in the separation section of the OCM process [5], limiting its industrialization.

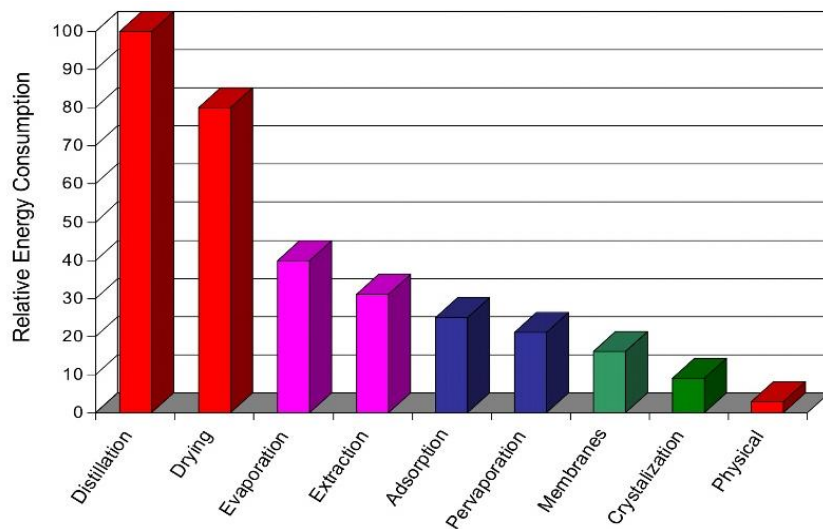


Figure 1. Relative energy comparison by different technologies [6].

Different alternatives have been proposed to improve energy efficiency in separation operations to replace distillation (Figure 1). Among these alternatives, swing adsorption (SA) looks promising for implementation in the OCM process. During gas phase SA, a suitable adsorbent is used to selectively separate the components of a gas stream. The different gases are adsorbed at a different extent on the surface of the active material, allowing the selective separation of the different components in the gas phase. This process is inherently batch because the surface of the solid gets saturated with the adsorbed gases, thus the adsorbent material needs to be regenerated using a desorption process. This process can be carried out by changes of temperature (TSA) or pressure (PSA). In this last case, the operation involves cycles of high and low pressures because the adsorption is favored at high pressures and desorption is promoted at lower pressures. The adsorbents

are packed within suitable columns that operate simultaneously, doing the adsorption and desorption cycles in parallel columns. Thus, in the PSA process, not only the adsorbent materials and the operating conditions are fundamental, but also the operating policies during the adsorption and desorption cycles.

Due to the complexity of the effluent gas mixture from the OCM process, the implementation of a PSA separation process is far from a straightforward task. Once a suitable adsorbent is engineered, there is need for developing a feasibility assessment involving the study of: adsorbents selectivity and kinetic performance, stability of the adsorbent materials, adsorption-desorption cycling performance, energy consumption, operations scheduling, and optimization of the operating conditions, among others.

In this regard, this work is mainly focused on the design and assessment of the PSA process in the separation of effluent gases from an OCM process. An exploration on the suitable adsorbent materials for the separation was carried out, and the corresponding equilibrium and kinetic models were validated to use them as inputs in the PSA modeling. Then, a PSA model was implemented in a commercial software (i.e. Aspen Adsorption), including the adsorption and desorption cycles and the corresponding operating policies. Finally, a preliminary economic assessment for the implementation of a PSA system within an OCM process was carried out.

1.2 Oxidative Coupling of Methane Process

The oxidative coupling of methane (OCM) has been investigated for over 40 years as an alternative route for ethylene production. This chemical route has the potential to effectively exploit and upgrade widely available natural and shale gas. In comparison with other traditional routes, the OCM process requires less energy and reduces the emission of greenhouse gases. Despite its economic potential, and the recent implementation of an OCM demonstration plant by Siluria Technologies and Braskem, there is still need to overcome different technical drawbacks. The main limiting issues of the OCM process are related to the low conversion of methane into ethylene, and the high energy consumption required in the downstream processing [7, 8]. A simplified scheme of the OCM process is presented in Figure 2, and as observed, it can be divided in three main sections: reaction,

CO₂ removal, and main ethylene purification. A brief description of each part is presented in the following sections.

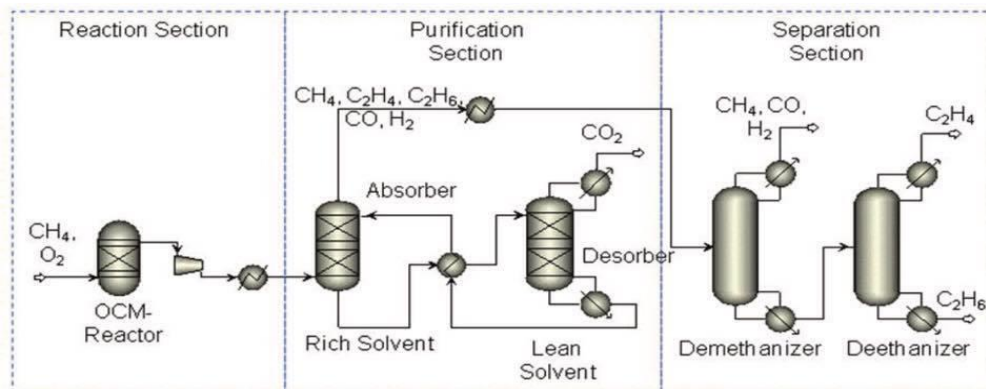


Figure 2. General flow diagram for the OCM process [9].

1.2.1 Reaction section

The OCM reaction was first discovered by Keller and Bhasin [10], when using several metal oxides for the selective synthesis of ethylene. As observed in Figure 3, the OCM process involves a complex system of heterogeneously catalyzed and non-catalytic reactions [11]. The process proceeds through a partial oxidation of methane at high temperatures and low pressure. The concentrations of oxygen in the mixture has to be tuned in order to ensure an adequate equilibrium among combustion products, ethylene selectivity, and methane conversion. Low oxygen concentration is used in the feed stream to achieve a high ethylene selectivity with reduced side combustion; however, conversions are low. In contrast, when high oxygen concentration is fed to the OCM reactor, the reaction reaches high methane conversion. However, there is an increase in partial and total oxidation products and consequently, a low ethylene selectivity.

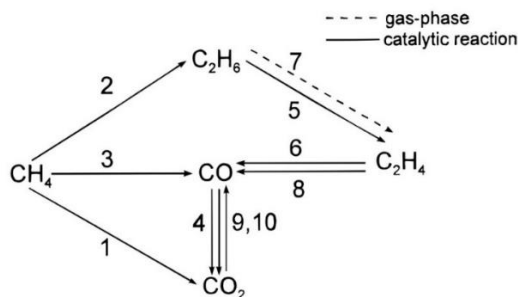


Figure 3. OCM reaction scheme [11].

A kinetic model for the OCM has been recently proposed [5, 10]. As observed in Figure 3, this model considers three primary reactions and seven consecutive steps. First, methane is converted into ethane by oxidative coupling of methane, and then sequentially transformed into ethylene, either catalytically or thermally promoted in the gas phase. In parallel, methane can be oxidized into carbon monoxide and carbon dioxide. At the same time, produced ethylene can react with oxygen or water to produce carbon monoxide by ethylene oxidation or ethylene reforming, respectively. Other simultaneous reaction occurs when carbon monoxide reacts with oxygen to produce carbon dioxide, but this reaction can occur in both directions. All stoichiometric equations proposed in the kinetic study are summarized in **Table 3**. The corresponding rate equations that describe the previous reaction system are presented in Equations 1 to 6:

Table 3. Reactions considered in the kinetic model [5, 10].

Reaction	Reaction number (i)
$CH_4 + 2O_2 \rightarrow CO_2 + 2H_2O$	1
$2CH_4 + \frac{1}{2}O_2 \rightarrow C_2H_6 + H_2O$	2
$CH_4 + O_2 \rightarrow CO + H_2O + H_2$	3
$CO + \frac{1}{2}O_2 \rightarrow CO_2$	4
$C_2H_6 + \frac{1}{2}O_2 \rightarrow C_2H_4 + H_2O$	5
$C_2H_4 + 2O_2 \rightarrow 2CO + 2H_2O$	6
$C_2H_6 \rightarrow C_2H_4 + H_2$	7
$C_2H_4 + 2H_2O \rightarrow 2CO + 4H_2$	8
$CO + H_2O \rightarrow CO_2 + H_2$	9
$CO_2 + H_2 \rightarrow CO + H_2O$	10

$$r_i = \frac{k_{0,i} e^{\frac{-E_{a,i}}{RT}} p_{O_2}^{n_i} p_{CH_4}^{m_i}}{(1 + K_{CO_2,i} e^{\frac{-\Delta H_{CO_2,i}^{ads}}{RT}} p_{CO_2})} ; \text{to } i = 1, 3 - 6 \quad (1)$$

$$r_2 = \frac{k_{0,2} e^{\frac{-E_a}{RT}} \left(K_{O_2,2} e^{\frac{-\Delta H_{O_2,2}^{ads}}{RT}} p_{O_2} \right)^{n_2} p_{CH_4}^{m_2}}{\left(1 + \left(K_{O_2,2} e^{\frac{-\Delta H_{O_2,2}^{ads}}{RT}} p_{O_2} \right)^{n_2} + K_{CO_2,2} e^{\frac{-\Delta H_{CO_2,2}^{ads}}{RT}} p_{CO_2} \right)^2} \quad (2)$$

$$r_7 = k_{0,7} e^{\frac{-E_{a,7}}{RT}} p_{C_2H_6}^{m_7} \quad (3)$$

$$r_8 = k_{0,8} e^{\frac{-E_{a,8}}{RT}} p_{C_2H_4}^{m_8} p_{H_2O}^{n_8} \quad (4)$$

$$r_9 = k_{0,9} e^{\frac{-E_{a,9}}{RT}} p_{CO}^{m_9} p_{H_2O}^{n_9} \quad (5)$$

$$r_{10} = k_{0,10} e^{\frac{-E_{a,10}}{RT}} p_{CO}^{m_{10}} p_{H_2O}^{n_{10}} \quad (6)$$

According with experimental observations, there is an inhibiting effect of carbon dioxide on the formation of ethylene. This is taken into account by using a Hougen-Watson type rate equation (Eq. 1), when the inhibiting effect of oxygen is not detected. In some cases, oxygen causes an inhibitory effect as well, and this is modeled by including both effects in a Hougen-Watson type rate equation (Eq. 2). The rates of ethane dehydrogenation, ethylene oxidation, and other reactions are modeled via power law type rate equations (Eq. 3-6). The corresponding parameters of this kinetic model are summarized in Table 4. An advantage of this set of equations is that they can be implemented within the existent templates of most commercial process design software (e.g. Aspen Plus, HYSYS, PRO II, etc.).

Table 4. Kinetic parameters of the OCM kinetic model [11].

Reaction number <i>i</i>	$k_{0,i}$	$E_{a,i}$	$K_{CO_2,i}$	$\Delta H_{CO_2,i}^{ads}$	$K_{O_2,i}$	$\Delta H_{O_2,i}^{ads}$	m	n
1	0.2×10^{-5}	48	2.5×10^{-13}	-175			0.24	0.76
2	23.2	182	8.3×10^{-14}	-186	2.3×10^{-12}	-124	1	0.4
3	5.2×10^{-7}	68	3.6×10^{-14}	-187			0.57	0.85
4	1.1×10^{-4}	104	4×10^{-12}	-168			1	0.55
5	0.17	157	4.5×10^{-13}	-166			0.95	0.37
6	0.06	166	1.6×10^{-13}	-211			1	0.96
7	1.2×10^7	266					1	0.96
8	1.2×10^3	300					0.97	0
9	1.9×10^{-4}	173					1	1
10	2.6×10^{-2}	220					1	1

1.2.2 CO₂ removal section

The downstream processing of the effluents of the OCM reactor starts with water removal by condensation followed by carbon dioxide reactive absorption using amines. In this stage, the effluent gases are cooled down and separated from the condensed water. Then they are put in countercurrent contact with an amine solution in a packed or tray column. In this unit, carbon dioxide is absorbed with a monoethanolamine (MEA) solution under high pressure, allowing the upgrading of the OCM effluent gases. This step also requires a stripping column where the MEA is regenerated at high temperatures, releasing the absorbed CO₂. This process can be highly energy intensive depending on the CO₂ content in the original effluents. A flowsheet of the absorption section is represented in Figure 4.

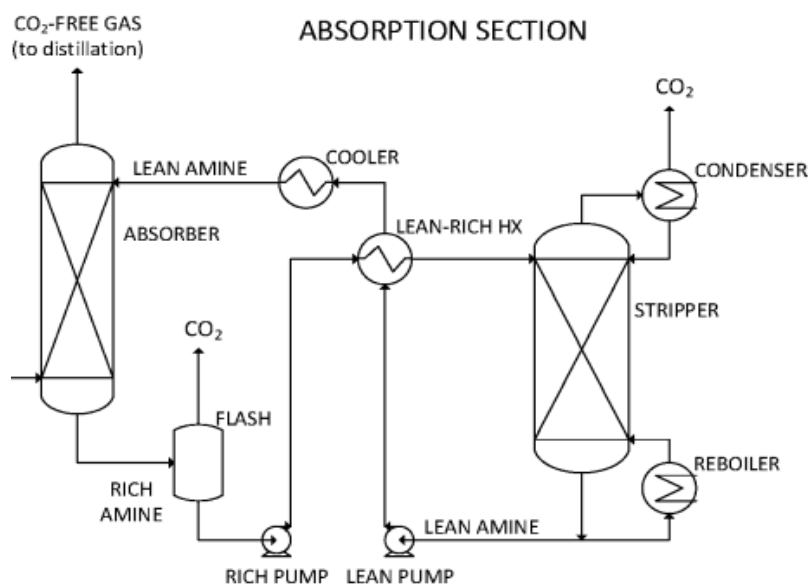


Figure 4. General flow diagram of absorption process for CO₂ removal [12].

1.2.3 Ethylene purification section

The last stage of the downstream purification process involves the separation of unreacted methane and the recovery of ethylene fulfilling market specifications. This section is composed of two distillation columns that operate under high pressure and cryogenic temperatures. The first column is called de-methanizer unit; here methane is separated from the ethane/ethylene mixture. The second column is known as the de-ethanizer unit,

where the olefin and the paraffin are separated. Because of the similar relative volatility of the components, these two columns require large number of stages and large reflux ratios. Taking into account that they operate under high pressure and cryogenic conditions; these columns are highly energy-intensive and consequently costly to operate. In addition, the units are constructed to withstand the high internal pressures and heavy loads, the low temperatures, and large mechanical stresses; all within a cryogenic insulation. These features highly increase the capital costs of the distillation train. Typical specifications of the cryogenic distillation columns used during the separation of methane-ethane-ethylene are summarized in Table 5.

Table 5. Typical column specifications in the separation of OCM gases [3].

Specification	Demethanizer column	Deethanizer column
No. Stages	36	74
Column diameter [m]	5.5	3.4
Structured Packing type	Sulzer MellapackPlus	Sulzer MellapackPlus
Packing Section Height [m]	10	10.65
Top Stage Temperature [°C]	-106.9	-8.5
Top Stage Pressure [bar]	35	33.8
Bottom Stage Temperature [°C]	-5.9	14.8
Condenser Duty [kW]	-7556.93	-10369.49
Reboiler Duty [kW]	3235.22	11420.34

In general, the cryogenic distillation accounts for 95 % or more of the total energy consumption in the OCM downstream process. Large energy is consumed in the gas compressors, the refrigeration systems, and in the reboilers of the columns. This have brought the attention of many researchers to develop less energy-intensive separations.

1.3 Alternative separation in the OCM process

The oxidative coupling of methane (OCM) process has been a research target of academic and industrial players for many years. This because the low-cost and wide availability of natural gas, biogas and shale gas around the globe. If effectively implemented at the industrial scale, the OCM process would contribute to generate added value to methane,

and to reduce oil consumption in the petrochemical industry. In turn, this will contribute to increase crude reserves in the long term [13] and to reduce gas flaring in production fields. With this in mind, several efforts have been done to improve the performance of current cryogenic separations. The most recent attempts involve the use of heat-integrated distillation configurations, and the use of alternative adsorption processes. Specifically, the use of selective solid adsorbents has been identified as a promising alternative to reduce operating costs during the downstream separations in the OCM process. A key factor of the adsorption process is the adsorbent material. For the separation of OCM effluent gases, different materials have been tested, namely activated carbons, zeolites, metal-organic frameworks (MOFs), etc. In particular, zeolites and zeolite-related materials have demonstrated high selectivity in the olefin-paraffin separation.

According to recent reports on OCM gases separations, zeolites exhibit high selectivity in the separation of methane and C₂ olefins. These materials have a strong affinity for ethylene caused by the different interaction of the hydrocarbons with the divalent metals (e.g. Ca²⁺ ions) on the surface. These cations have a strong interaction with the ethylene double bond (π), allowing a selective adsorption over methane. Triebe *et al* [14] evaluated the partitioning factors achieved in the separation of ethylene/methane mixtures using different zeolites (4A, 5A, 13X, CaX and H-mordenite). Particularly, CaX zeolite showed the higher selectivity among the evaluated zeolites (Figure 5).

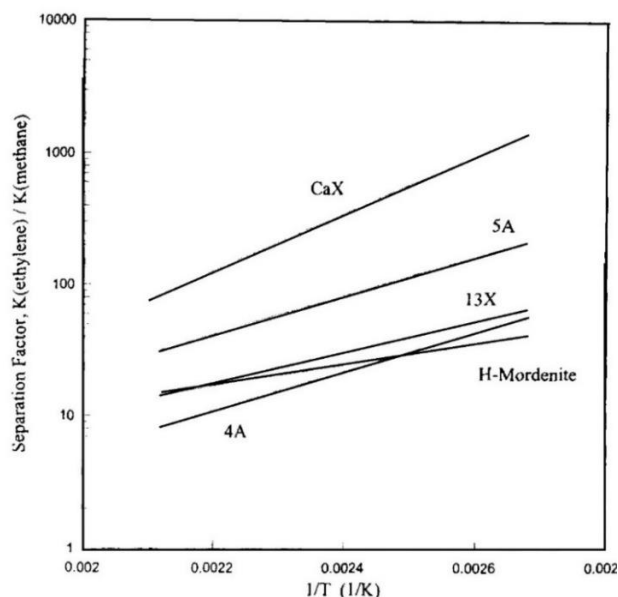


Figure 5. Separation factor for the ethylene/methane mixture in different adsorbents [14].

Similarly, some reports have studied the equilibrium adsorption of the pure components present in effluents of the OCM process. According to results, CaX zeolite exhibits higher adsorption capacity than LTA zeolites [15, 16]. Taking into account the effectiveness of zeolites in the separation of OCM effluents at lab and pilot scale, it is expected that the implementation at the industrial scale would be done by developing suitable temperature or pressure swing adsorption systems. In particular, pressure swing adsorption (PSA) is a preferable due to the lower energy consumption, and the maturity of its development at the industrial scale. This process has been employed in multiple applications, such as air dehydration, hydrogen purification, nitrogen-oxygen separation, ethanol dehydration, etc. [17, 18]. Despite multiple investigations have been done to explore the potential use of zeolites as selective adsorbents in the separation of OCM gases, few have been devoted to the assessment of the PSA performance at the industrial scale.

1.4 Project description

Bases upon the described context, the aim of this work was to develop a pressure swing adsorption (PSA) process for the separation of OCM effluents, using zeolite-based molecular sieves as adsorbents. To carry out this work, it is necessary to collect physicochemical data on the adsorbent material and the OCM gases (e.g. physical and thermochemical properties) in order to construct a mathematical model that describes the adsorption operation. Then, the model must be validated using experimental data to verify the good agreement with the PSA behavior.

Once the mathematical model is established and validated, the operating conditions are determined, and the cycles that control the adsorption and desorption steps are programmed. Then, the process model is implemented in a commercial software (Aspen Adsorption), where the performance of the operation is analyzed. Finally, a preliminary economic evaluation of the separation process is carried out to be compared with the cryogenic distillation process (traditional separation).

2. Chapter Two: Fundamental concepts

2.1 Adsorption

Adsorption occurs due to the selective transference of one or more components (i.e. adsorbates) from a gas or liquid phase onto the surface of a solid material (i.e. adsorbent). The phase change of the adsorbate is caused by interaction and affinity with the surface of the adsorbent. During the process, the adsorbate experiences a reduction in its energy potential, which explains the exothermic nature of adsorption. Generally, adsorption occurs under reversible physical interactions (e.g. van der Waals or dipole forces), in the so called Physisorption. However, in some cases the interaction with the surface is strong, and chemical bonds can be formed. In this case the process is called Chemisorption, and sometimes it can be hardly reversible or even irreversible. The physical adsorption is most commonly applied to allow regeneration and reuse of the adsorbent, and three types of effects can govern this process: steric, kinetic, and equilibrium effects.

2.1.1 Steric effects

The steric hindrance occurs in adsorbent materials that have microporous structure with pore openings of similar size to that of the adsorbate molecules. This is the case of some zeolites, metal organic frameworks, and activated carbons, among others. When steric effects take place, the adsorption is favorable to those components with a smaller kinetic diameter than the micropore opening. A typical application of steric effects and size exclusion occurs in the separation of *n*-paraffins from *i*-paraffins, which have different molecular sizes and shapes. Another example is the dehydration of azeotropic ethanol with LTA zeolites. In this case, the 3Å and 4Å openings permit water to reach the active sites for adsorption, while ethanol is rejected. A scheme describing steric effects is described in Figure 6, where the structure of zeolite works as a molecular sieve to separate branched from linear paraffins.

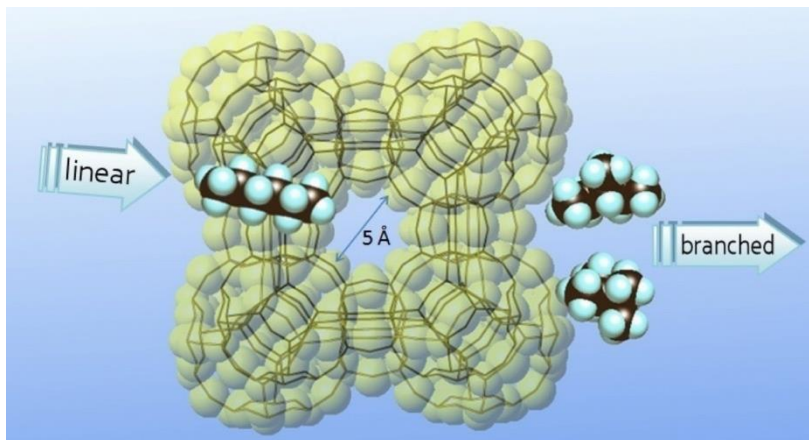


Figure 6. Molecular sieving effect for linear and branched paraffins in 5A zeolite [19]

2.1.2 Adsorption equilibria

In a typical adsorption process, the solute establishes a dynamic equilibrium between the fluid and the solid surface [20]. The solute distribution between the two phases is governed by the chemical nature of the phases, the concentration of the solute in the fluid (i.e. partial pressure in the case of gases), and the temperature. In general, the characterization of the adsorption equilibrium for a given solute-solvent system is done under isothermal conditions. This is described by depicting surface coverage (i.e. surface loading) at different concentrations (i.e. partial pressures in the case of gases) of the solute. The generated plots are called adsorption isotherms, and in general, they are classified in families according with their shapes. Brunauer *et al* [21] described and classified five types of isotherms, which may vary according to the involved phenomena during the adsorption process (Figure 7).

The type I isotherm corresponds to monolayer adsorption, and it is characterized by a limited adsorption capacity of the material. This behavior is mainly observed when adsorption occurs on microporous solids. Type II isotherms exhibits an inflection point when the monolayer is completed. In this case the change of shape is due to adsorbate deposition in multi-layers; this occurs in macroporous materials. Type III isotherms have a convex shape, with unfavorable performance at low pressure due to a weak adsorbate-adsorbent interaction. However, at higher pressures there is a higher adsorption capacity. This occurs by unrestricted multilayer adsorption and is typical of mesoporous and macroporous materials. The type IV and V isotherm are capillary-condensation versions of the type II and III, respectively [20, 22].

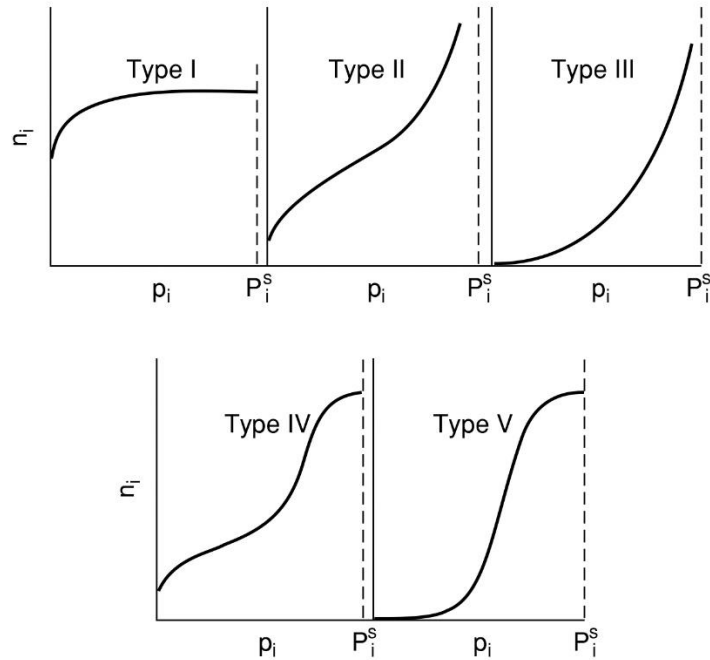


Figure 7. The five types of van der Waals adsorption isotherms [22].

Langmuir isotherm

The Langmuir equation is a theoretical based model suitable to describe type I isotherm behavior. This model is used in systems where chemisorption occurs (i.e. monolayer adsorption). This type of interactions are due to the presence of ionic or covalent bonds between adsorbent and adsorbate. Some of the assumptions involved in the formulation of the Langmuir model [23] are:

- Surface is homogeneous, that is, adsorption energy is constant over all sites.
- Adsorption on surface is localized, that is, molecules are adsorbed at specific and localized sites.
- Each site can accommodate only one molecule.

The Langmuir model assumes that the adsorption-desorption process occurs in equilibrium, and each step it is formulated as a chemical reaction between the adsorbate and the solid surface [23]. Based on the above, the Langmuir isotherm is written in terms of adsorbed load as:

$$q = \frac{bq_m p}{1 + bp} \quad (7)$$

Where b is the equilibrium constant, and it is defined as the ratio between the adsorption (K_a) and desorption (K_d) constants. q_m is the maximum load of the adsorbate on the adsorbent surface, and p is the partial pressure of the component.

Freundlich isotherm

Freundlich proposed an equation that describes physisorption phenomenon on microporous adsorbents, such as in zeolites. This model has limitations at high pressures and low temperatures since its exponential behavior does not give a limiting value (typical of type II isotherms). The Freundlich model is considered as an empirical equation in the form [23]:

$$q = bp^{\frac{1}{n}} \quad (8)$$

Where b and n are constants that depend on the temperature ($n > 1$).

Langmuir-Freundlich (L-F) Isotherm

This equation is a combination of the Langmuir and Freundlich isotherms to give the following relation:

$$q = \frac{q_m bp^{\frac{1}{n}}}{1 + bp^{\frac{1}{n}}} \quad (9)$$

The L-F isotherm was proposed to provide a better adjustment at high pressures in type II systems. This model is usually applied in commercial software because it has shown satisfactory results in the prediction of the adsorption equilibrium in a variety of mixtures.

2.1.3 Adsorption kinetics

Generally, physical adsorption occurs rapidly once the adsorbate reaches the adsorbent surface because of the strong interatomic forces at the active sites. Instead, within porous materials the process is generally limited by mass transfer. As shown in Figure 5, there are

three mass transfer resistances along the adsorption process: at the external fluid film, within the intercrystalline macropores, and in the microporous crystals.

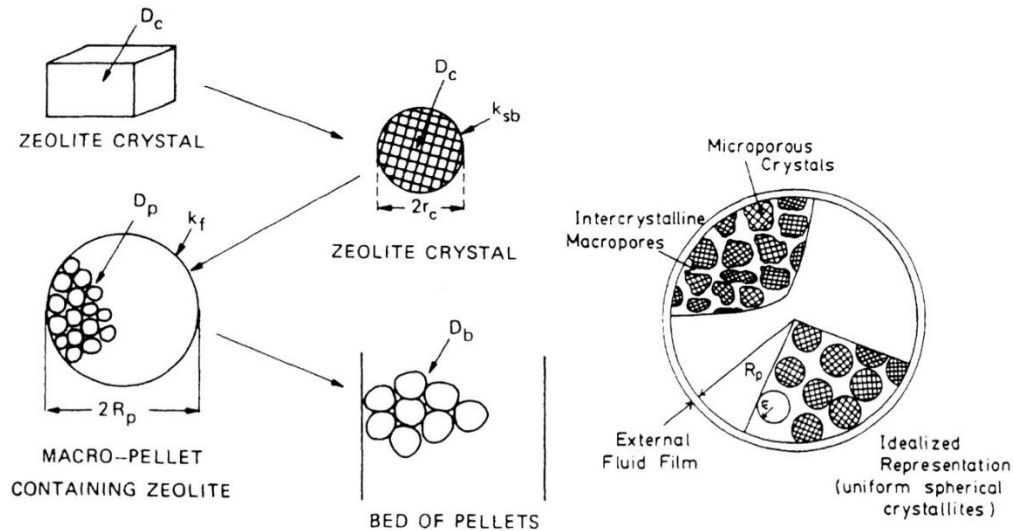


Figure 8. Schematic representation of the three transfer mass resistance [24].

The corresponding mass transfer mechanisms along these different media can be described as follows:

- 1) The solute is transported from the fluid phase through the boundary layer around the adsorbent material (external fluid film diffusion).
- 2) The solute travels through the fluid contained within the intercrystalline micropores (diffusion through the macropore).
- 3) The solute reaches the crystal and get into the micropores (microporous diffusion)
- 4) The solute is adsorbed on the inner surface of the material (adsorption step).

The desorption process occurs in a similar manner. The macropore and micropore mass transport can be described using simplified or complex models. Fick's diffusion models can be employed for this purpose. Also, statistical mechanics methods, using molecular dynamics or Monte-Carlo simulations approaches can be applied [25]. Nevertheless, at the industrial practice, these approaches could represent high computational costs and unpractically long designing times. Therefore, more practical and simplified approaches have been used to model the adsorption process during the design of industrial units. Among these, the Linear Driving Force (LDF) model is typically incorporated in process

design software. This is a flexible, easy-to-solve, empirically-based model similar to a convective mass transfer model. The LDF model relies on an adjustable parameter that is regressed based upon adsorption experiments performed at different operating conditions. Thus, in the LDF model, the three mass transfer resistances observed during the adsorption process are lumped within an effective mass transfer resistance [26, 27]. This model related the mass transfer rate due to adsorption, as follows:

$$J = \rho_s \frac{\partial q}{\partial t} \quad (10)$$

Where, the flux ($\frac{\partial q}{\partial t}$) is represented for the following expression:

$$\frac{\partial q}{\partial t} = MTC (q^* - q) \quad (11)$$

The mass transfer coefficient (MTC) can be calculated as a sum of three resistances, as follows [28]:

$$\frac{1}{MTC} = \frac{r_p}{3k_f} + \frac{r_p^2}{15 \varepsilon D_{eff}} + \frac{r_c^2}{15 \bar{K}_K D_c} \quad (12)$$

The first term corresponds to film resistance, which involves convective dispersion of the solute within the bulk fluid, and the diffusion through the stagnant fluid surrounding a particle. This resistance appears when the adsorption of one component occurs in a binary mixture. The second term consists in the diffusion of gas molecules that occurs in the macropore due to the collisions with other molecules and with the pore walls. Diffusion by collision among molecules in large pores is called molecular diffusion. However, when the diameter of the pore becomes smaller, collisions between the molecules and the pore walls are more frequent giving rise to another diffusion mechanism, called Knudsen diffusion. The third term is related with the micropore resistance given by surface diffusion of molecules across the interior surface of the adsorbent material. This occurs because adsorbate species can move by surface attractive forces, allowing molecular mobility within the micropore.

2.2 Adsorbent materials

Porosity in adsorbent materials is a critical variable in the design of adsorption processes because it has a great impact both in equilibria and kinetic phenomena. For instance, if the

solid adsorbent has a high adsorption capacity but slow kinetics, a high adsorption efficiency would require long residence times within the column, hence, a low throughput. On the other hand, if the solid exhibits low adsorption capacity but rapid diffusion, the separation is not efficient and large equipment would be required. For this reason, commercial adsorbent materials must have a high surface area and a large pore network to improve the relationship between adsorption equilibria and kinetic effects.

Most commercial adsorbents are classified as homogeneous and composites. The homogeneous materials consist of chemical compounds of defined nature, such as alumina, silica gel, and activated carbon. In comparison, the composites materials are made by blending active agents and binders, such as in the case of zeolite-based molecular sieves.

2.2.1 Alumina

Active alumina is a porous material with high surface area, composed of aluminum oxide. It is widely used at the industrial scale for dehydration of liquids and gases. There are a variety of alumina-based materials, but the most commonly used in drying is γ -alumina. Some characteristics of a γ -alumina are given in Table 6. As observed, this material has a good macropore and micropore volumes, and a large macropore radius to allow a rapid transport of molecules.

Table 6. Typical characteristics of γ -alumina [23]

Characteristic	value
True density	2.9 – 3.3 g/cc
Particle density	0.65 – 1.0 g/cc
Total porosity	0.7 – 0.77
Macropore porosity	0.15 – 0.35
Micropore porosity	0.4 – 0.5
Macropore volume	0.4 – 0.55 cc/g
Micropore volume	0.5 – 0.6 cc/g
Specific surface area	200 – 300 m ² /g
Mean macropore radius	100 – 300 nm
Mean micropore radius	– 3 nm

2.2.2 Silica gel

Silica gel is made by coagulation processes from solutions of silicic acid in colloidal state. This adsorbent is used at the industrial scale for water uptake because it has strong hydrophilicity due to the presence of hydroxyl groups on the surface. Silica gel has been also used in the drying of non-reactive and reactive gases, adsorption of hydrogen sulfide, oil vapors, and polar components, such as alcohols [23]. This material presents some variabilities depending on the mode of synthesis, however most typical characteristics are summarized in **Table 7**.

Table 7. Typical characteristics of Silica gel [23]

Characteristic	value
Particle density	0.7 – 1.0 g/cc
Total porosity	0.5 – 0.65
Pore volume	0.45 – 1.0 cc/g
Specific surface area	250 – 900 m ² /g
Range of pore radius	1 to 12 nm

Silica gel has a larger surface area than alumina, but it has a smaller pore size. It is advantageous in the separation by steric effects.

2.2.3 Activated carbon

Activated carbons are made by thermal decomposition and further activation of biogenic or carbonaceous materials, such as, wood, shell nuts (e.g. macadamia nuts, coconuts) and coal. Commercially, there are two main grades of activated carbons, materials with large pores used for liquids separations, and those with small pores for gas adsorption. This adsorbent is commonly used for the separation of mixtures containing non-polar components, and the adsorption capacity largely depends on the thermal treatment and the activation procedure. The typical characteristics are summarized in Table 8.

Table 8. Typical characteristics of Activated Carbon [23]

Characteristic	value
True density	2.2 g/cc
Particle density	0.73 g/cc
Total porosity	0.71
Macropore porosity	0.31
Micropore porosity	0.40
Macropore volume	0.47 cc/g
Micropore volume	0.44 cc/g
Specific surface area	1200 m ² /g
Mean macropore radius	800 nm
Mean micropore radius	1 – 2 nm

2.2.4 Zeolites

Zeolites are crystalline aluminosilicates composed by tetrahedral units of SiO₄ and AlO₄, interconnected through an oxygen atom. Due to its crystalline structure, this material generates pores that may differ in size depending on their configuration (see Figure 9). Based upon the different achievable pore sizes of the crystals, selective molecular separation can be accomplished by size exclusion, behaving as a molecular sieve. The pore size and the pore volume can vary depending on the crystalline structure, typically from 0.2 to 0.8 nm and from 0.10 to 0.35 cm³ / g, respectively.

Zeolites are widely used in adsorption applications, catalysis, and ion exchange, mainly because their competitive costs compared with similar materials. The zeolitic adsorbents have been mainly used on three different areas [29]:

- 1) Removal of traces or diluted impurities of a gas.
- 2) Separation of gas mixtures.
- 3) Gas analysis.

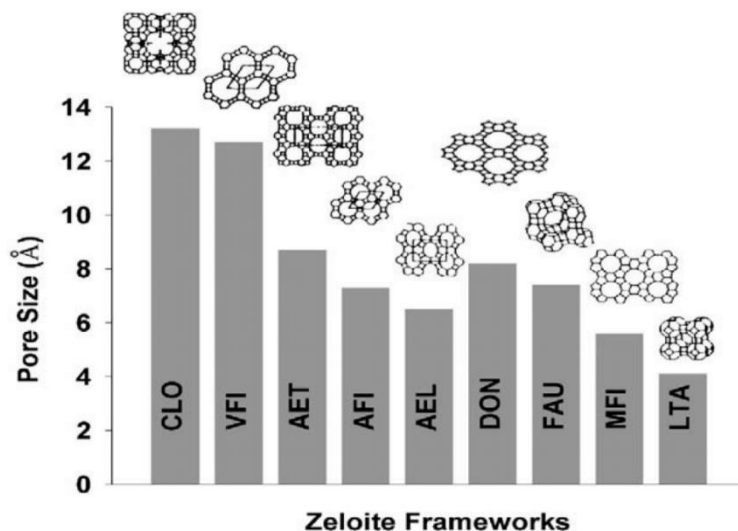


Figure 9. Comparison of pore size in different types of zeolites [29].

In gas purification, the typical applications are related with the removal of impurities like toxic, organic and corrosive compounds. Applications in the bulk separation are focused in the production of industrial gases like nitrogen, oxygen and ethylene. Gas analysis applications are mainly in gas chromatography, and in dehumidification of analytical gases. From the large variety of natural and synthetic zeolites, Lynde Type A (LTA) have been widely used as molecular sieves for paraffin/olefin separations. In particular, their surface activity and their low pore size (3Å, 4 Å and 5Å) made them suitable for the separation of different types of gases. Linde type X zeolite (FAU) has also developed interesting industrial applications, as the purification and separation of gases, due to its ability to exchange metals in its large framework, increasing the selectivity of some components.

2.2.4.1. Zeolite LTA

The zeolite A or LTA is synthesized through the hydrothermal reaction of the silica and alumina gels, in basic medium and water in excess at 70 to 100 °C and at atmospheric pressure. Its formation mechanisms consist of 3 stages: maturation (when depolymerization and reordering of the materials in the gel occurs), nucleation (when crystalline precursors are formed) and crystal growth [30]. The crystal structure of zeolite

LTA contains eight cages per unit cell (Figure 10). This unit cell is the consequence of the ordering of the Si and Al atoms in the framework during its crystal growth [31].

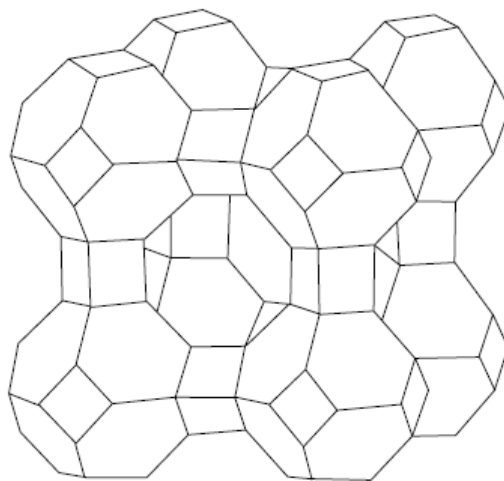


Figure 10. Framework structure of the zeolite LTA [32].

2.2.4.2. Zeolite X

Zeolite X belongs to the aluminosilicate family with a FAU framework type. It is represented as $[M_x(H_2O)_y] [Al_xSi_{192-x}O_{384}] - FAU$, where x is the number of Al atoms per unit cell (between 77 and 96) and M is the exchangeable cation. The X zeolite is synthesized by the hydrothermal reaction of aluminosilicate gels at 70 to 300 °C (usually 100°C) and at atmospheric pressure, under alkaline conditions [33].

The framework of zeolite X consists of sodalite cages connected in a cubic manner over six-membered double rings (instead of double four-rings as for LTA), as is shown in Figure 9. This creates a large cavity in the zeolite accessible by a three-dimensional 12-ring pore system [34], which it is favorable for its ion exchange.

Molecular sieves based on zeolite 5A and zeolite CaX are studied as adsorbent materials for the OCM process according to reported by Garcia and the proposed in this study, respectively. Their main characteristics are discussed in the following sections.

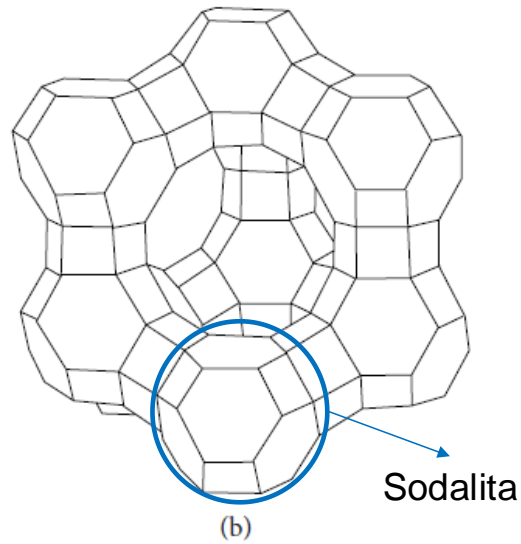


Figure 11. Framework structure of the zeolite FAU [32].

Zeolite 5A

The 5A zeolite is synthesized as a sodium LTA zeolite (4A) and produced through ionic exchange between sodium (Na^+) and calcium cations (Ca^{+2}). In addition to the change in affinity for the adsorbates, the ionic exchange can increase the effective pore opening from 4 to 5 angstroms, improving the adsorption performance due to the reduction in diffusivity limitations. The change of micropore diffusivity parameters (D_c in Equation 12) for N_2 , CH_4 and C_2H_6 on 4A and 5A zeolites are summarized in Table 9.

$$D_c = \left(D_\infty \exp\left(-\frac{E_A}{RT}\right) \right) \frac{d \ln P}{d \ln q^T} \quad (12)$$

Table 9. Effect of cation exchange on diffusivity in Zeolite 5A for different gases [30]

	Critical Diameter [Å]	D [cm ² /sec]	Activation Energy [kcal/mole]
Zeolite 4A (Na)			
N ₂	3.7	9.6 × 10 ⁻⁷	6.1
CH ₄	4.08	5.8 × 10 ⁻⁸	7.4
C ₂ H ₆	4.36	5.7 × 10 ⁻⁸	6.2
Zeolite 5A (Ca)			

	Critical Diameter [Å]	D [cm ² /sec]	Activation Energy [kcal/mole]
N ₂	3.7	5.2 x 10 ⁻⁹	1.5
CH ₄	4.08	7.2 x 10 ⁻⁸	3.0
C ₂ H ₆	4.36	5.7 x 10 ⁻⁸	1.3

As observed, structure with a smaller pore diameter have a greater diffusion temperature dependence (i.e. higher activation energy). Instead larger pore sizes allow faster diffusion at any temperature condition. Reported data in Table 9 indicate that molecular diffusion is two orders of magnitude higher in 5A compared with 4A zeolite. Zeolite 5A is widely used in industrial applications as separation of linear and branched hydrocarbons, gas drying, and bulk separation. Particularly, in the treatment of OCM effluent gases, zeolite 5A exhibits a higher selectivity for ethylene compared with methane [15].

Zeolite CaX

This zeolite is synthesized from X zeolite and obtained by ion exchange of the sodium cation (Na⁺) of 13X zeolite with calcium cations (Ca²⁺). This ion exchange increases the positive charge of the surface and increase the effective pore size opening [35]. A characteristic of the CaX zeolite is its adsorption capacity owing to the pore size and shape, Si/Al ratio (1 to 1.5), and their active cation (see Figure 12). The framework of the CaX zeolite described in the Figure 12 contains 8 sodalites and 8 supercages, where sites 1, 1', 2', 2 and 3 can incorporate 16, 32, 32, 32 and 93 calcium cations, respectively. This is favorable because promotes the interaction between cations and adsorbed gases, like Ca²⁺ cation and ethylene double bond (π).

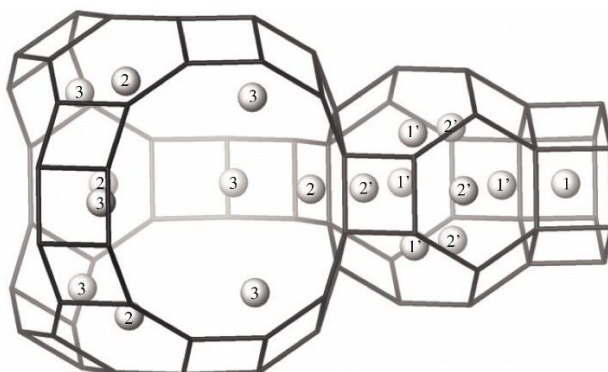


Figure 12. Cation sites in FAU zeolite [34].

The CaX zeolite has a wide range of industrial applications for gas separation owing to its higher thermal and chemical stability. Moreover, the selectivity in olefins (C_2H_4 and C_2H_6) with respect to methane is considerably higher as shown in Figure 13.

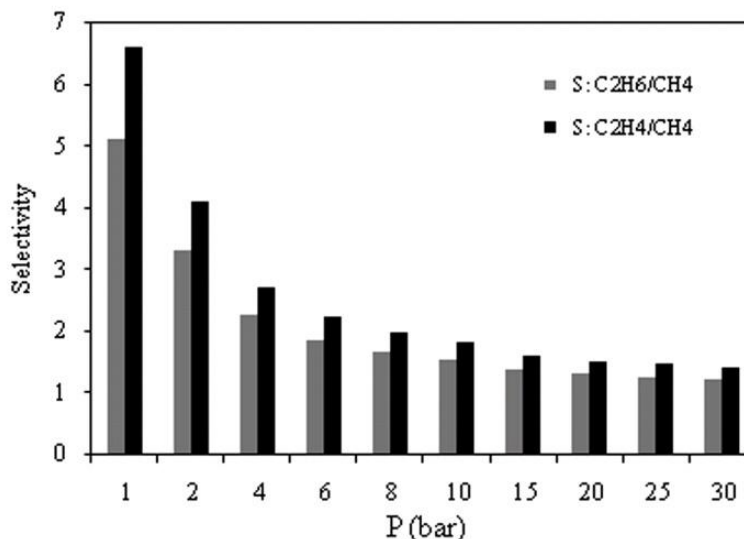


Figure 13. Adsorption selectivity for C_2 olefins compared with methane over zeolite CaX at 298 K and different pressures [35].

2.3 Adsorption processes

Industrial adsorption processes work under cycling operation in two main steps, adsorption and regeneration. During the adsorption step, one or more components from the fluid phase are preferentially adsorbed on the solid material. Then, during the regeneration step the adsorbed components are removed from the saturated material by changes in temperature and/or pressure for use in the next cycle [36]. The adsorption processes are generally carried out on fixed bed columns filled with adsorbent pellets, and an advanced control system is used to manipulate the operating variables. Main operating variables include cycle time, feed flow, pressure, temperature, and flushing times, among others. The cycling times between the adsorption and desorption steps, and the corresponding operating conditions are defined based upon the characterization of the adsorption process. This is done by the analysis of the so-called breakthrough curves, which are the normalized time concentration profiles of the effluent gas, as obtained from dynamic adsorption experiments.

2.3.1 Breakthrough curves

The industrial operations of packed adsorption columns can be characterized by monitoring the change of concentration of the effluent mixture. As example, this process can be described for a gas adsorption. At the beginning of the adsorption operation, the gas is feed to a regenerated solid. As soon as the gas is in contact with the adsorbent material, a particular adsorbate is selectively retained on the surface of the adsorbent and removed from the gas stream. This indicates that the concentration of the adsorbate is nearly zero in the gas stream leaving the packed column. Then, as more untreated gas is fed to the column, the adsorbent starts to get saturated with adsorbate. As a result, a moving front of the saturated solid appears along the packing bed. While this front can be conceptually assumed as a plug type front, in reality it might exhibit an uneven profile due to channeling, bypass, or wall effects within the packing. While the moving front is still far from the end of the column, the concentration of the selectively adsorbed component in the effluent gas stream is very low. However, as soon as the saturation moving front reaches the end of the column, the concentration of the adsorbate in the gas phase starts increasing. The process is completed when the entire packed bed is saturated, and the concentrations of the inlet and outlet gases are identical.

The whole process can be described by tracking the concentration of adsorbate in the gas phase with respect to the inlet concentration (c/c_0) along the adsorption cycle. This is graphically described in Figure 14, and it is typically known as breakthrough curve.

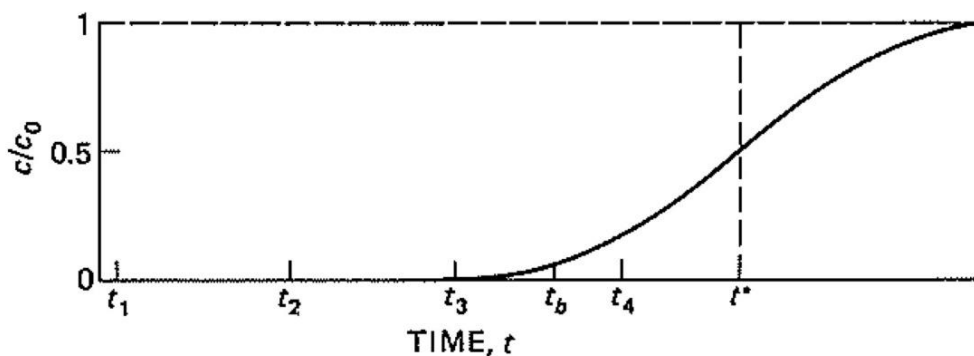


Figure 14. Typical adsorbate concentration profile along a packing bed during adsorption process [37]

The breakthrough time (t_b) in Figure 14 indicates when the feed flow must be stopped to avoid affecting the product purity ($c/c_o < 0.05$). However, if the feed flow pass beyond the breakthrough, the concentration increases rapidly until achieving the same concentration of the feed stream. The breakthrough curve provides information about the amount of adsorbate retained in the bed. The area above the curve in the S-Shaped profile of Figure 14 represents the total solute adsorbed, assuming that the bed is completely saturated ($c/c_o = 1$). Notwithstanding, in a symmetrical curve, the adsorbed amount also can be calculated through the rectangular area in the left side at the time t^* localized in $c/c_o = 0.5$.

The time t^* can be estimated from the material balance with respect to the cross-sectional area of the bed assuming a constant velocity:

$$F_A = u_0 c_0 \quad (13)$$

Where F_A is the feed flow, u_0 is the superficial velocity and c_0 is the solute concentration. Based on an Ideal breakthrough curve, the solute concentration in the time t^* is completely adsorbed, so

$$u_0 c_0 t^* = L \rho_B (q^* - q_0) \quad (14)$$

Where, the equilibrium loading q_0 is equal to zero in the initial time, L and ρ_B is the length and the density of the bed, respectively [38]. Equation 14 allows obtaining t^* for a given velocity, adsorbate concentration, and adsorption capacity.

Another way to describe the adsorption process is monitoring the concentration of adsorbate on the solid adsorbent. This type of profiles along the adsorption process are presented in Figure 15 [37]. Here, the mass transfer zone (MTZ), represented by a black line, is the section of packing where adsorption is still occurring because the solid is not saturated. As observed, the MTZ differs from the plug front (blue line) due to dispersion effects caused by diffusion, channeling, bypass and wall effects. This also explains the difference between t_b and t^* . The time t_3 in Figure 15 corresponds to the breakthrough time t_b of Figure 14.

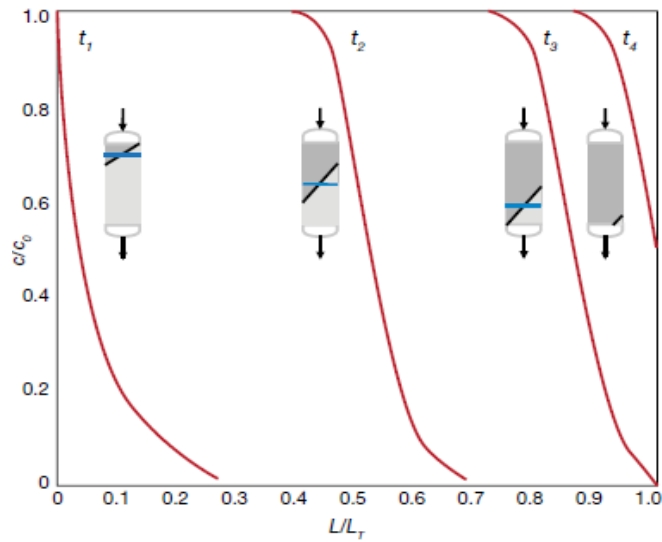


Figure 15. The mass transfer zone moving along the bed [37]

A special characteristic of the breakthrough curve is the typical S-shape. In general, curves with a narrow MTZ (Figure 16(a)) are characteristic of materials with high adsorption capacity compared with others with a wide MTZ (Figure 16(b)).

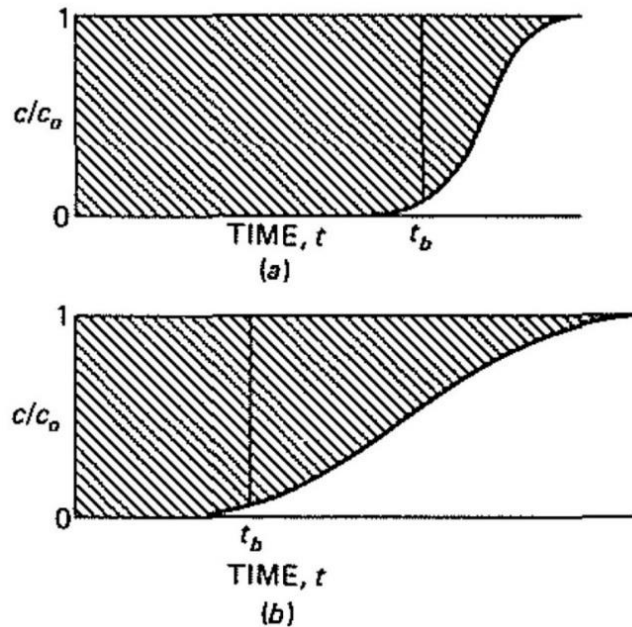


Figure 16. Breakthrough curve for (a) narrow and (b) wide MTZ [38]

For this reason, effective adsorbents have a steep breakthrough curve and almost a flat MTZ moving along the column. Thus, when using effective adsorbents, the breakthrough profiles must be similar regardless the size of the packing bed. This means that the MTZ represents a minor fraction of the total length of the bed. The portion occupied by the MTZ within the packing bed is called the length of the unused bed (LUB) at breakthrough. The LUB is related to the breakthrough time and the residence time as presented in Equation 15.

$$t_b = t^* \left(1 - \frac{LUB}{L}\right) \quad (15)$$

The LUB is a key design parameter to specify the length of the packed bed during the design of adsorption columns.

The regeneration is the second step during adsorption process. In this step, adsorbate is removed from the surface of the adsorbent material by changing the operating conditions. This step is analogous to the previous one, but in this case the MTZ moves backwards until reaching the inlet port of the column. Regeneration can be accomplished by increasing temperature, or by reducing the pressure of the system. If the system uses changes of temperature it is called temperature swing adsorption (TSA). If the desorption occurs by changes of pressure, the process is referred as pressure swing adsorption (PSA). In general, PSA is preferred because is less energy intensive.

2.3.2 Pressure swing Adsorption

The pressure swing adsorption (PSA) is a dynamic process that involves the selective adsorption and desorption of components from a gas mixture, through pressure changes at different time steps. The selectivity depends on the difference in the adsorption equilibrium and adsorption rate at the different pressure levels. Selective separation is achieved if these differences are large among the components in the gas mixture.

In general, the process operates nearly under isothermal conditions, although some temperature changes occur because of the exothermic nature of the adsorption process.

Nonetheless, the temperature is not the most influential variable because the process is mainly governed by pressure changes, high pressure during adsorption, and low pressure during the regeneration step. These cyclic changes generate a difference in the adsorption capacity of the adsorbent as shown in Figure 17.

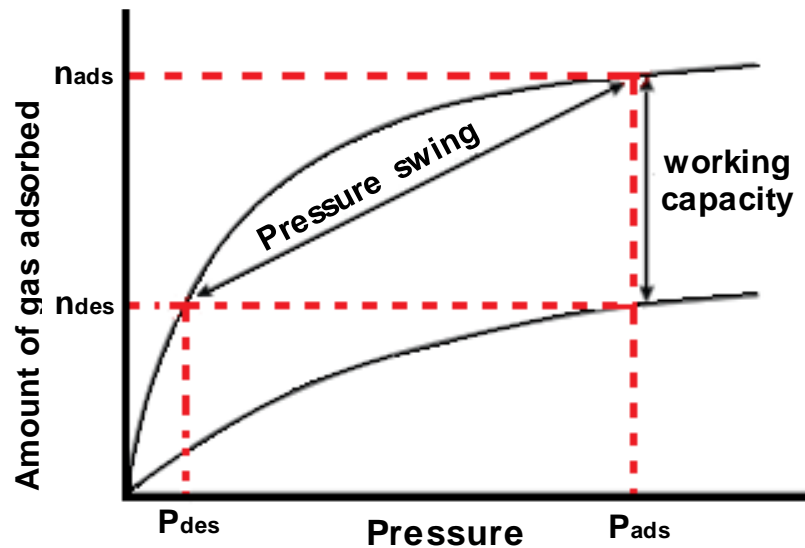


Figure 17. Adsorbent's working capacity in the PSA process. Adapted from [39].

The main industrial applications of the PSA process is the air products separation, hydrogen purification, and natural gas drying. However, in the last years it has been applied in multiple gas processes such as, ethanol dehydration, olefins/paraffin separations, and other hydrocarbon separations.

The PSA process is carried out in parallel fixed-bed columns, operating under simultaneous and cyclic-switching adsorption-desorption steps. The cycle times and flow switches are managed by mean of suitable control loops using automatic valves. Dynamic programming of the operation is determined from the breakthrough curves (breakthrough point) and the corresponding adsorption isotherms at the operating pressure. The most common steps encountered in a PSA operation are the pressurization, high pressure feed, blowdown, regeneration at low pressure, pressure equalization, and rinse. The elementary steps of a PSA, the operating mode and the main characteristics of each step are summarized in Table 10. A typical PSA scheme, based on the Skarstrom cycle [40], is presented in Figure

18. The Skarstrom cycle is used during gas drying and gas purification, this is, when the valuable product is the raffinate gas. Nevertheless, in some applications the adsorbate is the valuable product. In this case the purity of the valuable product decreases during the depressurization and purge steps, where the adsorbate is released with a significant fraction of raffinate gas.

Table 10. Elementary Steps [36]

Elementary step	Mode of operation	Principal features
Pressurization	<ol style="list-style-type: none"> 1. Pressurization with feed from the feed end 2. Pressurization with raffinate product from the product end prior to feed pressurization 	<p>Enrichment of the less selectively adsorbed species in the gas phase at the product end.</p> <p>Sharpens the concentration front, which improves the purity and recovery of raffinate product</p>
High-pressure adsorption	<ol style="list-style-type: none"> 1. Product (raffinate) withdrawal at constant column pressure 2. The column pressure is allowed to decrease while the raffinate product is drawn from the product end 	<p>Raffinate product is delivered at high pressure</p> <p>Very high recovery of the less selectivity adsorbed species may be achieved, but the product is delivered at low pressure</p>
Blowdown	<ol style="list-style-type: none"> 1. Countercurrent blowdown to a low pressure 2. Co-current blowdown to an intermediate pressure prior to countercurrent blowdown 	<p>Used when only raffinate product is required at high purity; prevents contamination of the product end with more strongly adsorbed species</p> <p>Used when extract product is also required in high purity; improves extract product purity and may also increase raffinate recovery</p>
Desorption at low pressure	<ol style="list-style-type: none"> 1. Countercurrent desorption with product purge 2. Countercurrent desorption without external purge 	<p>Improves raffinate product at the expense of decrease in recovery; purge at sub-atmospheric pressure reduces raffinate product loss but increases energy cost.</p> <p>Recovery enhancement while maintaining high product purity is possible only in certain kinetic separation</p>

Elementary step	Mode of operation	Principal features
	3. Evacuation	High purity of both extract and raffinate products; advantageous over product purge when the adsorbed phase is very strongly held
Pressure equalization	The high and low-pressure beds are either connected through their product ends of the high-pressure bed are connected to the respective ends of the low-pressure bed.	Conserves energy and separative work
Rinse	The bed is purged with the preferentially adsorbed species after high-pressure adsorption at feed pressure in the direction of the feed	Improves extract product purity when the lighter species are co-adsorbed in large amount with heavier components

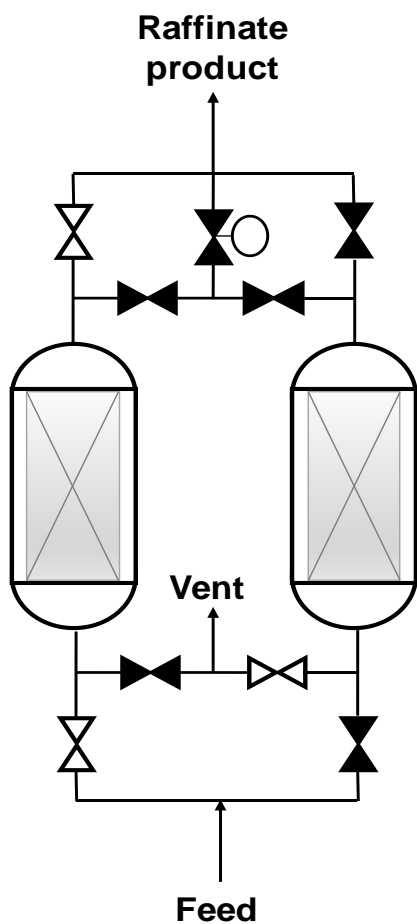
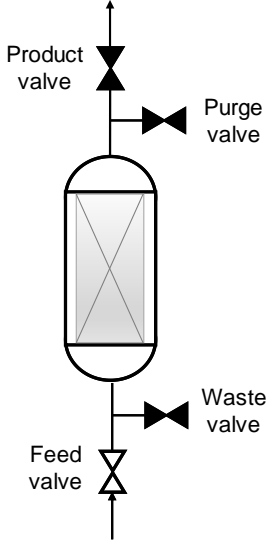
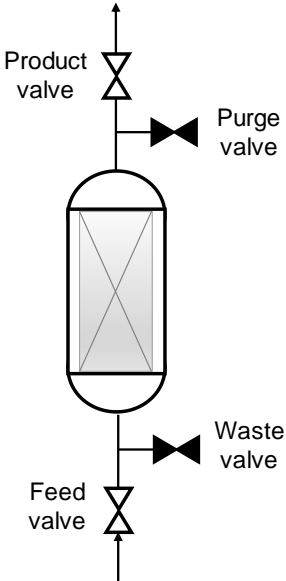
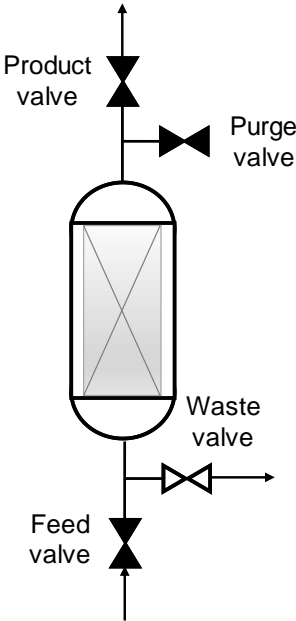
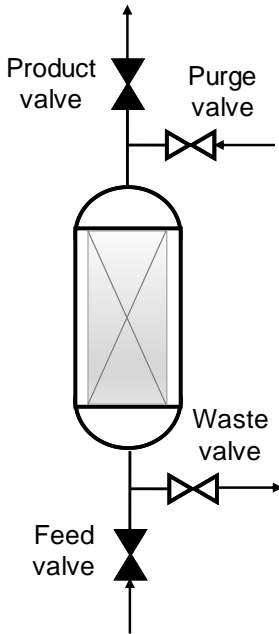


Figure 18. Pressure swing adsorption scheme.

The Skarstrom cycle operation consist in four steps (pressurization, adsorption, blowdown and countercurrent purge), as it is described in Table 11.

Table 11. Description of Skarstrom cycle

Skarstrom step	Operation step
<p>Pressurization: In this step, the bed is pressurized to the higher operating pressure with the feed. There, the feed valve is ON while the other valves from the bed are OFF.</p> <p>Note: The valve ON correspond to color white and the valve OFF to color black.</p>	
<p>Adsorption: In this step, the stream feed is fed at high pressure, where the strongly adsorbed component is retained while the raffinate goes through the bed.</p>	

Skarstrom step	Operation step
<p>Blowdown: When the bed saturation is achieved, the feed, product and purge valves are OFF, and the waste valve is ON in order to depressurize the bed until reach atmospheric pressure.</p>	
<p>Countercurrent purge: Once the atmospheric pressure is achieved in the bed, the Purge valve is ON to feed a fraction of the raffinate product at low operating pressure.</p>	

This cycle is used for small-scale of air drying and other processes where the impurities are present at low concentration and the selectivity of the adsorbent material is high [36].

3. Chapter three: Modeling of pressure swing adsorption process

This study explores the adsorption of effluent gases from an oxidative coupling of methane (OCM) process on a CaX zeolite, in order to design and implement an industrial scale PSA system. The effluents gases involved in this study are methane, ethane and ethylene only. The other components (i.e. water, carbon monoxide, carbon dioxide, and hydrogen) are not considered as it was assumed that were removed in a previous section or that the amount adsorbed on the zeolite is negligible. Water is removed by condensation after the reaction section, carbon dioxide is absorbed using counter current contact with Methyl ethylamine at 10 bar [12]. Carbon monoxide and hydrogen are inert on zeolite CaX and are present in low amounts in typical reactor effluents [41], [42]. In the downstream section, one of the main challenges is to reach the ethylene purity (99.9%) for polymer applications. However, the separation technologies available requires high energy consumption to achieve these purities constrains. Cryogenic distillation is the traditional separation operation to separate methane from olefins, reaching a 98,7 % recovery of ethylene at 99.9 % of purity. Nevertheless, the energy consumption represents at less 49% of the total energy cost [43].

In order to evaluate the feasibility of a PSA system as alternative to the distillation separation, a computer-based assessment of the technology was accomplished. A mathematical model was implemented using the Aspen Adsorption software, incorporating a linear driving force (LDF) adsorption rate model. The corresponding transport parameters were fitted from experimental data in order to validate the model proposed.

3.1 Mathematical model

The design of the adsorption processes requires the implementation and use of rigorous models to describe the behavior during the gas separation. In general, the detailed modeling of mass transport processes is required taking into account that diffusion within the porous structure of the adsorbent is the controlling step. Then, there is need for estimating and quantifying the mobility of the molecules within the solid matrix, and to establish their interaction with the adsorbent surface. Models with different degrees of complexities have been proposed to describe the dynamics of gas adsorption on solid surfaces. In these models is necessary to consider some approximations that involve the assumption of a pseudo homogeneous bed (see Figure 19), where material balances are formulated with respect to the average values of the system variables. Although these average values do not represent the values of each particle, they can describe the macroscopic behavior of the adsorption process in the PSA unit.

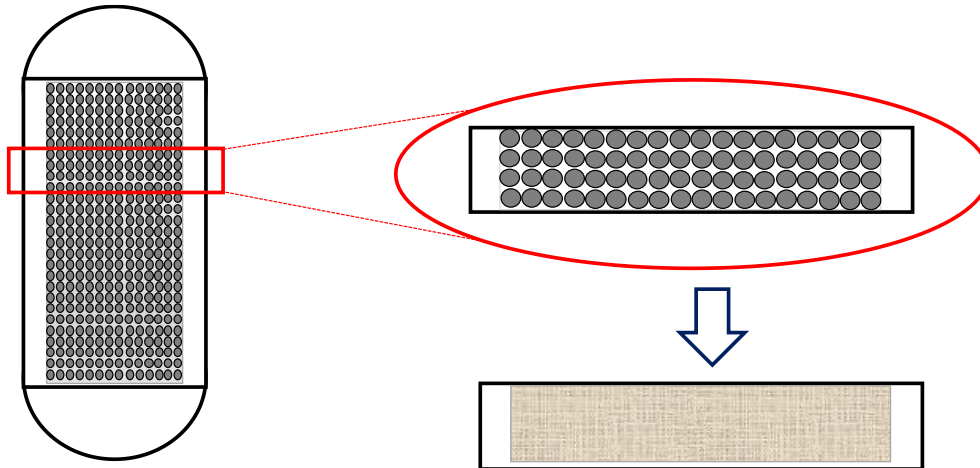


Figure 19. Pseudo-homogeneous control volume [44].

In the Figure 19, the bed is considered with vertical orientation, axial flow and the void fraction is uniform in all fixed-bed. In addition to this, other typical assumptions are involved in the modeling as it is presented below.

- Ideal gas law is obeyed.
- Momentum balance is simplified by using the Ergun equation.

- Macropore and micropore diffusion are simplified by Linear Driving Force (LDF).
- Film mass transfer in the layer around the pellets is considered.

With these assumptions, the whole set of mass balances for each component, the equilibrium models, and the corresponding energy balances for the gas and solid phases are formulated. Details, fundamentals, assumptions, and parameters of the equations used in the modeling of the adsorption process are described in the following sections.

3.1.1 Adsorption equilibrium model

Adsorption equilibrium of pure components can be described using the Langmuir model. This has exhibited good agreement with experimental adsorption isotherms of OCM effluent gases over CaX zeolites. The Langmuir model is expressed as in Equation 16.

$$q_i = \frac{b_i q_{m_i} p_i}{1 + b_i p_i} \quad (16)$$

However, it is necessary adjust the nomenclature from the literature equations to the default formats used in the Aspen Adsorption software. This will help unifying concepts that will be addressed later, and to guide future users on the basics of the software. In this regard, the equation 17 is expressed as follow

$$q_i = \frac{IP_1 P_i}{1 + IP_2 P_i} \quad (17)$$

Here, the parameters $IP_1 = b_i q_{m_i}$ and $IP_2 = b_i$, where, q_m represent the maximum surface loading (kmol/kg), b is the ratio between the adsorption and desorption kinetic constants (bar^{-1}), and P_i is the partial pressure of each component in the gas mixture.

The list of adsorption equilibrium parameters for the OCM gases on CaX zeolites were fitted with the experimental data of isotherms previously reported in the literature [35], using the equation 2. These parameters are summarized in Table 12 and presented together with the adsorption enthalpy of each gas reported by Mehdipour and Fatemi [45].

Table 12. Adsorption equilibrium and kinetic parameters of OCM gases on CaX zeolite

Component	$IP_1 \times 10^3$ [kmol/kg]	IP_2 [1/bar]	ΔH_{ads} [kJ/kmol]*
C ₂ H ₆	1.23	0.6138	-25956
C ₂ H ₄	1.48	0.6427	-29783
CH ₄	0.24	0.1142	-20214

*Data taken from Mehdipour and Fatemi [45]

Due to the temperature dependence of the equilibrium constant ($IP_2 = k_a/k_d$), according to the Van't Hoff equation [46]:

$$IP_2 = b = b_0 \exp\left(\frac{-\Delta H_{ads}}{RT}\right) \quad (18)$$

The obtained IP_2 values exhibit a decreasing trend: C₂H₄ > C₂H₆ > CH₄. This is related to the heat of adsorption (i.e. isoesteric heat), because this increases with the greater molecular interaction with the adsorbent surface (see Figure 20). The graphic behavior of Equation 2 for the three gases under study are presented in Figure 20, together with reported adsorption isotherm experiments [45]. A main assumption of the model is that there is no competitive adsorption, so the pure component Langmuir model can be used during the multi-component adsorption equilibrium calculations. In this case, surface selectivity will be dictated by the relative values of the Langmuir parameters.

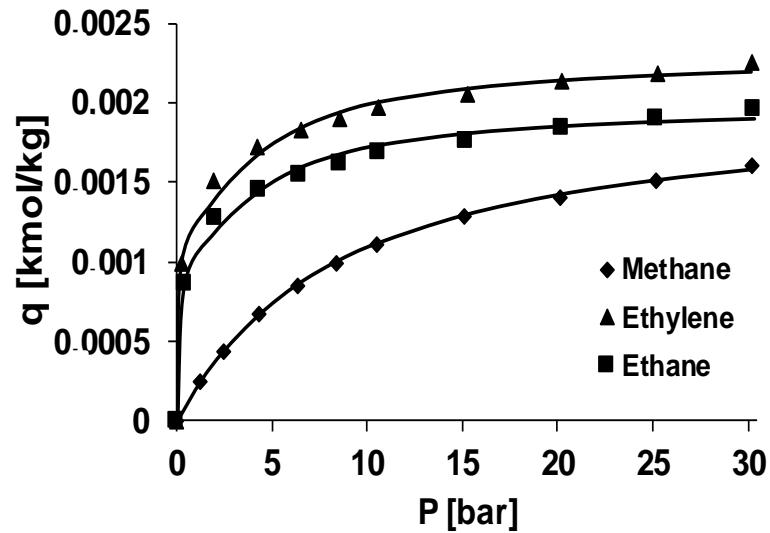


Figure 20. Adsorption isotherms for CH_4 , C_2H_4 and C_2H_6 on CaX zeolite at 298 K [45].

3.1.2 Mass transport model

The conservation equations in the mass balance considers terms for axial dispersion, convection, accumulation, flux to the solid surface, and no chemical reaction. A Material balance for component i over a pseudo-homogeneous differential volume element is depicted in Figure 21.

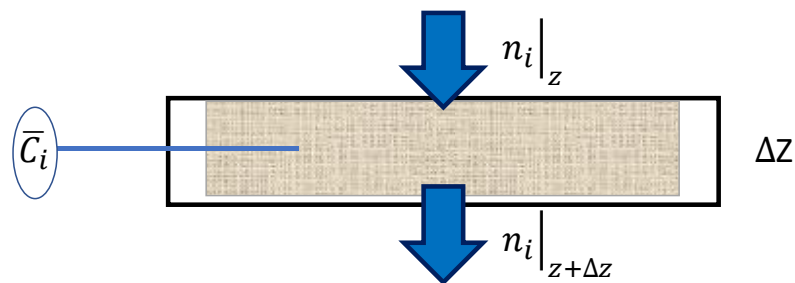


Figure 21. Control volume for mass material balance.

Inside the control volume the law of conservation of the mass must be satisfied.

$$\text{Accumulation} = \text{In} - \text{Out} \quad (19)$$

The accumulation term can be expressed as a difference between two intervals of time and the flow as the difference of two spatial points different.

$$(A \bar{C}_i \Delta Z)_{t+\Delta t} - (A \bar{C}_i \Delta Z)_t = (A n_i \Delta t)_Z - (A n_i \Delta t)_{Z+\Delta Z} \quad (20)$$

Due to the cross-sectional area (A) is constant along of the bed, this variable can be eliminated from Equation 20. On the other hand, when applying the limit when time (Δt) and length (ΔZ) tend to zero, it is possible obtained the following differential equation:

$$\frac{\partial \bar{C}_i}{\partial t} = - \frac{\partial n_i}{\partial Z} \quad (21)$$

Where, \bar{C}_i is the average concentration obtained by the following expression:

$$\bar{C}_i = C_{g,i} \epsilon_i + q_i \rho_B \quad (22)$$

If n_i is the flux of each component caused by macroscopic movement and axial diffusion:

$$n_i = C_{g,i} v_s + n_{diff,i} \quad (23)$$

When substituting the above terms in Equation 21, a differential equation is obtained:

$$\frac{\partial}{\partial t} (C_{g,i} \epsilon_i + q_i \rho_B) = - \frac{\partial}{\partial Z} (C_{g,i} v_s + n_{diff,i}) \quad (24)$$

Reorganizing terms, Equation 24 can be written as

$$\frac{\partial C_{g,i}}{\partial t} = - \frac{1}{\epsilon_i} \frac{\partial}{\partial Z} (C_{g,i} v_s) - \frac{1}{\epsilon_i} \frac{\partial}{\partial Z} n_{diff,i} - \frac{\rho_B}{\epsilon_i} \frac{\partial q_i}{\partial t} \quad (25)$$

Here, the molecular axial diffusion ($n_{diff,i}$) is defined by

$$n_{diff,i} = -\epsilon_i D_{az} C_g \frac{\partial y_i}{\partial Z} \quad (26)$$

Substituting the axial diffusion term in equation 25, the mass balance is expressed as

$$\frac{\partial C_{g,i}}{\partial t} = - \frac{1}{\epsilon_i} \frac{\partial}{\partial Z} (C_{g,i} v_s) + \frac{\partial}{\partial Z} (D_{az} C_g \frac{\partial y_i}{\partial Z}) - \frac{\rho_B}{\epsilon_i} \frac{\partial q_i}{\partial t} \quad (27)$$

If total concentration of the gas remains constant, equation 27 can be rearranged as

$$\frac{\partial y_i}{\partial t} = -\frac{1}{\epsilon_i} \frac{\partial}{\partial Z} (y_i v_s) + D_{az} \frac{\partial^2 y_i}{\partial Z^2} - \frac{\rho_B}{\epsilon_i c_g} \frac{\partial q_i}{\partial t} \quad (28)$$

Based on the gas ideal assumption ($C_g = P/RT$), equation 28 can be expressed as follow

$$-D_{az} \frac{\partial^2 y_i}{\partial Z^2} + \frac{1}{\epsilon} \frac{\partial (v_g y_i)}{\partial z} + \frac{\partial y_i}{\partial t} + \frac{\rho_s R T_g}{P \epsilon} \frac{\partial q_i}{\partial t} = 0 \quad (29)$$

Where:

$\left[\frac{1}{\epsilon} \frac{\partial (v_g y_i)}{\partial z} \right]$ is the convection term

$\left[\frac{\partial y_i}{\partial t} \right]$ is the accumulation term

$\left[\frac{\rho_s R T_g}{P \epsilon} \frac{\partial q_i}{\partial t} \right]$ is the flux on solid surface

For the final expression of mass balance, the gas velocity (v_g) is defined through of flow, the axial diffusion (D_{az}) is calculated by the correlation suggested by Wakao [47].

$$\frac{D_{az}}{v_s d_p} = \frac{20}{ScRe} + \frac{1}{2} \quad (30)$$

And values as solid density (ρ_s), pressure (P) and interparticle voidage (ϵ) are defined from operating parameters.

3.1.3 Energy balance

The energy balance considers contributions from axial effective heat conduction, convection, accumulation, and generation due to adsorption and desorption process. In addition, the energy model also assumes a constant cross-sectional area with insulated walls. The viscous dissipation as well as the kinetic and potential changes are neglected in the calculations. Then, the corresponding gas phase energy balance for a pseudo-homogeneous differential volume is depicted in Figure 22.

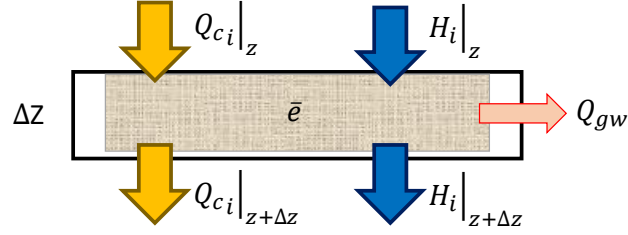


Figure 22. Control volume for gas phase energy balance

Based upon the same approach used in the material balance (Equation 20), the energy balance is deduced in differential terms as follow:

$$(A \bar{e} \Delta Z)_{t+\Delta t} - (A \bar{e} \Delta Z)_t + (A Q_c \Delta t)_{z+\Delta z} - (A Q_c \Delta t)_z + (A H \Delta t)_{z+\Delta z} - (A H \Delta t)_z = -Q_{gs} \Delta t - Q_{gw} \Delta t \quad (31)$$

Where, Q_{gs} and Q_{gw} are the heat transfer from gas phase to solid phase and the heat transferred by the gas to the wall, respectively. These expressions are defined by the following equations:

$$Q_{gs} = (HTC) a_p A \Delta Z (T_g - T_s) \quad (32)$$

$$Q_{gw} = (H_w) a A \Delta Z (T_g - T_w) \quad (33)$$

And Q_c is the heat conduction in the gas phase, and it is expressed by:

$$Q_c = -\varepsilon A K_g \frac{\partial T}{\partial Z} \quad (34)$$

As the cross-transversal area is constant, this can be factorized and cancelled. If the differential time and length elements tends to zero, the following differential equation is obtained.

$$\frac{\partial \bar{e}}{\partial t} + \frac{\partial q_c}{\partial z} + \frac{\partial H}{\partial z} + Q_{gs} + Q_{gw} = 0 \quad (35)$$

Here, the differential equation for enthalpy (H) and average energy density (\bar{e}) are given by

$$\frac{\partial \bar{e}}{\partial t} = \frac{\partial \bar{u}}{\partial t} = \varepsilon \rho_g C v_g \frac{\partial T_g}{\partial t} \quad (36)$$

$$\frac{\partial H}{\partial z} = \rho_g C_{vg} \frac{\partial T_g}{\partial z} \quad (37)$$

Substituting the terms of the previous equations (32-34 and 36-37) in the differential equation represented in equation 35, the gas phase energy balance is

$$-\varepsilon K_g \frac{\partial^2 T_g}{\partial z^2} + C_{vg} v_g \rho_g \frac{\partial T_g}{\partial z} + \varepsilon C_{vg} \rho_g \frac{\partial T_g}{\partial t} + (HTC) \alpha_p (T_g - T_s) + (H_w) a (T_g - T_w) = 0 \quad (38)$$

Where:

$\left[-\varepsilon K_g \frac{\partial^2 T_g}{\partial z^2}\right]$ is the thermal conduction

$\left[C_{vg} v_g \rho_g \frac{\partial T_g}{\partial z}\right]$ is the convection term

$\left[\varepsilon C_{vg} \rho_g \frac{\partial T_g}{\partial t}\right]$ is the accumulation term

$\left[(H_w) a (T_g - T_w)\right]$ is the environment transfer

$\left[(HTC) \alpha_p (T_g - T_s)\right]$ is the gas-solid transfer

From the gas phase energy balance, the constants of the thermal conduction, convention, accumulation terms are provided by Aspen Properties Software. The film heat transfer coefficient between the gas and the column wall (H_w) can be calculated as follow

$$H_w = \left(\frac{D_i}{2}\right)^{-1} \left[\frac{1}{\frac{D_i}{2} H_{wi}} + \frac{\ln\left(\frac{D_1}{D_i}\right)}{k_1} + \frac{\ln\left(\frac{D_0}{D_1}\right)}{k_2} + \frac{1}{\frac{D_0}{2} H_{w0}} \right]^{-1} \quad (39)$$

For the solid phase, the energy balance is expressed from the following control volume (see Figure 23):

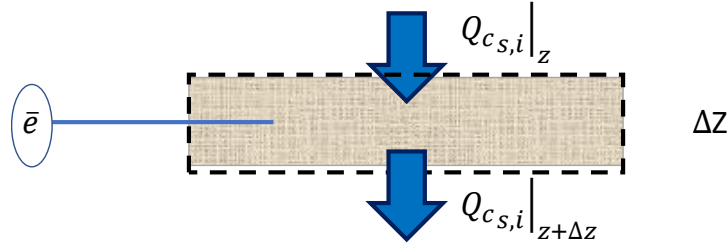


Figure 23. Control volume for solid phase energy balance

Where, the energy balance is deduced in differences terms as follow:

$$(A Q_c \Delta t)_{z+\Delta Z} - (A Q_c \Delta t)_z + (A \bar{e} \Delta Z)_{t+\Delta t} - (A \bar{e} \Delta Z)_t = Q_{sg} \Delta t \quad (40)$$

In equation 40, Q_{sg} is the heat transfer by solid to gas phase, which is given by

$$Q_{sg} = (HTC) a_p A \Delta Z (T_g - T_s) \quad (41)$$

By taking differential elements to zero, the following differential equation:

$$\frac{\partial q_c}{\partial z} + \frac{\partial \bar{e}_i}{\partial t} - (HTC) a_p (T_s - T_g) = 0 \quad (42)$$

The average energy density can be expressed by the amount of component i adsorbed on bed and the characteristic energy from adsorbent particles.

$$\bar{e}_i = \bar{u}_i \quad (43)$$

$$\bar{u}_i = \rho_s \widetilde{u}_s + \rho_s \widetilde{u}_{a,i} q_i \quad (44)$$

Replacing terms in equation 42, the solid phase energy balance is

$$\frac{\partial q_c}{\partial z} + \frac{\partial}{\partial t} (\rho_s \widetilde{u}_s + \rho_s \widetilde{u}_{a,i} q_i) - (HTC) a_p (T_s - T_g) = 0 \quad (45)$$

Next it is convenient to switch from internal energy to enthalpy to facilitate the handling of the equations.

$$\widetilde{u}_s = \widetilde{h}_s \quad (46)$$

$$\widetilde{u}_a = \widetilde{h}_a + \Delta H_{ADS} \quad (47)$$

Thus, the solid phase energy balance can be expressed as

$$\frac{\partial q_c}{\partial z} + \rho_s \frac{\partial \bar{h}_s}{\partial t} + \rho_s \frac{\partial}{\partial t} (h_a q_i + \Delta H_{ADS} q_i) - (HTC) a_p (T_s - T_g) = 0 \quad (48)$$

Here, the heat by conduction in the particle is defined by

$$q_c = -K_s \frac{\partial T_s}{\partial z} \quad (49)$$

Thus, the solid phase energy balance is

$$\begin{aligned} -K_s \frac{\partial^2 T_s}{\partial z^2} + \rho_s C_{p_s} \frac{\partial T_s}{\partial t} + \rho_s \left(\sum_{i=1}^n C_{pg_i} q_i \right) \frac{\partial T_s}{\partial t} + \rho_s \sum_{i=1}^n \Delta H_i \frac{\partial q_i}{\partial t} - (HTC) a_p (T_s - T_g) \\ = 0 \end{aligned} \quad (50)$$

Where:

$\left[-\varepsilon K_g \frac{\partial^2 T_g}{\partial z^2} \right]$ is the thermal conduction

$\left[\rho_s C_{p_s} \frac{\partial T_s}{\partial t} \right]$ is the accumulation term

$\left[\rho_s \left(\sum_{i=1}^n C_{pg_i} q_i \right) \frac{\partial T_s}{\partial t} \right]$ is the adsorbed phase

$\left[\rho_s \sum_{i=1}^n \Delta H_i \frac{\partial q_i}{\partial t} \right]$ is the adsorption term

$\left[(HTC) a_p (T_s - T_g) \right]$ is the solid-gas transfer

Here, the overall transfer coefficient (HTC) can be calculated by the following equation

$$HTC = j C_{pg} v_g \rho_g Pr^{-2/3} \quad (51)$$

Where, j is the Colburn factor, that is calculated using the following Reynolds-dependent correlations

$$j = 1,66 Re^{-0,51} \quad Re < 190 \quad (52a)$$

$$j = 0,983 Re^{-0,41} \quad Re > 190 \quad (52b)$$

The Reynolds number (Re) for particles is calculated with equation 53 [48]:

$$Re = \frac{v_g 2r_p M \rho_g}{\mu} \quad (53)$$

Where:

$[v_g]$ is the superficial velocity

$[\mu]$ is the gas phase dynamic viscosity

$[M]$ is the mean molecular weight

3.1.4 Momentum balance

The momentum balance is described by Ergun's equation that considers velocities changes and the pressure drop along the packed column. This equation is valid for laminar and turbulent flow, and this have been successfully applied to the modeling of pressure profiles within catalytic and adsorbent packed beds.

$$\frac{\partial P}{\partial z} = - \frac{1.5 \times 10^{-3} (1 - \varepsilon_i)^2}{(2r_p \psi)^2 \varepsilon_i^3} \mu v_g + 1.75 \times 10^{-5} M \rho_g \frac{(1 - \varepsilon_i)}{2r_p \psi \varepsilon_i} v_g^2 \quad (54)$$

3.1.5 Mass transfer rate

The adsorbate flux into the adsorbent can be described by using a linear driving force (LDF) model, incorporating a single lumped mass transfer parameter, as in Equation 55 [46, 47].

$$\frac{\partial q_i}{\partial t} = MTC(q_i^* - q_i) \quad (55)$$

As described before, the mass transfer coefficient is (MTC) is composed of three resistances that describe the effects in the external film, macropore region, and micropore region within the zeolitic material [28].

$$\frac{1}{MTC} = \frac{r_p}{3k_f} + \frac{r_p^2}{15 \varepsilon D_{eff}} + \frac{r_c^2}{15 \bar{K}_K D_C} \quad (56)$$

Here, k_f is the film or external resistance coefficient and it is obtained from the Sherwood number as [28]:

$$k_f = Sh \frac{D_{mol}}{2r_p} \quad (57)$$

The effective diffusivity (D_{eff}) consists of two diffusion mechanisms. One of them involves the collision among molecules in the large pores, namely molecular diffusion (D_{mol}). The other represents the collision between molecules and the pore wall; this is Knudsen diffusion (D_k). In addition, the effective diffusivity includes the ratio between the actual diffusion path length and the total distance that takes a diffusive molecule; this ratio is called tortuosity (τ_p). Thus, the diffusivity can be determined by the following equation [28], [50]:

$$\frac{1}{D_{eff}} = \tau_p \left(\frac{1}{D_m} + \frac{1}{D_k} \right) \quad (58)$$

D_c is the crystal diffusivity that can be determined from the Eyring equation [24].

$$D_c = D_{c0} e^{-\frac{Ea_i}{RT}} \quad (59)$$

And \bar{K}_K is the dimensionless Henry's coefficient obtained by [28]:

$$\bar{K}_{H_i} = \frac{\partial q_i^*}{\partial P_i} RT \frac{\rho_s}{\varepsilon} \quad (60)$$

For the model validation, the MTC parameter of each component is fixed with dynamic experimental data (breakthrough curves).

3.1.6 Model solution

As observed, the proposed dynamic model corresponded to a set of partial differential equations (PDE's) for mass, energy and momentum balances. For this reason, it is necessary to use a numerical method to solve them simultaneously. These PDE's can be converted into first-order ordinary differential equations by discretizing all the spatial variables using the method of centered finite differences. This is cataloged in the Aspen Adsorption numerical package as upwind differencing scheme 1 (USD1), and it is based on a first-order Taylor expansion, as presented below.

The finite differences method allows representing a fixed-bed into a mesh of discrete points (see Figure 24), called nodes, which have an average value of each variable in a specific point of the bed.

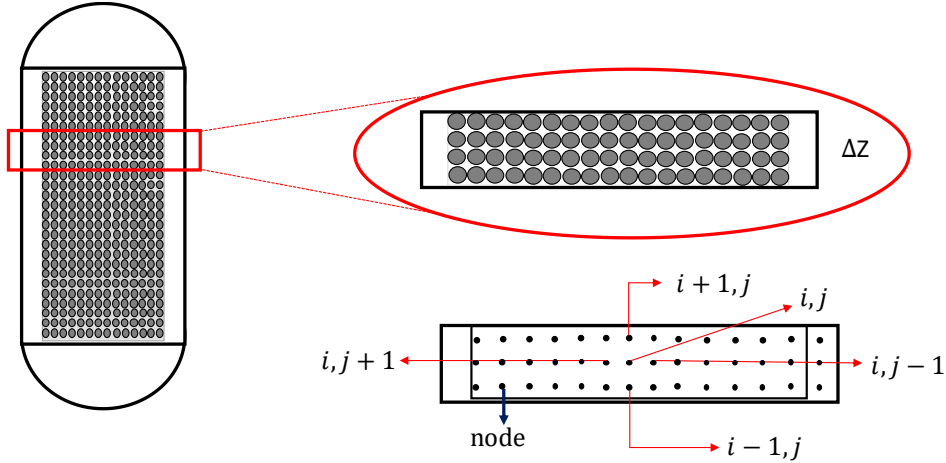


Figure 24. Representation of a fixed-bed into a mesh of discrete points.

In this sense, finite centered difference based on the differential element depicted in Figure 24 is defined as follows

$$\frac{\partial y_i}{\partial z} = \frac{y_i - y_{i-1}}{\Delta z} \quad (61)$$

The second-order term is approximated with a second-order accurate central differencing scheme [51].

$$\frac{\partial^2 y_i}{\partial z^2} = \frac{y_i - 2y_{i-1} + y_{i-2}}{\Delta z^2} \quad (62)$$

According to reports [9-12], this approach offers good numerical accuracy, stability, non-oscillatory and reduced simulation time. In order to define the required number of nodes, the outlet molar composition of the gas phase was obtained by integrating the mathematical model along the column, with a different number of nodes (20, 40, 60 and 80). A comparison with experimental breakthrough curves reported by Hosseinpour [35], allowed to define a suitable number of nodes for a proper representation of the adsorption process (see Figure 25).

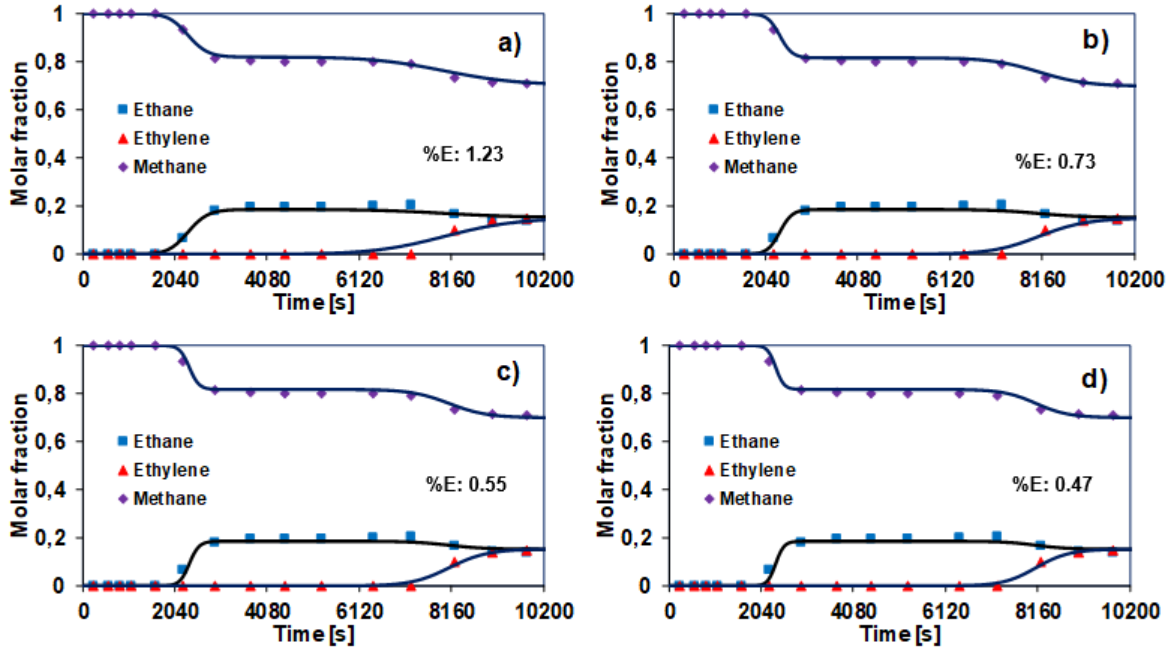


Figure 25. Breakthrough curves evaluated with different nodes: (a) 20 nodes; (b) 40 nodes; (c) 60 nodes and (d) 80 nodes. %E: Percentage of error.

According with preliminary results, the best agreement with experiments was obtained using 60 and 80 nodes. However, these two alternatives differ in the required calculation time. Therefore, considering the saving of computing time, an axial mesh of 60 nodes was used for subsequent simulations. This agrees with previous reports on the modeling of dynamic adsorption processes [44, 52]. During simulations in the Aspen Adsorption software, the absolute tolerance in calculations was set at 1×10^{-6} . The details of the model comparison with experimental data will be discussed in the next section.

The initial and boundary conditions used to solve the set of differential equations are presented as following:

- At the initial time ($t = 0$), the composition and amount adsorbed in the bed is equal to zero. The temperature of the gas and the bed, the gas velocity and the pressure, are the same as the feed conditions ($T_g = T_F$, $T_s = T_F$, $u = u_F$, $P = P_F$). However, when the time is different to zero the initial and boundary conditions change. These conditions are represented as limits in the control volume from Figure 26.

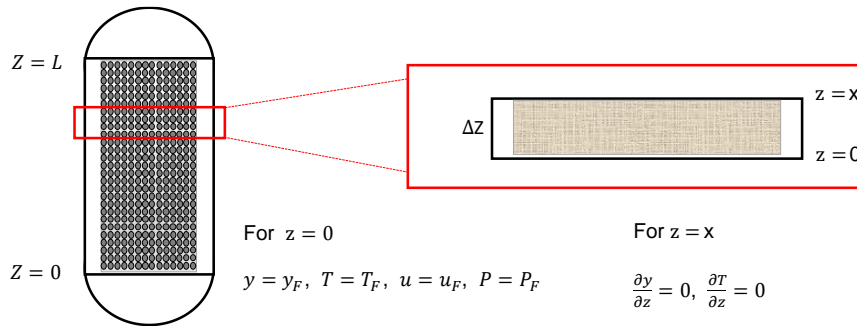


Figure 26. Representation of initial and boundary conditions in a fixed-bed.

- For $z = 0$, the composition (y), temperature (T), gas velocity (u) and pressure (P) take the value of the feed conditions (y_F, T_F, u_F , and P_F).
- For $z = x$, the composition and temperature take constant values ($\partial y/\partial z = 0$ and $\partial T/\partial z = 0$) because in that limit the bed achieve its saturation condition (maximum capacity of adsorption).

3.2 Model validation

As stated before, in order to validate the described model, experimental data on the dynamic adsorption of OCM gases on CaX zeolites were used. Because the data from our own experiments were only available for pure ethane and methane, and not for the ternary mixture (methane, ethane and ethylene), validation was done taking into account pilot scale breakthrough curves of OCM gases reported by Fatemi et. al [16]. The corresponding parameters, operating conditions, and geometric characteristics of the reported experiments are summarized in Table 13.

Table 13. Reported column specifications on the breakthrough experiments of OCM gases using CaX zeolite

Bed properties	
Bulk density	644.7 kg/m ³
Bed diameter	0.0127 m
Bed length	0.20 m
Particle density	1604 kg/m ³

Bed properties	
Inter-particle voidage	0.35
Specific heat capacity	1070 J/ kg K
Particle radius	1.6 -2.6 mm
Adsorption conditions	
Feed molar composition	
Methane	70%
Ethane	15%
Ethylene	15%
Feed flow	20 Nml * min ⁻¹
Pressure	1.013 bar
Temperature	308.15 K

As observed in Figure 27, the experimental multicomponent breakthrough curves are accurately described by the developed model. As expected from the reported adsorption isotherms, ethane and ethylene are adsorbed in larger degree than methane. Interestingly, there is also a higher selectivity for the olefin compared with the paraffin. This might indicate that the CaX zeolite molecular sieve could be a suitable separation agent for the OCM effluent gases. The breakthrough time of ethane and ethylene are observed ($y_i/y_{0,i} = 0.05$) at 2020 and 6920 seconds, respectively. In these breakthrough times the amount retained in the bed for ethane and ethylene are 7.52×10^{-4} mol and 2.58×10^{-3} mol, respectively. The mass transfer coefficient (MTC) and the isotherm parameter (IP_1) were used as a fitting parameter to address the mass transfer changes in the bed. The regressed parameters are summarized in Table 14.

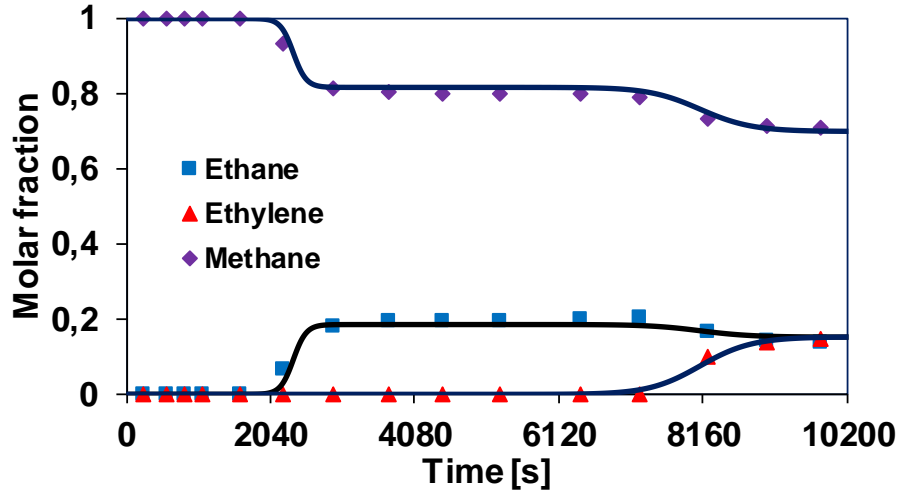


Figure 27. Breakthrough curves of methane, ethane and ethylene at 308 K [16].

Table 14. Adsorption equilibrium and kinetic parameters for PSA simulation using CaX zeolite

	$IP_1 \times 10^3$ [kmol/kg]	MTC [1/s]
C ₂ H ₆	0.30	0.1106
C ₂ H ₄	1.31	0.0241
CH ₄	0.01	0.2349

As expected, ethylene is preferably retained by the adsorbent due to the selective interaction between the calcium cation on the zeolite structure and ethylene. As ethylene has the highest electron density (see Figure 28), it interacts strongly with Ca²⁺ by the double bond (π). In addition, ethylene exhibits a selective adsorption on the CaX zeolite according to the result obtained from regression of IP1 parameter, where the multicomponent parameter (1.31) presents a close value to IP1 parameter for pure component (1.48). This indicates that the majority of the zeolite active sites contain ethylene molecules, and according to the assumptions of Langmuir model there is less adsorption capacity for ethane and methane due to each site can accommodate only one molecule.

Comparatively, the electron density of ethane is lower, which generates a minor interaction with the zeolite. This is supported with the intermediates values of the parameters fixed (IP1= 0.30 and MTC=0.1106), which it indicates that the amount adsorbed is lower than ethylene.

On the other hand, methane has minimal interaction with the alkaline cation, showing a rapid convective transport along the column. This agrees when comparing the heats of adsorption of each component presented in Table 12, which increase with the presence of double bonds or polar groups in the molecule, as mentioned by Ruthven [46].

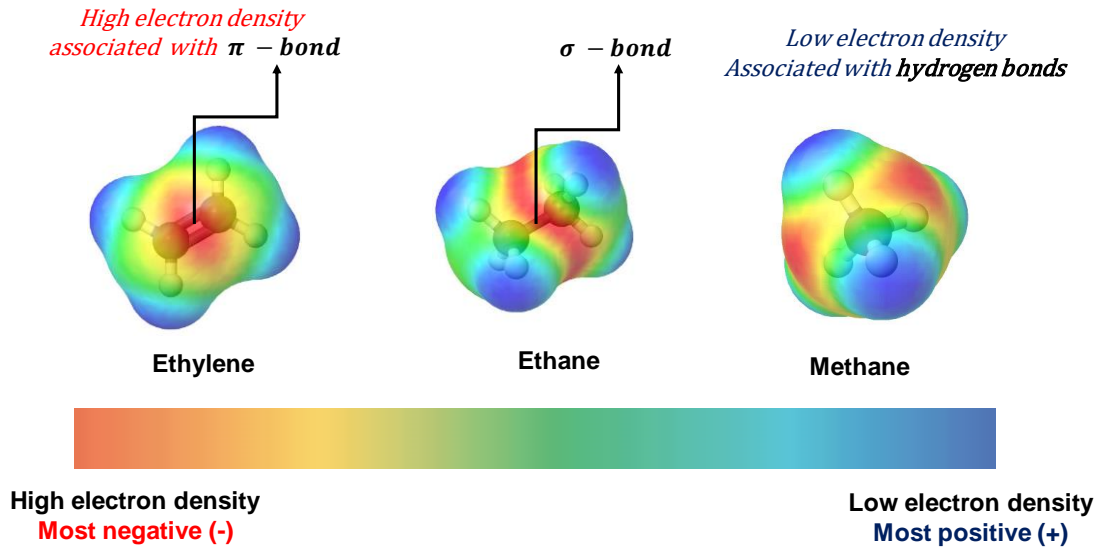


Figure 28. Electrostatic maps of ethylene, ethane and methane.
Electrostatic maps taken from [55]

The calculated MTC includes all mass transfer resistances (external film, macropore, and micropore), however, the individual resistances should be evaluated to determine which of those is the limiting one. These mass transfer resistances were determined through equation 56 – 60 and the following correlations:

For the calculation of the external resistance a correlation proposed by Wakao and Funazkri [56] is used. This is valid for mass transport of molecules within the bulk fluid, and the diffusion through the stagnant fluid surrounding a particle of diameter $D_p = 2R_p$. This correlation is given by

$$Sh_i = 2 + 1.1 Sc_i^{\frac{1}{3}} Re^{0.6} \quad (63)$$

Where the Reynolds number (Re) is determined by equation 53 and the Schmidt number is given by

$$Sc_i = \frac{\mu}{D_{m,i} \rho_s} \quad (64)$$

For macropore resistance, molecular diffusion (D_m) and Knudsen diffusion (D_k) are calculated in order to obtain the effective diffusion, as is present in equation 58. In that sense, D_m and D_k are determined as follow

$$D_{m,i} = D_{1m} = (1 - y_1) \left(\sum_{j=2}^n \frac{y_j}{D_{1,j}} \right) \quad (65)$$

And, molecular diffusion ($D_{1,j}$) is expressed in m/s as

$$D_{1,j} = \frac{(1.858 \times 10^{-7}) T^{0.5} \left(\left(\frac{1}{M_{w,A}} \right) + \left(\frac{1}{M_{w,B}} \right) \right)^{\frac{1}{2}}}{P \sigma_{AB}^2 I} \quad (66)$$

Where, σ_{AB} is the collision diameter in Angstrom

$$\sigma_{AB} = \frac{\sigma_A + \sigma_B}{2} \quad (67)$$

These parameters σ can be found in Table B-1 of Bird et al. (1960) [57]. I is a dimensionless function of temperature, which can be determined by

$$I = \frac{A}{(T^*)^B} + \frac{B}{\exp(DT^*)} + \frac{E}{\exp(FT^*)} + \frac{G}{\exp(HT^*)} \quad (68)$$

Where the constants (A-H) are obtained from Reid et al. [58]

$$A = 1.06036; \quad B = 0.15610; \quad C = 0.19300; \quad D = 0.47635; \quad E = 1.03587;$$

$$F = 1.52996; \quad G = 1.76474; \quad H = 3.89411$$

After evaluating the external and macropore resistances with reported correlations, the remaining micropore resistance can be evaluated using the regressed value of the MTC. The corresponding results presented in Figure 3 indicate that the mass transfer is governed

by macropore and micropore resistance. However as expected, ethylene adsorption is governed by micropore resistance because it is retained on the surface of the zeolite within the micropores.

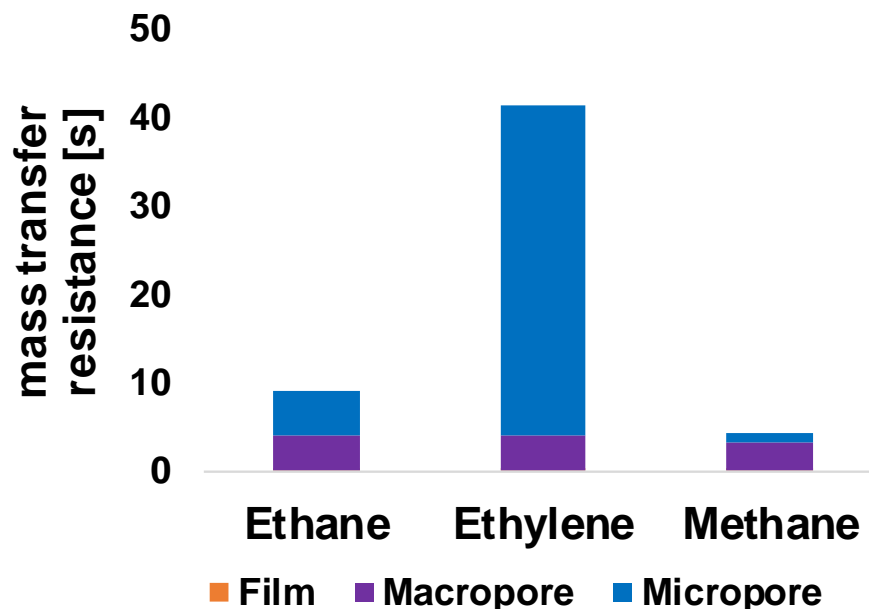


Figure 29. Individual mass transfer resistances as a percentage of the overall resistance.

The maximum adsorption capacity of ethane and ethylene was evaluated by integration of the breakthrough curve. This was done to verify that the calculation obtained with the Aspen Adsorption software was consistent with the adsorption isotherm measured at 1.01325 bar. These values are summarized in **Table 15**.

Table 15. Maximum adsorption capacity for CaX zeolite at 1.01325 bar.

	Maximum adsorption capacity evaluated with the Langmuir model at 1.01325 bar 1 (Eq. 17)	Maximum adsorption capacity obtained with Aspen Adsorption v.9 to 1.01325 bar
C ₂ H ₆	6.816×10^{-4}	6.817×10^{-4}
C ₂ H ₄	2.957×10^{-3}	2.957×10^{-3}
CH ₄	5.775×10^{-5}	5.775×10^{-5}

As observed in Table 15, the CaX zeolite exhibits a selectivity for ethylene that is four times larger than that for ethane. This is also consistent with the ratio of heats of adsorption, as shown below:

$$\frac{\Delta H_{ads,C_2H_4}}{\Delta H_{ads,C_2H_6}} = \frac{-29783 \text{ kJ/mol}}{-25956 \text{ kJ/mol}} = 1.15$$

The obtained model was also validated with available experimental data from a cooperation project between the National University of Colombia and the Technical University of Berlin. These experimental data were measured in the Mini-Plant OCM from the Thermodynamics and Refrigeration Laboratory of the TU Berlin, which is discussed in detail in the report of Garcia [59]. The specifications of the bed to carry out the modeling in the Aspen Adsorption software are summarized in Table 16.

Table 16. Column specifications for column fixed bed using CaX zeolite

Bed properties	
Bulk density	479 kg/m ³
Bed diameter	0.9 m
Bed length	0.05 m
Particle density	941 kg/m ³
Inter-particle voidage	0.48
Intra.particle voidage	0.2432
Specific heat capacity	1070 J/ kg K
Particle radius	4 mm

The first set of dynamic data consists of a breakthrough curve of ethane diluted in nitrogen (inert) measured under the conditions reported in Table 17.

Table 17. Adsorption condition for ethane breakthrough curve

Adsorption conditions	
Feed molar composition	
Methane	18.85%

Adsorption conditions	
Nitrogen (inert)	81.15%
Feed flow	7.44×10^{-7} kmol/s
Pressure	2 bar
Temperature	303.15 K

The modeling of the breakthrough curve was carried out in the same way as presented in the previous section, using the conditions in Table 17. As shown in Figure 30, the proposed model agrees reasonably well with the observed composition profiles from the Mini-Plant OCM.

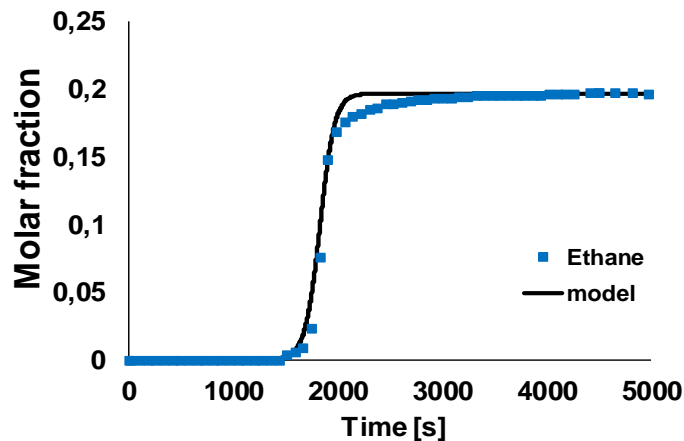


Figure 30. Ethane breakthrough curve at 303.15 K and 2 bar.

The fitted parameters (IP_1 and MTC) obtained from the regression of the experimental data with the proposed model are presented in Table 18.

Table 18. Adsorption equilibrium and kinetic parameters obtained from ethane breakthrough curve.

	$IP_1 \times 10^3$ [kmol/kg]	MTC [1/s]
C_2H_6	1.13	0.274

Here, the value of parameter IP_1 fitted (1.13) has a close value to IP_1 parameter from pure component (1.23). This is because ethane diluted in nitrogen present a behavior of pure

component owe to nitrogen is inert in the zeolite and all active sites are available for ethane molecules. The slight variation between the above values can present due to the slight differences between the CaX zeolite from Fatemi [16] and the CaX zeolite from BIOCM project.

The second set of experimental data was measured using methane diluted in nitrogen at different pressures (2 and 5 bar), as presented in Table 19.

Table 19. Adsorption condition for methane breakthrough curve at 2 bar.

Adsorption conditions		
Feed molar composition		
2 bar	Methane	18.85%
	Nitrogen (inert)	81.15%
5 bar	Methane	18.13%
	Nitrogen (inert)	81.87%
2 and 5 bar	Feed flow	7.44×10^{-7} kmol/s
	Temperature	303.15 K

In Figure 31 it is presented a comparison between the experimental data from the mini-plant and the corresponding simulation of the simulated breakthrough curve. Figure 31 (a) shows that the proposed model proposed fit well the experiments. However, in Figure 31 (b), the model presents a slight deviation in comparison of experimental data in the first seconds. The corresponding parameters (IP1 and MTC) from the dynamic adsorption experiments with methane are presented in

Table 20. Results obtained from the regression confirms that methane is not adsorbed on the bed, which indicates that the CaX zeolite is an alternative for the demethanization process during OCM downstream processing.

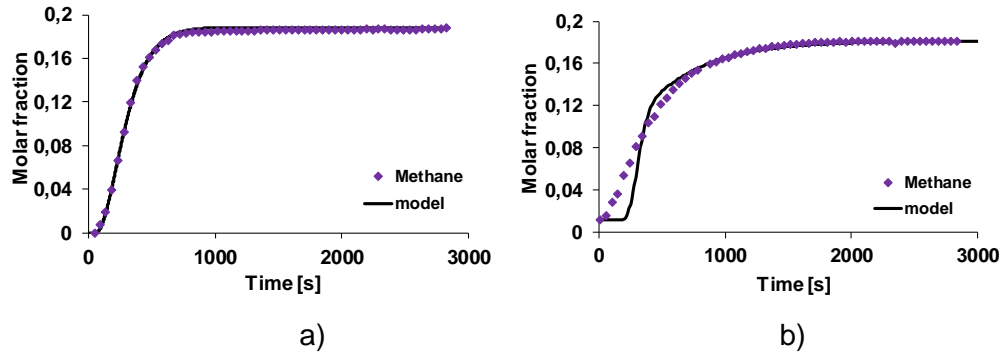


Figure 31. Methane breakthrough curves at 303.15 K: a) 2 bar and b) 5 bar.

Table 20. Adsorption equilibrium and kinetic parameters obtained from methane breakthrough curves.

	$IP_1 \times 10^3$ [kmol/kg]	$MTC \times 10^2$ [1/s]
2 bar	0.02	0.269
5 bar	0.04	1.45

Based on the above results, at high pressure the mass transfer coefficient increase. This has a similar behavior to the results reported by Sarker [60], where the equilibrium and kinetic behavior onto different adsorbent materials were evaluated. Sarker mentioned that at low pressure the MTC decrease due to adsorption occurs on adsorption sites with strong energy barriers, however, at high pressure the MTC rises because the adsorption takes place on the sites with weak energy barriers.

3.3 Pressure Swing Adsorption (PSA) process operation

In the previous sections it was verified that CaX zeolite can be used as adsorbent material for methane removal in effluent streams from an OCM reactor. In this regard, a dynamic simulation was carried out to study the performance of a PSA unit, in the separation of OCM effluent gases using CaX zeolite as adsorbent. The operating parameters were established taking into account the outlet conditions of the purification section. The packed bed size was established to maximize the adsorption working capacity, and to reduce the wear in the zeolites, as described in the following section.

3.3.1 Feed composition

The feed flow of the study mixture was based upon a reported model of the OCM process at a commercial scale [3]. However, the amounts of the gases were defined according to the compositions proposed by research partners at Technische Universität Berlin, which are reported in Table 21.

Table 21. Molar composition for OCM effluent gases based on Stansch Reaction.

Component	Molar composition
Methane	0.730
Ethylene	0.097
Ethane	0.036
Hydrogen	0.104
Carbon dioxide	0
Carbon monoxide	0.025
Water	0
Nitrogen	0.008

In this study, only methane, ethane, nitrogen and ethylene were considered. As mentioned before, the other gases were not taken into account for the following reasons: hydrogen does not interact with the zeolite, carbon dioxide is removed in the purification section, and carbon monoxide is only slightly adsorbed [41], and it is very diluted in the gas mixture. Although methane is slight adsorbed, it was included because it is present at high concentrations due to the low conversion in the OCM reaction. On the other hand, nitrogen is an inert component that comes from the air used in the oxidation reaction, and it was included in the experiments described in the previous section. The amount of each component in the study mixture was determined from the commercial scale flow (5931.54 kmol/hr) reported by Salerno [3], as presented in the following table:

Table 22. Commercial flow and molar compositions

Component	Flow [kmol/hr]	Molar composition	Flow in study mixture [kmol/ hr]	Molar fraction in study mixture
Methane	4330.03	0.730	4330.03	0.8381

Component	Flow [kmol/hr]	Molar composition	Flow in study mixture [kmol/ hr]	Molar fraction in study mixture
Ethylene	575.36	0.097	575.36	0.1114
Ethane	213.54	0.036	213.54	0.0413
Nitrogen	47.45	0.008	47.45	0.0092
Hydrogen	616.88	0.104	-	-
Carbon monoxide	148.29	0.025	-	-
Carbon dioxide	0	0	-	-
Water	0	0	-	-

3.3.2 Temperature

The operating temperature was defined taking into account the temperature from available experimental data (Breakthrough curve and adsorption isotherms), both at 308 K. Taking into account that the outlet temperature of the stream from the purification section is 318.15 K, it is necessary to cool it down to 308.15 K to feed the PSA columns.

3.3.3 Pressure

Pressure is a key parameter in the design of PSA systems owe to its direct impact on adsorption and desorption equilibrium; the larger the pressure the higher the adsorption capacity. In that sense, to use of the high pressure of the outlet stream from purification section (8.8 bar) is convenient for ethylene adsorption, as this saves energy in the downstream processing. On the other hand, it is necessary to employ a low pressure to regenerate the bed, which in this case is the atmospheric pressure (1.01325 bar).

3.3.4 Size

The size of the industrial scale adsorption column was determined through evaluation of the length of the unused bed (LUB), as described in the chapter 2. In this case, different column sizes are evaluated in terms of diameter and height. Then, the column size with the better performance (i.e. the minor fraction of unused bed) was selected. The LUB is determined with Equation 69, and results are summarized in Table 23.

$$LUB = \left(1 - \frac{t_b}{t^*}\right) \times L \quad (69)$$

The values of the breakthrough time (t_b) and symmetrical time (t^*) were obtained from the ethylene composition profile at $C/C_0 = 0.05$ and $C/C_0 = 0.5$, respectively. These times were evaluated with different diameters and heights, as presented in Table 23. The ethylene composition was used as reference because it is the higher value-added component in the OCM effluent mixture. The minor fraction of unused bed was obtained with a bed diameter of 2 meters and a bed length of 9 meters. With this geometry, 91.2% of the bed is used for ethylene adsorption and the remaining 8.8% corresponds to the unused mass transfer zone (MTZ), as represented in Figure 32.

Table 23. Percentage of unused bed.

Diameter [m]	Height [m]	t_b	t^*	LUB	Percentage of Unused bed
1.3	1,5	720	930	0,33	22.0
1.5	2	1420	1670	0.30	20.0
1.8	2	2110	2410	0.25	13.9
2	2	1710	1977	0.27	13.5
1.5	9	2690	3010	0.95	10.6
1.8	9	3960	4345	0.79	8.8
2	9	4080	4470	0.79	8.8

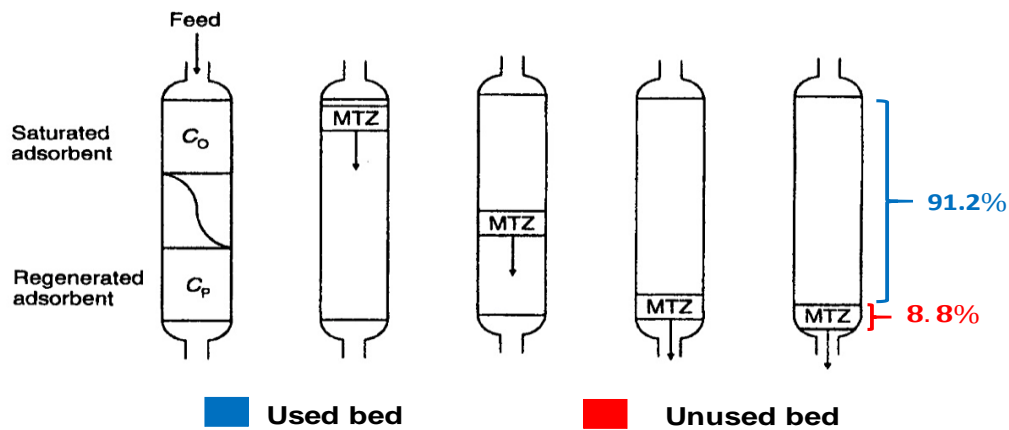


Figure 32. Schematic representation of LUB using a diameter of 2 m and a height of 9m. Adapted from Thomas and Barry Crittenden [61]

Despite other columns with larger dimensions can be determined, these exceed the typical column sizes encountered in industrial applications [60, 61]. Larger sizes could generate a substantial rise in capital costs due to the expensive requirements in platforms, soil settlement, and installation. Once the column diameter was established, the feed flow within the column can be calculated through superficial velocity. This velocity is a fundamental parameter used to mitigate the wear of pellets owe to high pressure drop. In the industrial operation, fixed bed columns with a height of 4 meters allows a maximum drop pressure of 1 psi (0.017237 bar/m) [44]. Nevertheless, the superficial velocity can be estimated from an energy-mechanical balance (see Annex A), where the limiting mechanical stress over the bed is at the point of fluidization. The onset fluidization occurs when the pressure drop across the bed is equal to the weight of the bed per area unit; at this point the wear of the bed is critical. In that regard, some authors proposed that the superficial velocity must be 80% less than the minimum fluidization velocity [46]. The minimum fluidization velocity (u) can be determined solving the following equation.

$$\left(1.75 \frac{\rho_f}{D_p \varepsilon_i^3}\right) u^2 + \left(150 \frac{(1 - \varepsilon_i) \mu_f}{D_p^2 \varepsilon_i}\right) u + (-g(\rho_s - \rho_f)) = 0 \quad (70)$$

Due to the adsorption column operates at 8.8 bar, it is necessary to determine the thickness of the column under the dimensions that have already been established above. Therefore, the cylindrical wall thickness is estimated taking into consideration the operating pressure and material losses by corrosion, as is presented in Eq. 71.

$$t_w = t_p + t_c \quad (71)$$

Where the thickness required for operating pressure is computed from the ASME pressure vessel equation:

$$t_p = \frac{P_d D_i}{2 S E - 1.2 P_d} \quad (72)$$

And, the thickness by corrosion effects is determined based on the thickness by operating pressure (t_p), which can be assumed to come in the following increments [64]:

1/16-in increments for t_p between 3/16 and 1/2 in

1/8-in increments for t_p between 5/8 and 2 in

1/4-in increments for t_p between 2 ¼ and 3 in

The values of the maximum allowable stress (S) depends on the design temperature, as it is reported in the following table.

Table 24. Maximum allowable stress [64]

Temperature [°F]	Maximum allowable stress [psi]
-20 to 650	15000
700	15000
750	15000
800	14750
850	14200
900	13100

On the other hand, the value of the weld efficiency (E) is 0.85.

Sandler and Luckiewicz [65] recommend that the internal design pressure (P_d) should be greater than operating pressure ($P_0 = 8.8 \text{ bar}$ or 127.63 psi).

$$P_d = \exp \left[0.60608 + 0.91615 (\ln(P_0)) + 0.0015655 (\ln(P_0))^2 \right] \quad (73)$$

The different parameters of the PSA unit are summarized in Table 25. These will be used in the simulation of the de-methanizing process.

Table 25. Column and adsorbent characteristics

Column parameter	value	
bed height [m]	9.0	
bed diameter [m]	2.0	
Wall thickness [m]	0.0127	
high-pressure [bar]	8.8	
low-pressure [bar]	1.01325	
feed molar composition:	Methane	0.8381
	Ethane	0.0413
	Ethylene	0.1114
	Nitrogen	0.0092

Column parameter	value
Adsorbent parameters	CaX zeolite
bed porosity	0.35*
wall heat transfer coefficient [w/m ² K]	3.33
bed density [kg/m ³]	644.7*
heat transfer coefficient [W/m ² K]	28-38*
pellet porosity	0.383
pellet radius [m]	0.0022
solid specific heat [J/kg K]	1070
adsorbent shape factor	0.99
particle density [kg/m ³]	1604*

* taken from Salmasi [16]

The design of the separation process will be discussed in the next chapter, as well as the implementation in the Aspen Adsorption[®] software.

4. Chapter four: Simulation process of the downstream section in the OCM process

The fundamentals of adsorption were covered in previous chapters, discussing the role of the adsorbent and its properties, and providing an understanding of the phase equilibrium and transport phenomena involved in the process. Also, a description of the OCM process was presented, recognizing the importance of developing enhanced separation processes for the separation of olefin/paraffin mixtures. Later, based upon experimental data, it was established that CaX molecular sieve is a suitable material for the adsorption separation of effluent gases from the OCM process. Finally, a model of the adsorption process using the zeolite based molecular sieves was implemented in a commercial software (Aspen Adsorption[®]), and the corresponding parameters were adjusted to fit experimental observations. Thus, this chapter is mainly focused on the dynamic simulation, up-scaling and preliminary economic evaluation of the implementation of a pressure swing adsorption process for the downstream separation of OCM effluents

With respect to the preliminary results, the zeolite CaX molecular sieve retains ethane and ethylene and separate them from methane. However, because the adsorbent material presents low selectivity for ethane and ethylene separation, the olefin can be later separated by a de-ethanizer column that allows to fulfill the required ethylene purity for polymer applications (99.9%).

4.1 Pressure swing adsorption process

The dynamic simulation of the pressure swing adsorption (PSA) process applied in the downstream separation of OCM effluents was implemented in Aspen Adsorption. The simulation was carried out to assess the performance of a single fixed bed column in an entire PSA cycle. Physicochemical, equilibrium and transport parameters used in

simulations were obtained in the previous chapter. Operating conditions were also defined according to preliminary results, reported data, commercial specifications of the products, and the corresponding conditions of the OCM process. Initially, it was assumed that the feed gas flow was coming from the purification section after CO₂ removal (See Figure 2 in chapter one), at 8.8 bar and 35°C. The fixed bed column specifications were determined according to the described operational parameters presented in last chapter. PSA was used for methane removal and ethylene/ethane purification was done as in the conventional cryogenic separation.

4.1.1 Implementation in Aspen Adsorption®

An industrial scale de-methanizing PSA unit consists of two coupled adsorption columns managed through an advanced control system. However, a single-bed approach was used to make the model configuration simpler and to save computational time while retaining the accuracy of the results. The single bed column model was implemented in Aspen Adsorption v.9 according to the steps presented in Figure 33. In the Aspen Adsorption interface, as a first step, the package of physical and thermodynamic properties of the components involved in this study should be defined through Aspen Properties module. In step 2, the flowsheet is created, which consists of the incorporation of columns, streams, valves and the tool of the control system (cycle organizer). Once the flowsheet is defined, in step 3 the mathematical model is set together with the conditions and properties required to carry out the process simulation. In step 4, the initial conditions of the bed are established in order to start the calculations of the discretization model. In step 5, the events of the adsorption cycle are scheduled (operation steps: adsorption, depressurization, purge and repressurization), as well as the specification of the valves controlling in each step. At the end of the cycle configuration, step 6 consists of activating and generating the cycle to later execute the simulation (step 7). In step 8, the material and energy balances can be generated is each cycle and PSA step, as a result of the simulation of the adsorption column.

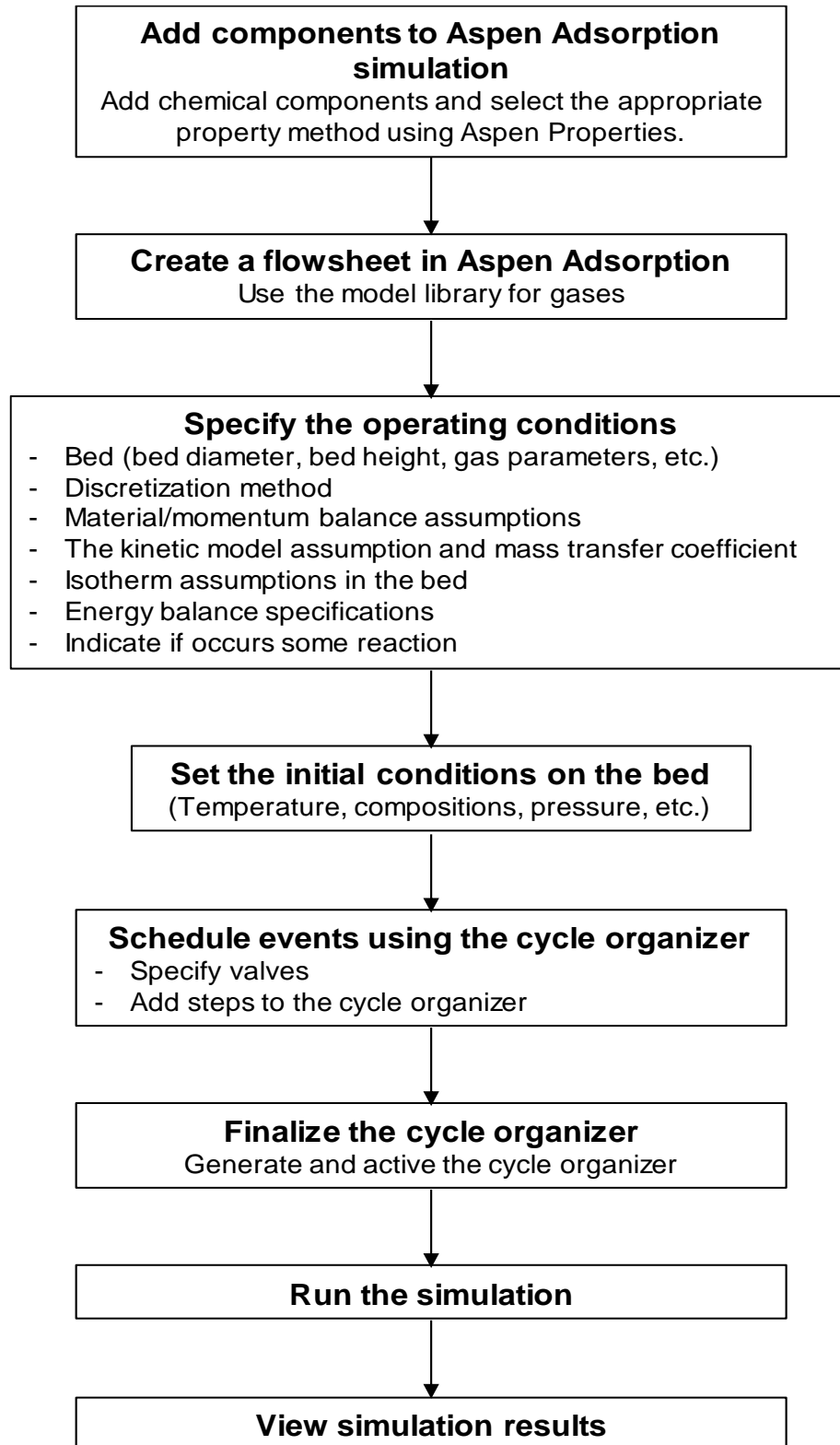


Figure 33. General procedure for simulating PSA columns in Aspen Adsorption

4.1.2 Separation of methane from ethane/ethylene mixture

As stated in chapter 3, the simulation of the dynamic process is carried out under the conditions presented in Table 25. In the separation of methane from the ethane / ethylene mixture, the olefin is strongly adsorbed in the bed, therefore it is necessary to recover the ethylene (component of commercial interest), and also to regenerate the bed for further adsorption. The PSA cycle used in the separation is based on the Skarstrom cycle, as presented in the next section.

Pressure swing adsorption using Skarstrom cycle

The PSA cycle for the methane separation and ethylene recovery process consists of 4 steps: Pressurization, adsorption, depressurization and purge, as shown in Figure 34. This cycle allows the separation of methane at high pressure (8.8 bar) by feeding the mixture of effluent gases through the bed. The ethylene adsorbed at high pressure are recovered in the regeneration of the bed, which begins with the process of depressurization and countercurrent purge at low pressure (atmospheric pressure).

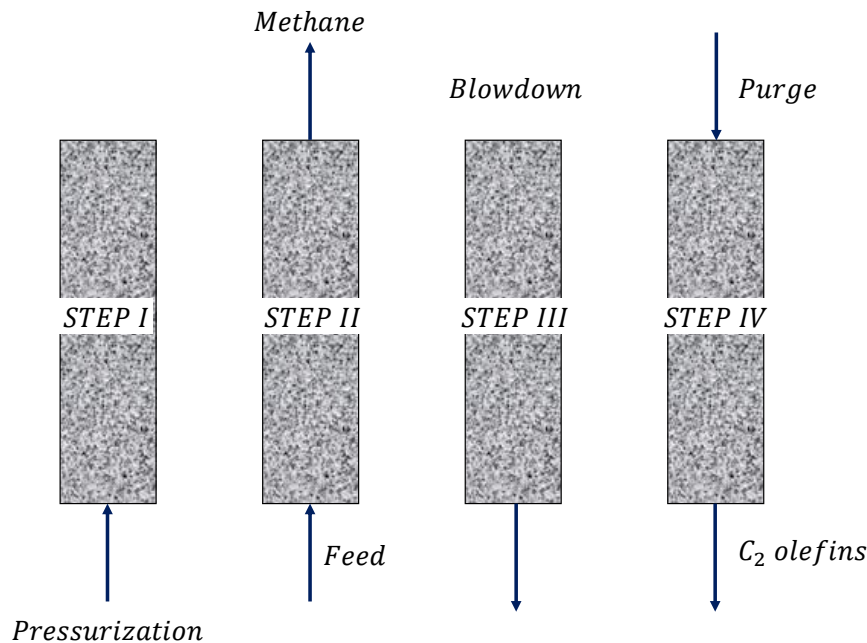


Figure 34. Steps used in the PSA cycle for the separation of methane from C₂ components

The PSA process used in this study begins with pressurization of the bed (Step 1). There, the PSA column is fed with the feed gas until it reaches the high operating pressure (8.8

bar), as shown in Figure 35. Step 2 consists of feeding the OCM gases at 8.8 bar, where the methane and nitrogen passes through the bed while ethane and ethylene are adsorbed (see Figure 36). In step 3, the bed regeneration process begins by depressurizing the column at an intermediate pressure (see Figure 37). To end the PSA cycle, step 4 involves purge at low pressure (atmospheric pressure) to remove the ethane and ethylene present in the voidage of the column and the macropores of CaX zeolite, as shown in Figure 38.

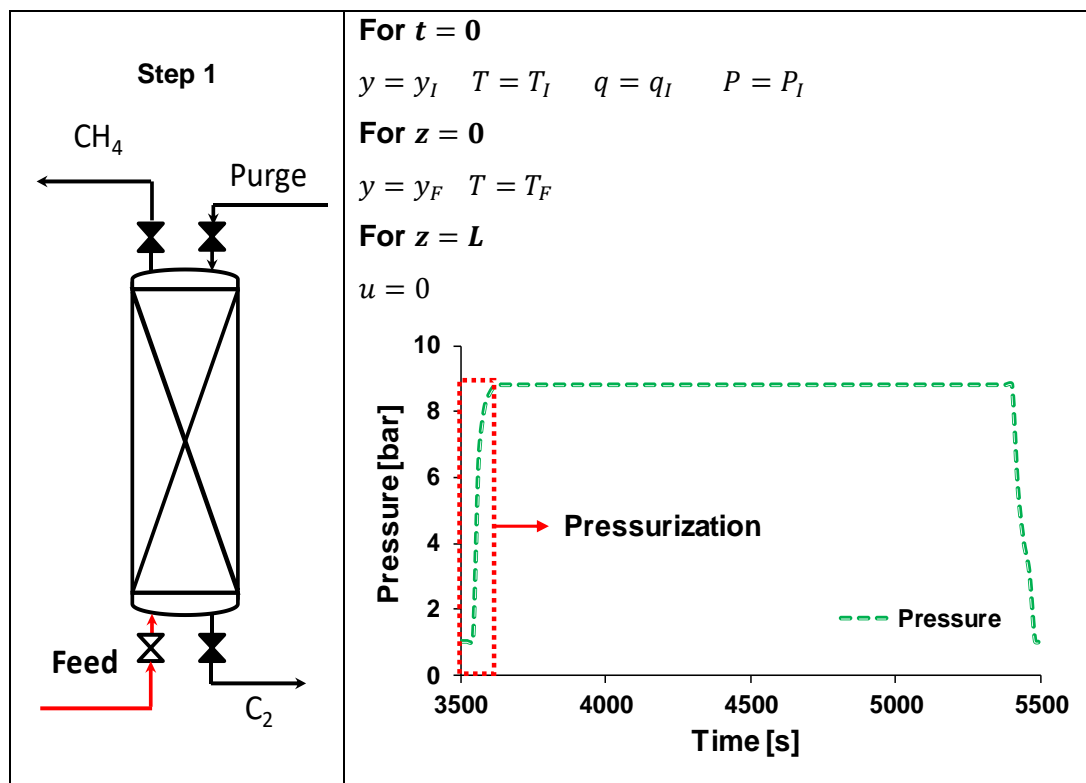


Figure 35. Step 1: Bed pressurization at 8.8 bar

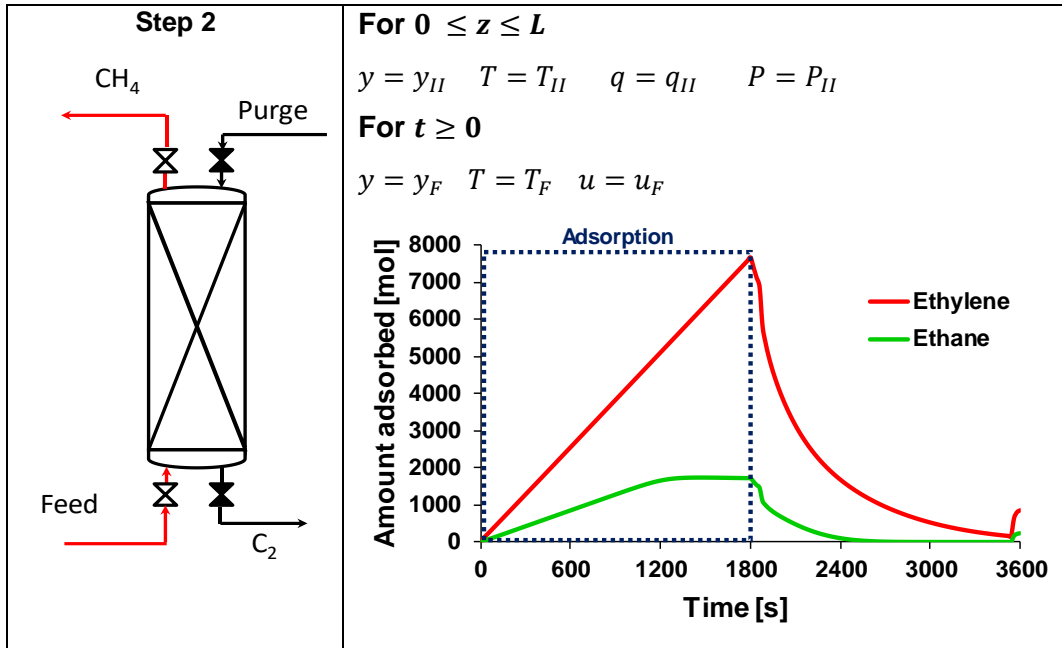


Figure 36. Step 2: Separation of methane from olefin mixture by adsorption of ethane and ethylene.

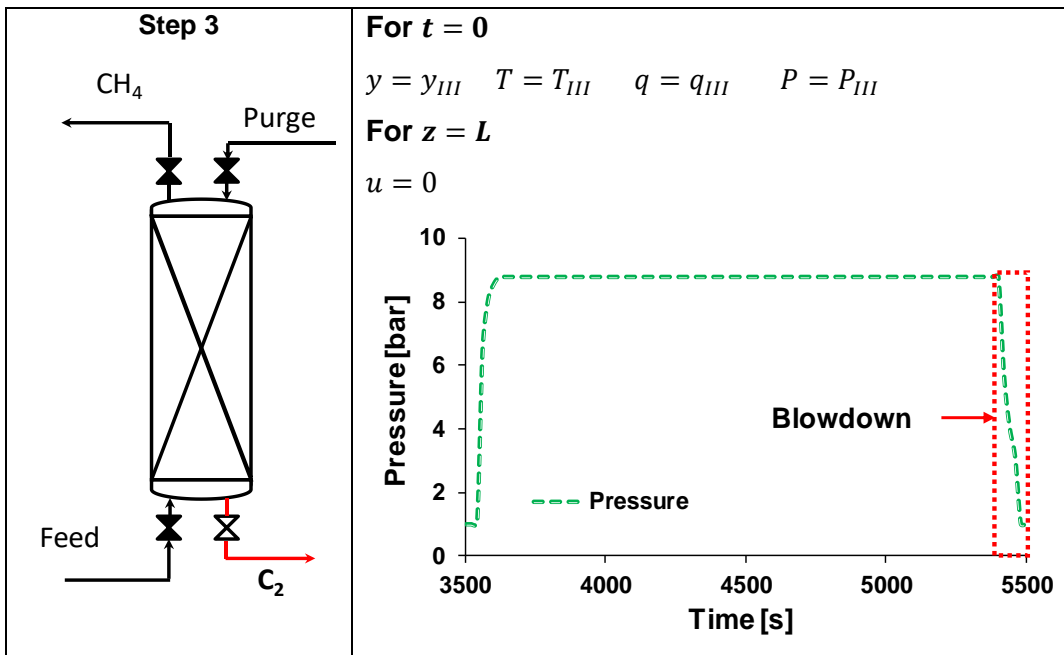


Figure 37. Step 3: Blowdown of the bed

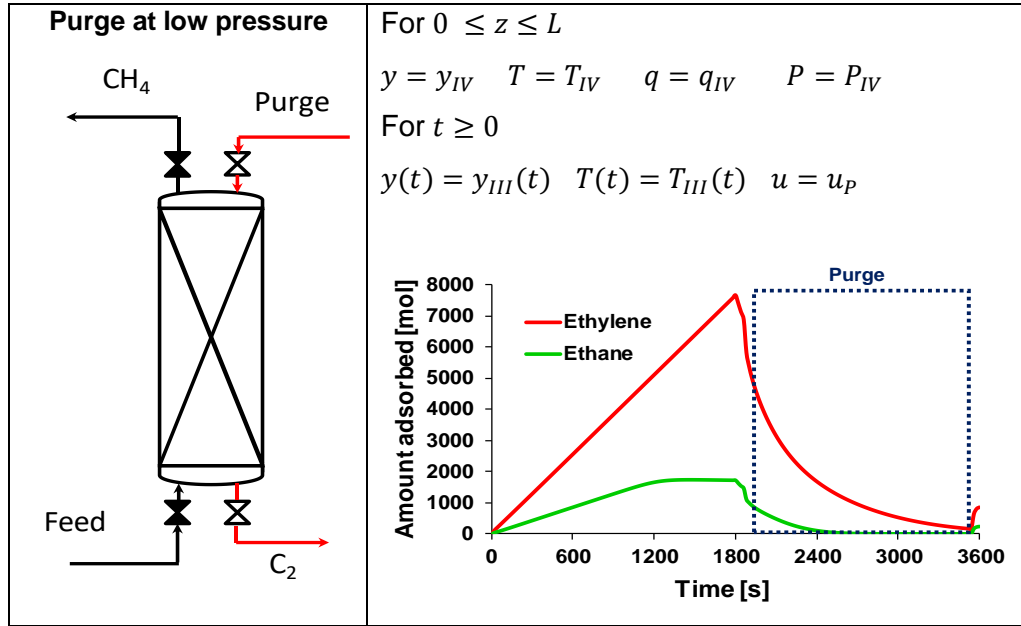


Figure 38. Step 4: Desorption of strongly adsorbed components at atmospheric pressure.

These sequential steps were defined based upon the ethylene purity requirements for polymer application (99.9% Purity). However, PSA performance was run under different operating conditions to assess the impact on OCM gases purity and recovery. These last variables are defined according to the following expressions

$$Purity = \frac{\text{Moles of the component in the product stream, in a cycle}}{\text{Total moles in the product stream, in the same cycle}} \quad (74)$$

$$Recovery = \frac{\text{Moles of the component in the product stream, in a cycle}}{\text{Moles of the component entering the bed, in the same cycle}} \quad (75)$$

Parametric study

The performance of the PSA process was studied under different operating conditions. However, some parameters were fixed to facilitate the comparison among experiments and to match conditions of the OCM process. Feed composition, temperature, pressure, and

adsorption time were kept constant during simulations. Because the aim of the OCM process is to produce ethylene for commercial purposes and it is strongly adsorbed in the CaX zeolite, the main variables that are involved in the regeneration process were studied. These corresponded to pressurization time, feed flow, and purge flow. Particularly, the feed flow was defined in Chapter 3 and it cannot be processed in one single column. In this regard, several parallel units are required to carry out the separation of the industrial scale flow proposed in chapter 3. Therefore, it is necessary to evaluate the operating flow based upon the adsorption time set for this study (1800 seconds). In Figure 39, different feed rates are evaluated with respect to ethane and ethylene losses due to bed saturation. This helps establishing the allowed flowrate of each one of the parallel PSA units.

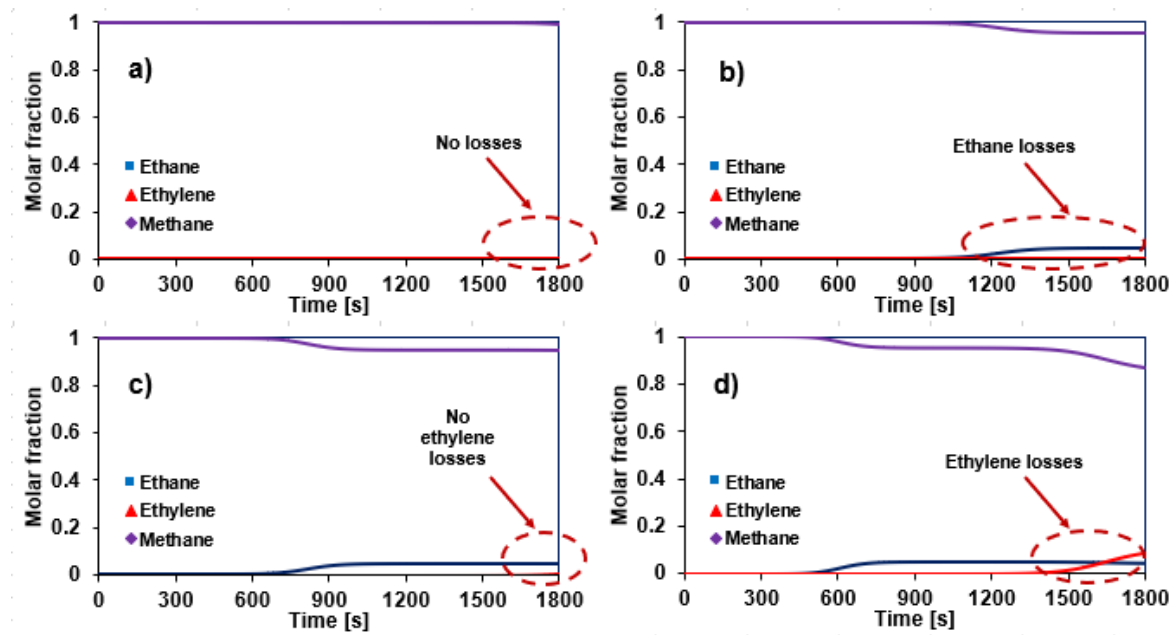


Figure 39. Different feed flows evaluated in the adsorption time proposed. a) 20 mol/s; b) 40 mol/s; c) 60 mol/s and d) 80 mol/s.

According to the results presented in Figure 39, when the flow is lower than 20 mol/s, the losses of ethane and ethylene are minimal (see figure 39 a). However, when a flow greater than 20 mol/s is used, the bed is saturated with ethane generating losses that are proportional to the feed flow increase (see figure 39: b and c). On the other hand, increasing the feed flow is convenient for the capture of ethylene due to the high selectivity of the olefin with the CaX zeolite. As long as it does not exceed the breakthrough point. A case study

was set with this feed flow rate (20 mol/s) to evaluate the study variables involve in the bed regeneration.

For this analysis, some design heuristics reported by Jain were followed [66]. The first rule states that for a two-bed PSA process, the adsorption and regeneration time must be the same. The second indicates that the maximum ratio of the pressurization time to the adsorption time should be 0.2. In addition, Levan [22] recommends that the pressurization time and depressurization time are the same. According to the above, the conditions evaluated are summarized in Table 26.

Table 26. Evaluation of the adsorption time in the bed regeneration process.

Run	$t_{\text{press}} = t_{\text{depress}}$ [s]	t_{purge} [s]	Q_{purge} [mol/s]
S1	60	1740	3
S1A	180	1620	3
S1B	360	1440	3

The results obtained based on the conditions presented in Table 26 are shown in Figure 40. There, the recovery percentage and the purity of ethane and ethylene were determined in order to evaluate the performance with respect to the pressurization time.

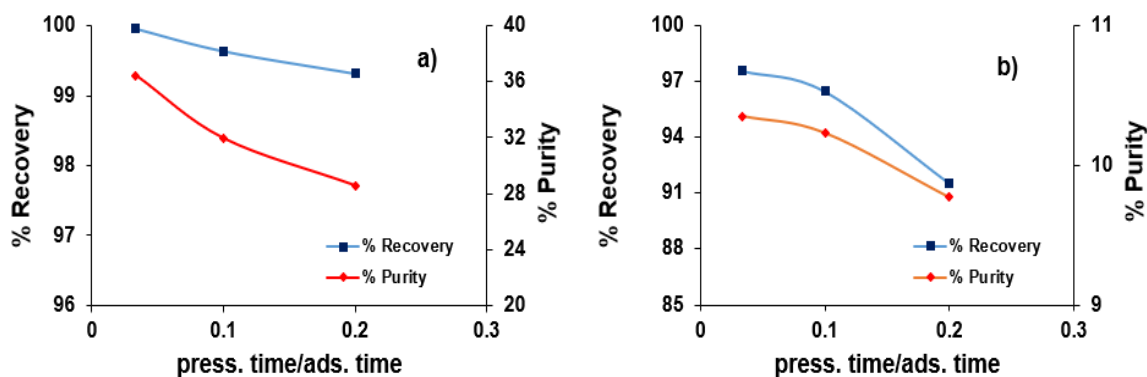


Figure 40. Olefins recovery and purity with respect to ratio of pressurization time to adsorption time. a) ethylene; b) ethane.

At a low ratio of pressurization time to adsorption time, the recovery of ethane and ethylene increases due to the increase in purge time, since more gas can be removed from the voidage of the column. Among the values evaluated, a ratio of 0.033 presents the best performance with respect to the recovery of ethylene and ethane, which are 99.9% and 97.1%, respectively. However, the purity of both components is low because the gases released in the regeneration are accompanied by methane retained in the voidage of the column and with the nitrogen used as purge flow in step 4 from the PSA cycle. Similarly, the methane separation performance was determined, as shown in Figure 41.

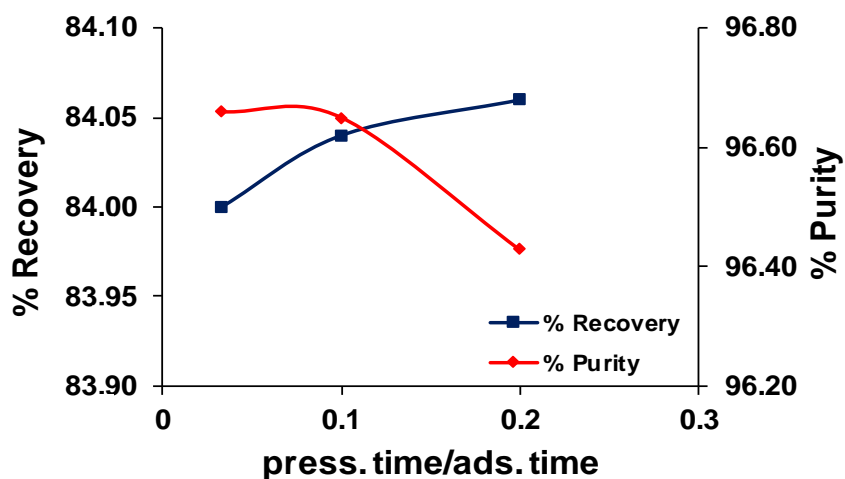


Figure 41. Methane recovery and purity with respect to the ratio of pressurization time to adsorption time.

Unlike ethane and ethylene, the recovery of methane increases with the increase of the time ratio (press. time/ads. time). Nevertheless, the purity decreases due to the increase in pressurization time that reduces the purge time; this limits the removal capacity of the ethane / ethylene mixture in the column. This implies that the non-eliminated C2 components are adsorbed in step 1 of the next PSA cycle, reducing the adsorption capacity of the bed. Consequently, the saturation of ethane in the adsorbent material is reached faster when the feed stream of step 2 flows through the bed, generating ethane losses. However, the change in methane purity does not exceed 0.25%.

To determine the effect of the purge flow on the purity of the methane obtained in step 2 of the PSA cycle, different flows were evaluated maintaining a time ratio of 0.033. The evaluated flows are presented in Table 27.

Table 27. Simulation conditions of PSA unit at different purge flows

Run	$t_{\text{press}} = t_{\text{depress}}$ [s]	Q_{feed} [mol/s]	Q_{purge} [mol/s]
S1	60	20	3
S2	60	20	1
S3	60	20	5

Based on above specifications, the performance of methane separation and ethane recovery in PSA column using different purge flows is presented in **Figure 42**.

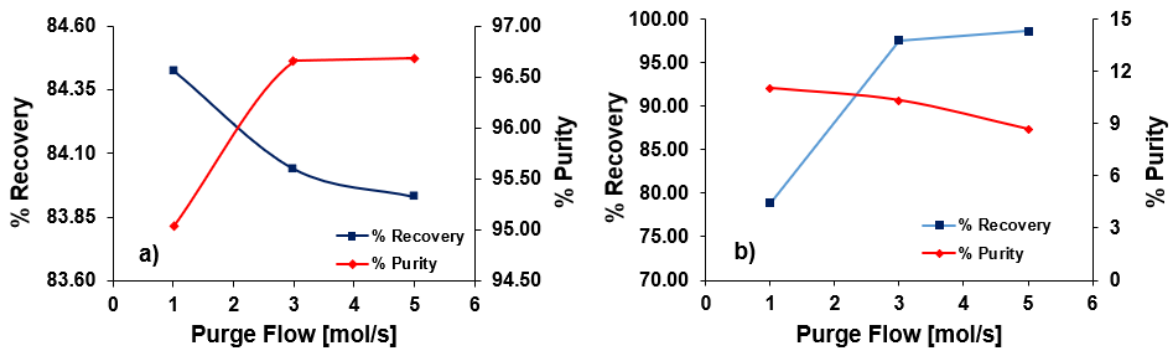


Figure 42. Performance of methane separation (a), and ethane recovery (b) in PSA column at different purge flows.

As stated before, the purge flow has an effect on the purity of methane separated in the PSA column, as shown in Figure 42. The purity of the methane obtained in step 2 of the PSA cycle decreases due to the reduction of active zeolite sites occupied by ethane and ethylene molecules that were not removed from the column in step 4 of the previous PSA cycle. This causes the amount of OCM gas fed to the bed to saturate the adsorbent material prematurely, generating losses of ethane and ethylene evacuated in the methane recovery stream. In the case of using a purge flow lower than 3 mol/s, ethane will not be completely removed from the column, affecting the purity of the methane in the next cycle. On the other hand, when using a purge flow greater than 3 mol/s, the changes in methane recovery and purity, as well as in the recovery of ethane, are not significant. However, the purity of ethane is affected by the increase of nitrogen in the recovery stream of C2 components.

Taking into account the bed has greater adsorption capacity for ethylene and that this component has greater market value, another study case was proposed. This case involves the flows of 40 and 60 mol / s, which do not reach saturation of the bed in order to avoid product losses. The conditions of the simulations proposed for these flow rates are summarized in Table 28.

Table 28. Ethylene purity and recovery for different conditions using CaX zeolite.

Run	Q_{feed} [mol/s]	Q_{purge} [mol/s]
S4	40	5
S5	40	7
S6	40	9
S7	60	5
S8	60	7
S9	60	9
S10	60	11.5
S11	60	13

The feed flows involved in the simulations presented in Table 28 were evaluated using a pressurization time of 60 seconds. In addition, different purge flows were evaluated in order

to determine the best performance in ethylene recovery and methane separation. The results obtained using a feed flow of 40 mol / s are shown in Figure 43.

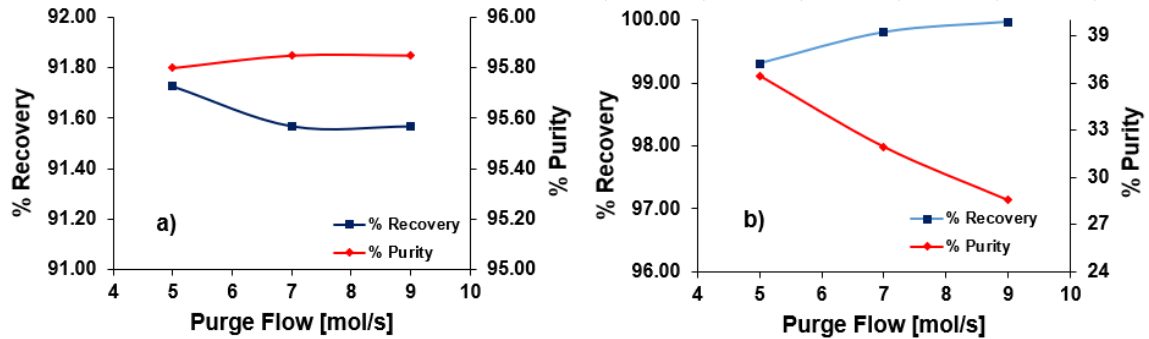


Figure 43. Evaluation of performance of PSA column using different purge flows. a) Results on methane separation performance; b) Results on ethylene separation performance.

According to the results of Figure 43, it is convenient to use a flow rate of 7 mol/s, due to the high purity of processed methane in the PSA column, and the increase in its recovery. However, operating with a purge flow greater than 7 mol/s does not enhance purity nor recovery of methane. In contrast, ethylene purity is affected by the high nitrogen content in the ethylene recovery stream. In this regard, at a flow of 40 mol/s, a purge flow of 7 mol/s is required.

In the same way, the separation performance was assessed using a feed flow of 60 mol/s and different purge flows, as shown in Figure 44.

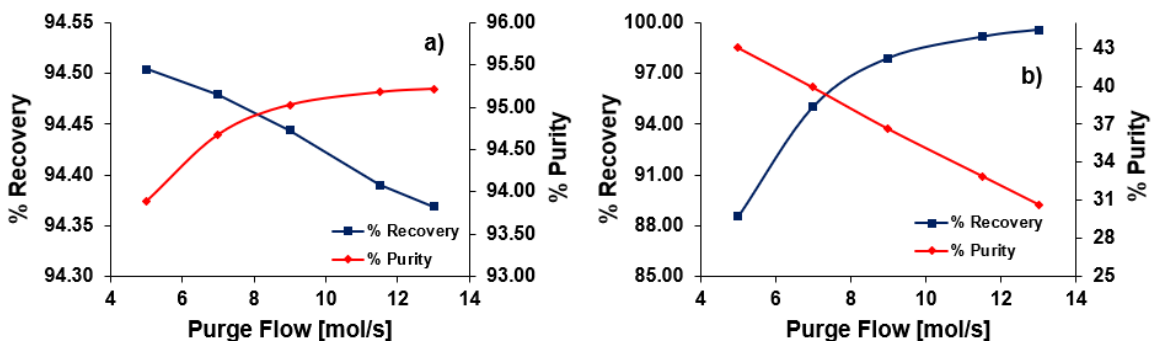


Figure 44. Separation performance of PSA column using a feed flow of 60 mol/s. a) Results on methane separation performance; b) Results on ethylene separation performance.

Based on the results presented in Figure 44, a purge flow of at least 11.5 mol/s should be used to achieve an ethylene recovery greater than 99%. However, when using a flow greater than 11.5 mol/s the purity of ethylene decreases by the amount of nitrogen used to remove the olefin adsorbed in step 2 (adsorption step). On the other hand, using a high purge flow does not represent a significant change (< 1%) in the recovery of ethylene and methane. Therefore, it is convenient to use a flow of 11.5 mol/s, which allows high recovery of ethylene and high purity of methane.

Since a feed flow of 60 mol/s into the PSA column is close to the rupture point (as presented in Figure 39), this flow was used for the methane separation operation. Therefore, 24 units of PSA are required to process the industrial scale flow proposed in chapter 3. In addition, a purge flow of 11.5 mol and a pressurization time of 60 seconds for the recovery of ethylene was employed. The operating parameters of the PSA cycle used in this separation process are summarized in Table 29.

Table 29. Operating parameter used in PSA cycle for methane separation and ethylene recovery.

Run	$t_{\text{adsorption}}$ [s]	$t_{\text{press}} = t_{\text{depress}}$ [s]	t_{Purge} [s]	Q_{feed} [mol/s]	Q_{purge} [mol/s]	P_{High}	P_{Low}
F	1800	60	1680	60	11.5	8.8	1.013

The structure of the PSA cycle and the time schedule of each step based on the above parameters are represented in Figure 45. There it is presented the amount of ethylene adsorbed by increasing the pressure, as well as the desorption of the olefin during the low-pressure stage.

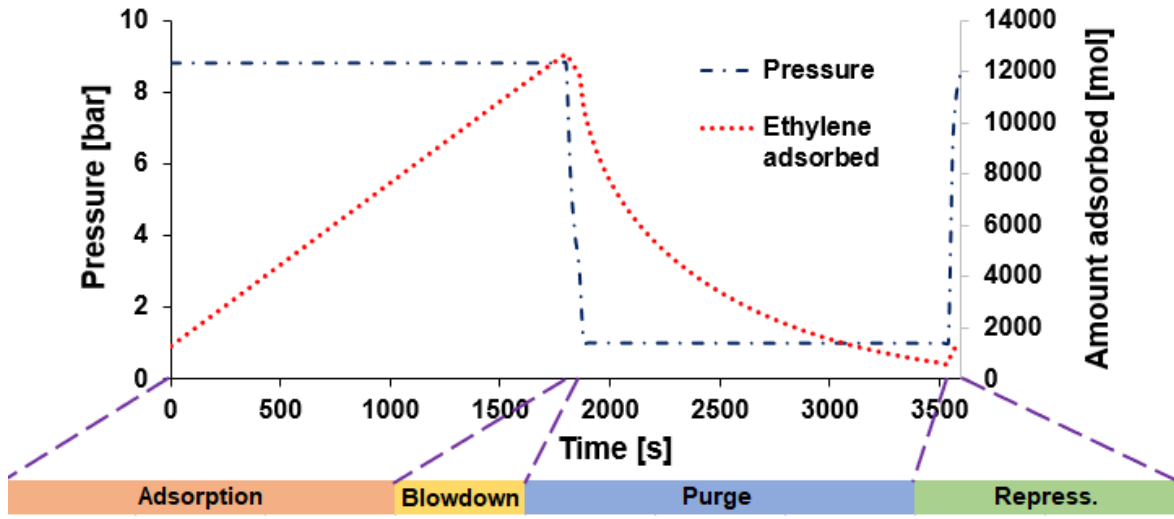


Figure 45. Structure of PSA cycle (cycle 31) and time schedule.

Additionally, Figure 46 shows the temperature profile determined during the ethane and ethylene adsorption process. The temperature profile was taken in the central section of the column at 3, 4.5 and 6 meters which were represented by nodes 20, 30 and 40, respectively.

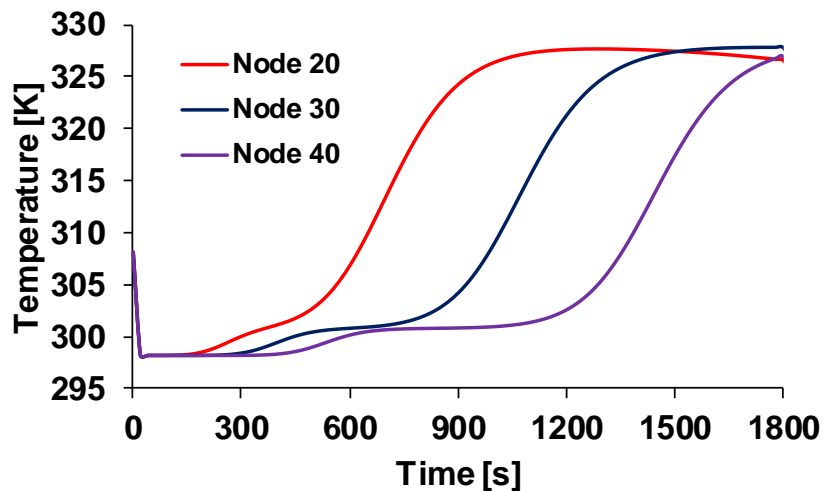


Figure 46. Temperature profile in the packed bed of CaX zeolite during PSA process

In the first seconds, a temperature lower than that of the experiment (298 K) can be observed due to the heat transfer from the bed to the surroundings, since ambient temperature is 24 ° C (297 K). Seconds later an increase in temperature occurs due to the saturation of the ethane in the bed. Subsequently, the temperature again shows an increase in temperature due to the saturation of the bed with ethylene. Therefore, Figure 46 can be used as an indicator of the time that it takes to saturate the bed at 3, 4.5 and 6 meters.

According to the operating parameters presented above, the results obtained from the simulation of the PSA column are summarized in Table 30.

Table 30. Results obtained from simulation based on operating parameters proposed.

Stream >>		CH ₄		C ₂	
Run	Component	Molar composition	% Recovery	Molar composition	% Recovery
S10	Ethane	0.0296	59.61	0.0497	40.39
	Ethylene	0.0011	0.82	0.329	99.18
	Methane	0.9518	94.39	0.1402	5.61
	Nitrogen	0.0175	8.31	0.4811	91.69

Despite methane is separated according to the results presented in the previous section, ethylene recovered in the regeneration stage presents low purity. This because there is low C2 olefin/paraffin selectivity of the CaX zeolite and the use of nitrogen in the purge flow. In that sense, the product does not comply with the quality specifications required for the production of polymers (99.9% Purity). Therefore, it is necessary to employ cryogenic distillation columns to achieve the required purity of ethylene for polymer applications.

4.1.3 Purification of ethylene

As stated before, the market purity requirements were not reached, therefore, it is necessary to use cryogenic distillation columns for further purification. Cryogenic distillation is a low temperature and high-pressure process used to separate chemicals with low boiling points.

For this study, the cryogenic distillation columns were implemented in Aspen Plus® 10.0v using Peng Robinson (PR EoS) as thermodynamic model. The model was validated with the experimental measurements done by Volova [67], as observed in Figure 47.

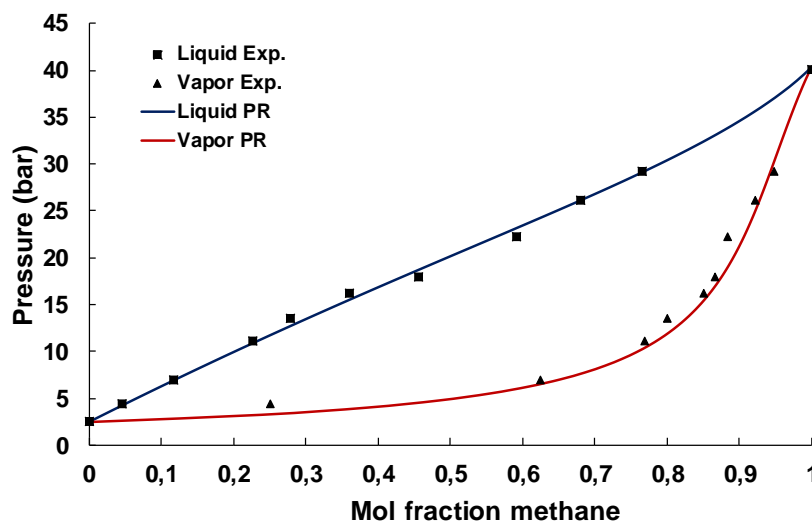


Figure 47. Liquid-vapor equilibria of Methane-Ethylene system at 186.14 K

The development of the simulations for ethylene separation and purification was based on the following procedure:

- I. Establish the separation sequence by the minimum energy required of reboiler heating and condenser cooling.
- II. Given the feed conditions and column specifications (pressure and number of stages), the reflux ratio and feed stage can be determined by shortcut models (e.g. DSTWU model) in Aspen Plus®.
- III. Execute rigorous calculations using RADFRAC model for the conditions obtained in the step II.
- IV. Determine the reboiler heat duty from the results obtained in the rigorous simulation.

In the step I, the separation sequence to ethylene purification was determined through the minimum energy requirements of the possible alternative of separation (see **Figure 48**).

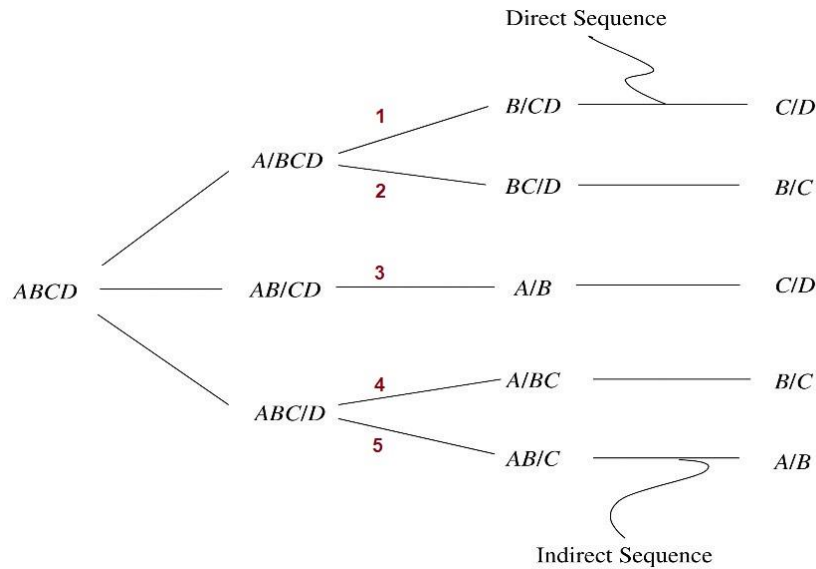


Figure 48. Alternative sequences for the separation of four components [68]

In **Figure 48**, the lightest component is separated in the top of each column in the direct sequence. In the indirect sequence, the heaviest component is separated in the bottom of each column of the train. In order to identify the lightest and heaviest components, the OCM gases were classified with the nomenclature used in **Figure 48**, according to the normal boiling point of each gas, as is presented in Table 31.

Table 31. Boiling temperatures of OCM gases.

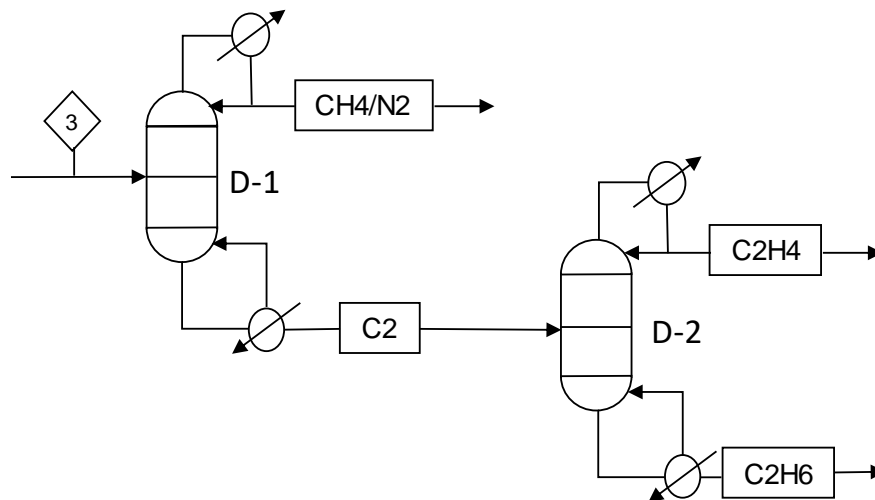
Component	Normal boiling point [K]
A: Nitrogen	77.35
B: Methane	111.55
C: Ethylene	169.3
D: Ethane	184.55

The results obtained in Aspen Plus® of the possible sequences to purify ethylene are summarized in Table 32.

Table 32. Heat duty of reboiler heating and condenser cooling

Sequence	Reboiler heating required [kW]	Condenser cooling required [kW]
1	19044.404	7653.858
2	12338.27	9940.11
3	9740.97	7448.98
4	19924.41	17529.044
5	19422.24	17136.2

According to the above results, it was established that the separation sequence with the lowest energy consumption and the lowest cooling utility requirement is number 3 (see Figure 49). This sequence separates nitrogen/methane mixture (A/B) from ethylene/ethane mixture (C/D) in the first distillation column, where subsequently the ethylene (C) is separated in a de-ethanizer column.

**Figure 49.** Representation of sequence 3 for ethylene separation

Once the ethylene separation sequence is established, in step II the simulation structure is constructed using the short method (DSTWU model) based on the following parameters:

Table 33. Operating parameters for Shortcut model

Specification	Value
Feed conditions	
Methane Flow [kmol/hr]	258.913
Ethane Flow [kmol/hr]	91.688
Ethylene Flow [kmol/hr]	607.345
Nitrogen Flow [kmol/hr]	888.213
Feed Temperature [°C]	-50
Feed Pressure [bar]	10
Column parameters	
Column 1 (C-1)	
Condenser pressure [bar]	9.9
Reboiler pressure [bar]	10
Number of stages	36
Column 2 (C-2)	
Condenser pressure [bar]	9.9
Reboiler pressure [bar]	10
Number of stages	74

The operating parameters of pressure (10bar) and temperature (-50°C) were set based on an analysis of sensibility in Aspen plus. This analysis contemplated the size, and the compressor's energy and heat requirements, as well as the wall thickness of the distillation column and the heat duty of condenser and reboiler.

The results obtained from this analysis indicate that operating at the conditions of the traditional process (pressures between 33 and 35 bar [3]) is more expensive than the conditions proposed in Table 33. This is because by increasing the pressure of the gas coming from the PSA column from 1.01 bar to 35 bar represents an increase in the capital cost of the compressor (+ 11.32%) and the distillation column (+ 9.17%) due to the increase in the number of compression stages and the thickness of the column, respectively. In addition, the utility costs of the compressor increase in its energy requirement (+ 65.6%) and cooling (+ 68.12%) due to the multistage increase in gas pressure. However, the cooling costs of the distillation column are reduced (-31.13%) by the decrease in the boiling point of OCM gases at high pressure (35 bar), but this cost reduction is not large enough in comparison with the increases in costs associated with the compressor and the column.

The values of capital and utility costs will be discussed later in order to compare and contextualize the percentage indicators stated before. On the other hand, the temperature was selected according to the lower energetic consumption in the reboiler of the distillation column, where at $-50\text{ }^{\circ}\text{C}$ it is a point close to the separation of boiling points between the methane / nitrogen and ethane mixtures / ethylene at 10 bar, which it reduces the amount of vapor to heat.

The DSTWU model is a method that uses the Winn-Underwood-Gilliland method to obtain approximate values of variables such as reflux ratio, optimum feed plate, and heats loads in the reboiler and condenser for the basic design of the distillation columns. Then, the results of the short-cut simulation (see Table 34) were used as initial parameters in a simulation with a rigorous calculation method (RADFRAC model). The RADFRAC model offers sufficient complexity and rigor in the calculations for the design of the separation train. According to the purity requirements of ethylene (99.9%), the operating parameters used to reach the product specifications are presented in Table 35.

Table 34. Results obtained from shortcut simulations in Aspen Plus

Specification	Column D-1	Column D-2
Feed stage	17	40
Reflux ratio	0.87	2.12
Minimum reflux ratio	0.81	1.77
Minimum number of stages	9	38

Table 35. Operating parameter used in RADFRAC model.

Specification	Demethanizer column 1	Deethanizer column 2
No. Stages	36	74
Condenser	Total	Total
Reboiler	Kettle	Kettle
Pressure [bar]	10	10
Reflux ratio	2.25	2.22
Distillate rate [kmol/hr]	1147.16	607.26
Reboiler duty		

Specification	Demethanizer column 1	Deethanizer column 2
Feed stage	17	40
Feed flow [mol/s]	1846.16	699
Feed composition		
Ethylene	0.329	0.869
Ethane	0.050	0.131
Methane	0.140	0
Nitrogen	0.481	0

The results obtained from the simulations using the RADFRAC model based on the operational parameters presented above are summarized in Table 36. The flow rate and molar composition obtained from the deethanizer are presented in this table.

Table 36. Results obtained from rigorous model for deethanizer column

	Top product	Bottom product
Flow rate [kmol/hr]	607.26	91.74
% Ethylene composition	99.92	0.57
% Ethane composition	0.08	99.43
% Methane composition	0	0
% Nitrogen composition	0	0

Finally, the ethylene separation and purification process using 24 units of PSA and 2 columns of cryogenic distillation are shown in Figure 50, where a diagram of the general process is presented. The mass balance of the process presented in Figure 50 is summarized in Table 37. There, the mass flows are reported, as well as the pressure and temperature of each stream.

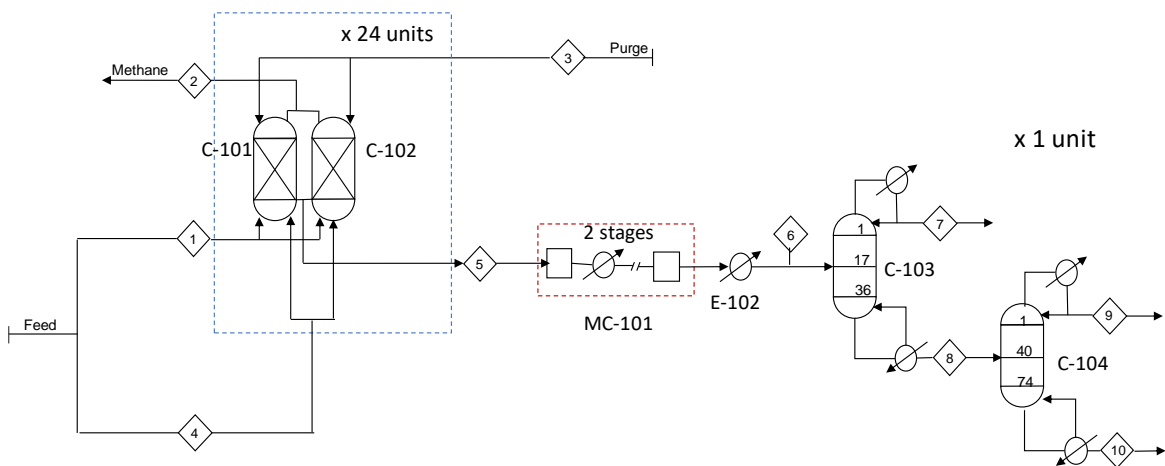


Figure 50. General flow diagram for the downstream section

Table 37. Mass balance for separation process proposed

STREAM NUMBER	1	2	3	4	5	6	7	8	9	10
Ethane [KG/HR]	6438	4070	0	389	2757	2757	0	2757	14	2743
Ethylene [KG/HR]	16201	141	0	979	17038	17038	1	17037	17023	14
Methane [KG/HR]	69702	69908	149	4211	4154	4154	4154	0	0	0
Nitrogen [KG/HR]	1336	2254	25718	81	24881	24881	24881	0	0	0
Total mass flow [KG/HR]	93677	76373	25867	5659	48831	48831	29036	19794	17037	2757
Temperature [°C]	35	35	35	35	35	35	-50	-166	-52	-32
Pressure [bar]	8.8	8.8	1.0	8.8	1.0	10	10	10	10	10

The methane from the 2 and 7 streams can be separated using a PSA system in order to be recovered and recirculated to OCM. In addition, the nitrogen separated can be purified to use again as purge (stream 3). This can be an alternative to reduce the purchase cost of nitrogen used as purge. Within the alternatives to Nitrogen separation are the PSA and Membrane separation [69], [70].

On the other hand, the recovery percentage of ethylene fed in streams 1 and 4 was 99.09%. The main ethylene losses were presented in the PSA column, where 142 kg/hr was lost during the operation. On the other hand, the losses registered in the cryogenic distillation system were 15 kg/hr.

Additionally, the energy and refrigerant requirements for the proposed scheme are reported in Table 38. Here, it is presented the energy consumption of compressor and columns, as well as the heat necessary to cooling the gas in the compression, and in the condenser of the distillation column.

Table 38. Energy and heat requirements for the PSA + Cryogenic distillation scheme

STREAM NUMBER	Electricity [kW]	Cooling water [kW]	Refrigerant [kW]
Compressor (MC-101)	4700.56	4883.16	
Heat Exchanger (E-102)			1478.4
Distillation Column (C-103)	672		5654
Distillation Column (C-104)	5949.37		5940.57

4.2 Comparison with conventional process separation

The separation scheme proposed above was compared with the traditional separation process, in order to have a reference point to assess the performance of the PSA system. This process consists on the implementation of cryogenic distillation columns to separate the mixture under the operating conditions reported at the industrial scale [3].

4.2.1 Separation of ethylene using demethanizer and deethanizer columns

In ethylene plants, the cryogenic distillation columns are highly energy intensive, generating large operating costs. However, this separation method is the most commonly used for the separation and purification of ethylene in the chemical industry. The traditional cryogenic distillation system was implemented in Aspen Plus® under the methodology used in section 4.1.3. It was established that the separation sequence that requires the least amount of energy in the reboiler and in the condenser is presented in Figure 51. This train separates nitrogen and methane in a first column, and subsequently ethylene is separated from ethane in the second column.

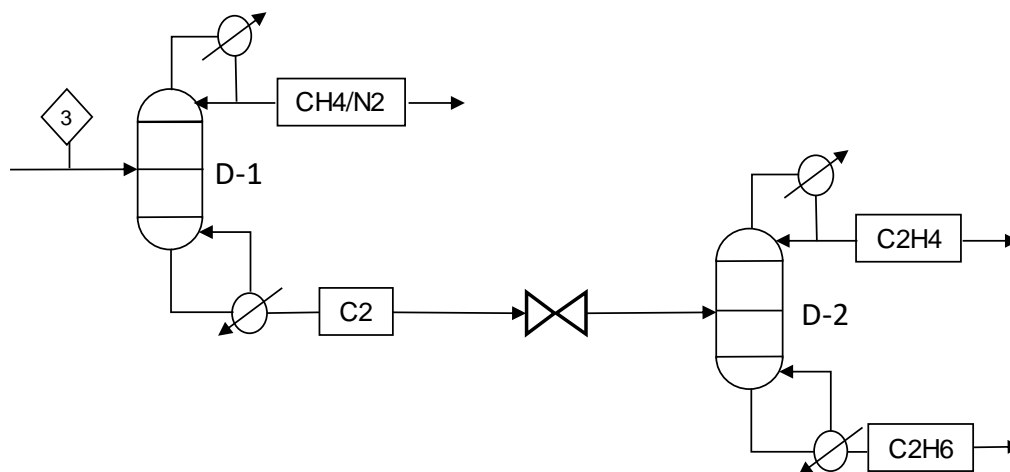


Figure 51. Sequence of separation established for traditional separation of ethylene.

To define the separation sequence, the shortcut simulation is used to determine the initial parameters necessary for the calculation of a rigorous design. The operating conditions used for this simulation are summarized in Table 39.

Table 39. Operating parameters used in shortcut model for traditional separation scheme

Specification	Value
Feed conditions	
Feed flow Flow [kmol/hr]	5166.38
Methane composition	0.8381
Ethane composition	0.0413
Ethylene composition	0.1114
Nitrogen composition	0.0092
Feed Temperature [°C]	-50
Feed Pressure [bar]	35
Column parameters	
Column 1 (D-1)	
Condenser pressure [bar]	34.5
Reboiler pressure [bar]	35
Number of stages	36
Column 2 (D-2)	
Condenser pressure [bar]	9.9
Reboiler pressure [bar]	10
Number of stages	74

The results obtained from the shortcut simulation are summarized in Table 40. There, the minimum reflux ratio and the minimum number of stages are reported. These are limit values in the exploration of variables to reduce the energy consumption using the rigorous method (RADFRAC model) under the required purity specifications (ethylene >99.9%).

Table 40. Initial parameters for distillation design in RADFRAC model

Specification	Column D-1	Column D-2
Feed stage	17	41
Reflux ratio	1.20	2.62
Minimum reflux ratio	0.91	2.23
Minimum number of stages	19	38

The design of the cryogenic distillation columns was defined according to the operating parameters presented in Table 41.

Table 41. Operating parameter used to simulation of ethylene separation

Specification	Demethanizer column 1	Deethanizer column 2
No. Stages	36	74
Condenser	Total	Total
Reboiler	Kettle	Kettle
Pressure [bar]	35	10
Reflux ratio	1.66	2.67
Distillate rate [kmol/hr]	4377.47	575.139
Feed stage	18	40
Feed flow [kmol/hr]	5166.38	788.91
Feed composition		
Ethylene	0.1114	0.7294
Ethane	0.0413	0.2705
Nitrogen	0.0092	0
Methane	0.8381	0.0001

The results obtained using the RADFRAC model are summarized in Table 42, where it is reported the amount and composition of ethylene produced by the deethanizer unit.

Table 42. Results obtained from rigorous simulation for deethanizer column

	Top product	Bottom product
Flow rate [mol/s]	575.139	213.771
% Ethylene composition	99.92	0.35
% Ethane composition	0.06	99.65
% Methane composition	0.02	0
% Nitrogen composition	0	0

In order to provide more information about the traditional ethylene separation process, the mass balance of the downstream section according to the process diagram shown in **Figure 52**, is presented in **Table 43**.

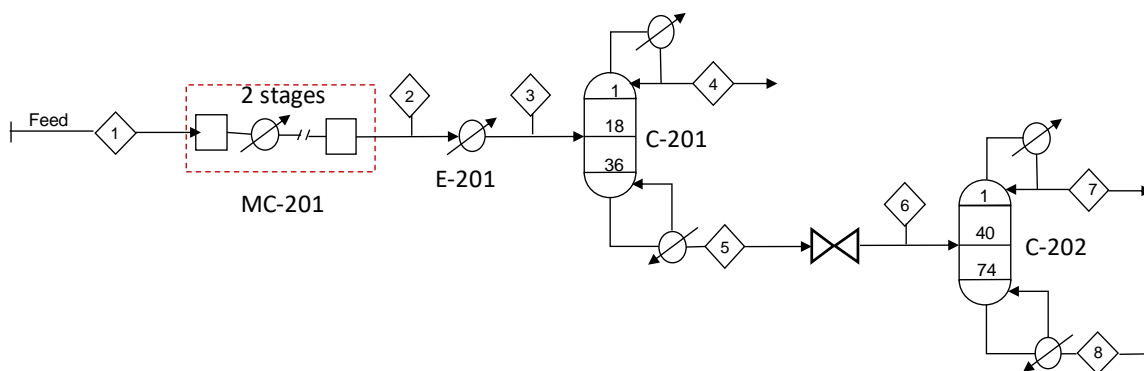


Figure 52. Process diagram of traditional cryogenic distillation for ethylene separation

Table 43. Mass balance for traditional separation scheme

STREAM NUMBER	1	2	3	4	5	6	7	8
Ethane [kg/hr]	6416	6416	6416	0	6416	6416	10	6406
Ethylene [kg/hr]	16146	16146	16146	2	16144	16144	16123	21
Methane [kg/hr]	69464	69464	69464	69463	1	1	1	0
Nitrogen [kg/hr]	1332	1332	1332	1332	0	0	0	0
Total mass flow [kg/hr]	93358	93358	93358	70797	22561	22561	16134	6427
Temperature [°c]	45	35	-50	-93	-2	-47	-52	-32
Pressure [bar]	8.8	35.0	35.0	35	35.0	10	10	10

The energy and heat requirements for this scheme are summarized in Table 44.

Table 44. Energy and heat requirements for the traditional Cryogenic Distillation scheme

STREAM NUMBER	Electricity [kW]	Cooling water [kW]	Refrigerant [kW]
Compressor (MC-201)	7426.5	9070	
Heat Exchanger (E-102)			5028
Distillation Column (C-103)	3212		11277
Distillation Column (C-104)	5425.3		6413

According to the mass balance, the percentage of ethylene recovery obtained by the traditional separation process was 99.86%, which means that the ethylene losses are 23 kg/hr during the operation. In addition, the ethylene purity for polymer applications was achieved. In comparison with the hybrid scheme (PSA + CD), this scheme (traditional separation) presents approximately 6.8 times less losses of ethylene.

Additionally, the energy required in the multi-compressor is 57.99% more larger than the energy used in the multi-compressor from the PSA + CD scheme. This is because the gas to be compressed in the traditional scheme contains all the methane from the carbon dioxide purification section.

4.2.2 Energy consumption

The energy consumption of the traditional process and that of the PSA process were also assessed. The energy requirement of the compressor and the reboilers of both separation schemes were considered in this analysis. In Figure 53 it is shown the performance with respect to the recovery of ethylene and the energy consumption of the proposed separation alternatives previously.

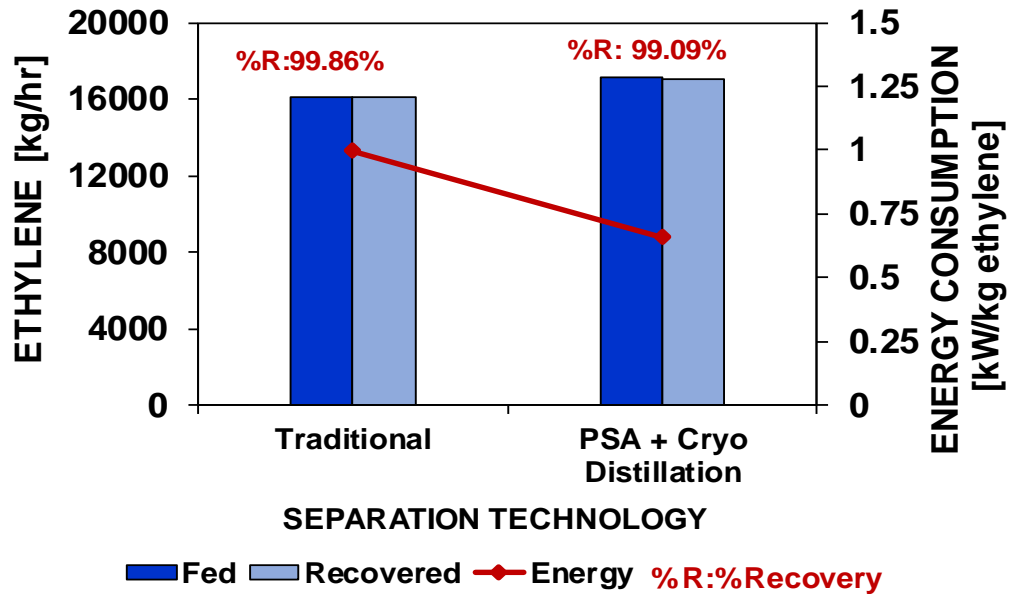


Figure 53. Performance of the separation schemes evaluated

The energy saving of the separation scheme that involves PSA units is around 30% with respect to the traditional one. This reduction occurs because the amount of gas sent to compression is lower than that used in the traditional separation process. In addition, the amount of gas fed to the first distillation column in the hybrid scheme is reduced by 47.7% respect to traditional scheme, which reduces the energy consumption contributed by the demethanizer column.

Finally, in Figure 53 is presented that the hybrid process (PSA + Cryogenic distillation) requires around 33.8% less energy to process 1 kg of ethylene, compared with the traditional. Although the energy savings of the hybrid separation process (PSA + cryogenic distillation) is evident, it is necessary to explore the feasibility of each process through a preliminary economic analysis, as presents below.

4.2.3 Preliminary economic evaluation

A preliminary economic evaluation was carried out to determine the capital and operating costs of the ethylene separation alternatives assessed. The capital cost included the cost of the equipment required for each separation scheme, and the operating one involved the costs of the required for the used utilities.

Annualized capital investment cost (CAPEX)

The cost of the equipment was estimated through the Aspen Economic Analyzer v.10. However, the cost of the PSA columns was estimated according to what was reported by Seider et. al. [64]. The method to estimate the cost of the pressurized columns is based on purchase cost for carbon steel construction, platforms, ladders and a nominal number of nozzles and manholes, as presented in the following expression:

$$C_P = F_M C_V + C_{PL} \quad (76)$$

Where, F_M is the material factor, C_V is the empty vessel and C_{PL} is the added cost for platforms and ladders. The vessel cost includes nozzles, manholes and supports based on the weight of the shell and the two heads, as given by the following correlation:

$$C_V = \exp \left[7.2756 + 0.18255 * LN(W) + 0.02297 * (LN(W))^2 \right] \quad (77)$$

The added cost (C_{PL}) depends on the column internal diameter and length, as follow

$$C_{PL} = 300.9 * (D_i)^{0.63316} (L)^{0.80161} \quad (78)$$

The weight of the vessel for the cost estimation of the pressurized columns depends on the wall thickness, and it can be calculated using the following expression in pounds.

$$W = \pi(D_i + t_w)(L + 0.8D_i)t_w\rho \quad (79)$$

Where, the term $0.8D_i$ accounts for two heads, $D_i + t_w$ is the external diameter, and ρ is the density of carbon steel (0.284 lb/in³).

Additionally, the cost of the adsorbent material required to fill each column was calculated according to the volume of the column and the density of the packing. For this study, the cost estimation was done with the commercial price of a CaX zeolite. The data necessary for estimating the packing costs of each column are reported in Table 45.

Table 45. Data for estimation cost of column packing

Zeolite	Price (\$USD/kg)*	Bulk density (kg/m ³)	Column volume (m ³)
CaX	1	700	28.27

* Taken from Alibaba [71]

The values of the costs obtained for the vessel, packing and platforms corresponding to a PSA column are presented in Table 46.

Table 46. Cost of a PSA column

Equipment	C_V [US\$]	C_{PL} [US\$]	Packing [US\$]	Total cost per column[US\$]
Column	\$ 74,690	\$ 14,937	\$ 19,792	\$ 109,420

Because 24 PSA units are required, these set is conformed by 48 adsorption columns, so the total cost of the PSA system is US \$ 5,252,150. The purchase cost is defined at a corresponding CE = 500 index for the year 2006. Therefore, it must be updated with an index of CE = 567.5, as will be presented later. The total costs obtained by Aspen Economic Analyzer are summarized in

Table 47.

Table 47. Equipment cost results obtained by Aspen Economic Analyzer

Equipment	Traditional separation	PSA + CD*
Condenser	\$ 50,700	\$ 61,000
Compressor	\$ 3,043,000	\$ 7,805,200
Distillation column C1	\$ 1,135,800	\$ 570,600
Distillation column C2	\$ 715,100	\$ 1,181,700

*CD: Cryogenic Distillation

The costs reported in Table 48 are valid for 2016, which requires updating costs through the CE index, as it is presented in Table 48.

Table 48. CE index for the years involve in this study

Year	CE index
2006	500.0

Year	CE index
2016	541.7
2018	567.3

Thus, the update of costs is given by

$$Actual\ Cost = \frac{CE\ index\ act}{CE\ index\ old} \times old\ cost \quad (80)$$

According to the above, current costs of both processes are shown in Table 49.

Table 49. Actualization cost for separation alternatives proposed

Equipment	Traditional separation	PSA + CD*
PSA units	-	\$ 5,959,089
Condenser 1	\$ 53,096	\$ 63,883
Compressor	\$ 3,186,808	\$ 8,174,063
Distillation column C1	\$ 1,189,476	\$ 597,566
Distillation column C2	\$ 748,895	\$ 1,237,546

Once, the equipment costs were updated, the installation cost must be considered. Due to the installed cost includes shipping costs, foundations, mounting and simple electric and piping connections [72]. This cost is averaged for each type of equipment and estimated through multipliers, which are reported in Table 50 [73].

Table 50. Multipliers for installed costs of process equipment from the ethylene separation

Equipment	Multiplier for installed cost
Distillation columns, Carbon Steel	3.0
Pressure vessels, Carbon Steel	2.8
Heat exchangers	2.5
Compressors	1.3

The estimate of the total cost of the equipment including the installation cost is determined by the following equation:

$$Total\ cost = Equipment\ cost \times multiplier\ factor \tag{81}$$

The total cost of the equipment involved in both separation schemes presented in this study is exhibited in Table 51.

Table 51. Total capital cost for separation schemes proposed

Equipment	Traditional separation	PSA + CD
PSA units	-	\$ 16,685,449
Condenser 1	\$ 132,740	\$ 159,707
Compressor	\$ 4,142,850	\$ 10,626,282
Distillation column C1	\$ 3,568,429	\$ 1,792,697
Distillation column C2	\$ 2,246,684	\$ 3,7712,637
Total capital cost	\$ 10,090,703	\$ 32,976,772

Operational cost (OPEX)

The operational costs were estimated according to heat duty required for the reboiler and condenser cooling capacity, as well as the utilities consumption of the compressor. The energy cost required for the compressor and reboiler of each distillation column were determined through electricity price. The cost of compressor cooling (gas compression system) was estimated based on price of water cooling, and refrigerant cost was computed according to reported by Turton et. al [74].

The cost of electricity was estimated based on reported by Ulrich and Vasudevan [75]. There, the price of the utility ($C_{S,u}$) was calculated by the following equation:

$$C_{S,u} = a(CE\ PCI) + b(C_{S,f}) \tag{82}$$

Where, a and b are utility cost coefficients and $C_{S,f}$ is the price of fuel in \$(US)/GJ. The fuel used to generate electricity was natural gas, whose price is \$3.16 /GJ. The value of utility

cost coefficients is presented in Table 52. The cost of refrigeration was calculated from the data reported in Table 53 by extrapolating the coefficient of reversible performance (COP_{REV}) as a function of temperature (see Eq. 83).

Table 52. Utility cost coefficients

Cost coefficients		
	a	b
Electricity \$/kwh		
Purchased from outside	1.3×10^{-4}	0.010

Table 53. Coefficient of reversible performance at different temperatures

Temperature [°C]	$1/COP_{REV}$
5	0.144
-20	0.257
-50	0.426

$$\frac{1}{COP_{REV}} = (0.00002 * (T)^2) - (0.0042 * T) + 0.1646 \quad (83)$$

Therefore, compared with cooling at 5°C whose price is \$ 4.77/GJ, cooling to -20°C is $0.257/0.144$ (1.78) times as expensive, and cooling to -50°C is $0.426/0.144$ (2.96) times as expensive [74]. In that regard, the predicted cost of the refrigerant required for cooling the condensers used in the ethylene separation process is summarized in Table 54.

Table 54. Refrigerant cost at different temperature

Temperature [°C]	$1/COP_{REV}$	Price [\$/GJ]
5	0.144	4.77
-20	0.257	8.49
-50	0.426	14.12
-60	0.489	16.18

Because the refrigeration systems operate at less than -60°C, the refrigeration cycle proposed by Turton [74] is no longer applicable. The cost of \$40/GJ was used to refrigerate the condenser from the distillation column employed to remove the mixture of nitrogen/methane. This value was taken from Aspen Economic Analyzer v.10. On the other hand, the cooling system used in the compressor uses cooling water, which has a price of \$0.0157/m³ [74].

The energy requirements and the volume of water required in each unit from both ethylene separation processes are summarized in Table 55. There, it is presented the heat duty required for the reboiler heating and condenser cooling, as well as the electricity and cooling water required to operate the gas compressor.

Table 55. Utilities required to operation of equipment in the ethylene separation in 1 h.

	Electricity [kw]	Cooling water [m3/s]	Refrigerant [kw]
Traditional separation			
Compressor	7426.5	0.436220577	-
Condenser 1	-	-	5028.21
Column 1	3212.24	-	11277
Column 2	5425.3	-	6413.24
CaX alternative 1			
Compressor	4700.56	0.23485637	-
Condenser 2	-	-	1478
Column 1	672	-	5654
Column 2	5948.37	-	5940.6

The costs were annualized for each equipment according to the following expressions:

For the cost of electricity and refrigerant

$$A_u = U_c \left(31.536 \times 10^6 \frac{s}{yr} \right) f_0 * C_{S,ui} \left(\frac{1 h}{3600 s} \right) \quad (84)$$

For the cost of cooling water

$$A_u = U_c \left(31.536 \times 10^6 \frac{s}{yr} \right) f_0 * C_{S,u} \quad (85)$$

Where, U_c is the utility required, f_0 is the operation factor (0.94) and $C_{S,u}$ is the cost of each utility.

Table 56. Annualized cost of utilities

	Electricity [\$/yr]	Cooling water [\$/yr]	Refrigerant [\$/yr]	Total utility cost per equipment
Traditional separation				
Compressor	\$6,831,926	\$203,021		\$7,034,947
Condenser 1			\$2,414,698	\$2,414,698
Column 1	\$2,955,065		\$13,371,743	\$16,326,808
Column 2	\$4,990,995		\$3,079,832	\$14,504,162
Total utility cost				\$33,847,230
CaX alternative 1				
Compressor	\$4,324,228	\$109,304		\$4,433,532
Condenser 2			\$709,780	\$709,780
Column 1	\$618,199		\$6,704,251	\$7,322,450
Column 2	\$5,472,137		\$2,852,841	\$8,324,978
N2 (Purge)				\$6,998,823
Total utility cost				\$27,789,563

As can be seen, Table 56 includes the price of nitrogen used in the PSA column as a purge, which has an industrial price of \$ 0.01 per lb (in 2013). This price was actualized to \$ 0.014 per lb due to inflation effects. In addition, the nitrogen market price corresponds to current one [76].

Total annualized cost (TAC)

The total cost of both processes was calculated as the sum of the operational cost with the capital cost as given in equation 88 [12].

$$TAC = OPEX + CAPEX \left(\frac{IR(IR + 1)^N}{(IR + 1)^N - 1} \right) \quad (88)$$

The IR is the interest rate of 15 %, and N is the operational life of the plant, which is assumed to be 10 years. The results obtained for the total annualized cost is presented in Table 57.

Table 57. Total annualized cost for separation schemes proposed

Separation scheme	Total annualized cost
Traditional separation	\$35,857,823
PSA + Cryogenic Distillation	\$34,360,253

Ethylene price

The price of ethylene was determined according to the global report presented by ICIS at the end of 2018 [77] (see Figure 54). This report offers the sale prices of the main ethylene markets in the world (US, Asia and EU).

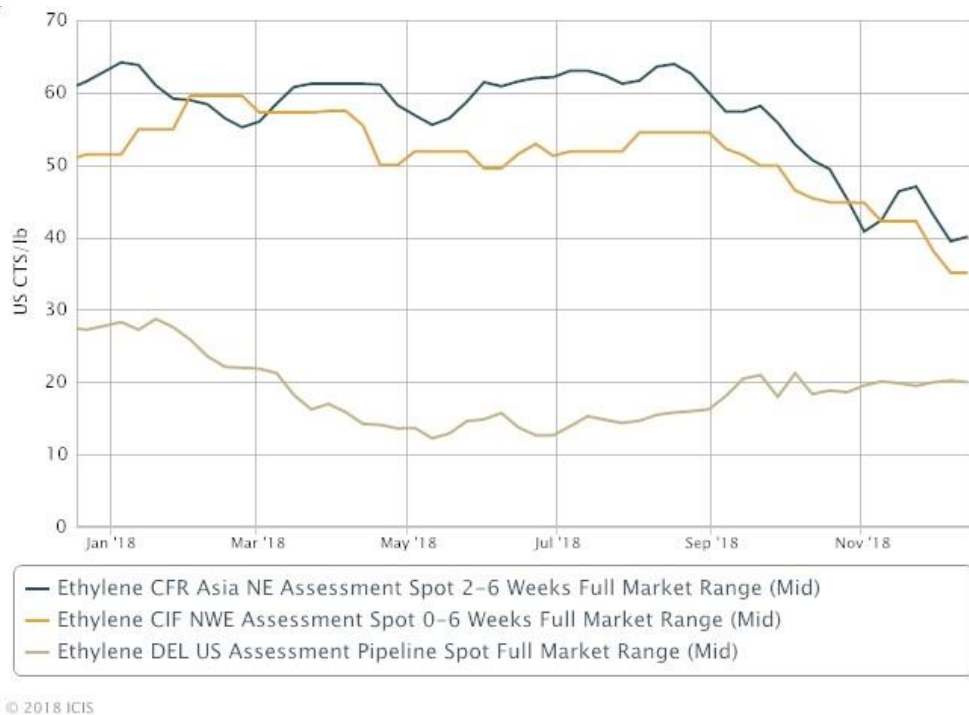


Figure 54. Global ethylene prices [77]

The prices of the ethylene produced by each separation scheme is reported in Table 58. There, the industrial price of ethylene was evaluated in the different markets in order to identify the most favorable scenarios for the sale of the product.

Table 58. Ethylene sale price in the US, EU and Asia markets

Market	US [cts/lb]	US \$/ton	Ethylene produced by traditional separation [ton/yr]*	Sale price [US\$]	Ethylene produced by PSA + CD [ton/yr]*	Sale price [US\$]
US	20	440.92		\$62,362,171		\$65,849,884
NWE	36	793.66	141,435	\$112,251,907	149,345	\$118,529,792
Asia	40	881.85		\$124,724,342		\$131,699,769

* Amount obtained from simulations proposed in this study.

Based on the above results, it is convenient to market the ethylene produced in the Asian and European markets, since the price is almost double that of the American market and the net profit margins could be higher.

In summary, the capital cost of the hybrid separation scheme is approximately 3 times higher than the traditional scheme. However, operating costs using the hybrid scheme are reduced approximately 18%. The capital cost of the hybrid system is mainly represented by the cost of PSA units and the gas compression system, which represent 51% and 32% of the total cost of capital, respectively. The cost of the PSA columns can be reduced through of a global optimization of the PSA adsorption system. This would represent a significant reduction in the cost of capital, which is advantageous not only because of the purchase cost of the columns, but also because of the reduction in plant size and all the instrumentation that each PSA unit requires. On the other hand, the utility cost associated with the purge will be reduced by implementing a separation system of PSA or membranes for the separation of nitrogen, which it can be reduced the value of the purge nitrogen involved in this analysis.

Finally, the total cost of the PSA separation process with cryogenic distillation is slightly lower (0.04%) compared to the traditional separation scheme. This is because the investment cost of the hybrid process is higher. However, the separation process involving the PSA system produces 7910 tons per year more than the traditional process, which generates higher profits (Ethylene sold - TAC), as shown in Figure 55.

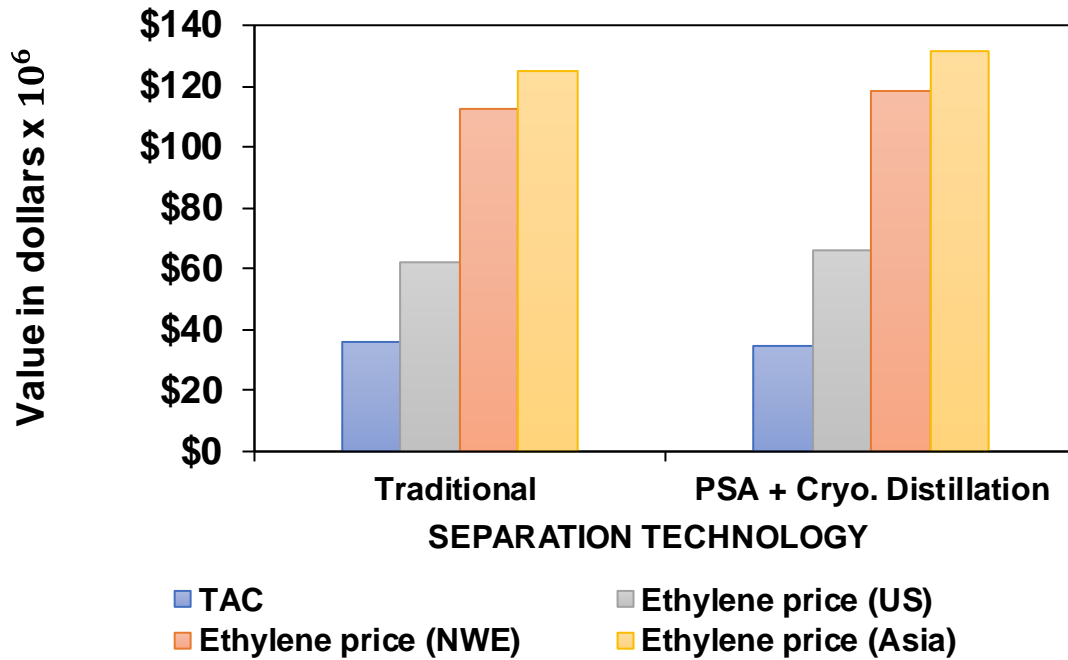


Figure 55. Comparison of the total annualized cost and the sale price of ethylene in the different markets for the evaluated processes. US: United Stated; NEW: North west of Europe; and Asia.

The difference in the profits obtained in each process due to the sale of ethylene in the different markets is \$ 4,985,284, which indicates that it is an advantage to implement the PSA system in the separation of ethylene from the OCM process.

5. Conclusions and perspectives

5.1 Conclusions

A mathematical model was developed based on the mass, energy and momentum balances, the Langmuir isotherm to represent the adsorption equilibrium and linear driving force to represent the kinetics of adsorption.

The proposed mathematical model was validated with the experimental data reported by Fatemi et. al., and the dynamic experiments obtained as a result of the Bio-empowered Oxidative Coupling of Methane (OCM) process BIOCM project. Here it was found that the fitted parameters of the model indicate that the adsorption process is competitive. The breakthrough curves were showed nitrogen and methane were not adsorb on the CaX zeolite. However, the absorbent material exhibited selectivity for ethane and ethylene.

The driving linear force model was based on 3 resistances (external, macropores and micro pores), which were determined from the mass transfer parameter adjusted in the validation of the model, and the estimation of the film and effective diffusion coefficients of the molecules. Here it was found the film resistance (external resistance) was negligible for all components. Nevertheless, the resistance of macropores and micropores were present. The resistance of micropores was more predominant in the ethylene adsorption because the most of active sites were in the micropores, which were occupied mostly by this ethylene molecules.

The operating conditions of the PSA columns were established through the simulation process implemented by Aspen adsorption. Here, methane separation and ethylene recovery strategies were determined by means of a PSA cycle conformed of 4 steps (repressurization, adsorption, depressurization and purge). Nitrogen was used as a purge, since the adsorption of this gas is negligible and allows the entrainment of the ethylene absorbed in the PSA column.

Due to the CaX zeolite exhibits selectivity for ethane, the ethylene purification process must be performed by cryogenic distillation. Despite this, the incorporation of PSA columns in the downstream section presents an energy saving of 30%, attributed mainly to the gas compression. The latter is because the amount of gas to be compressed in the hybrid process (PSA + CD) is less than the traditional process. In addition, the pressure increase using a PSA system is approximately 2.5 times less than the traditional Cryogenic Distillation scheme.

The implementation of a PSA system presents an 18% savings in operating costs due to the fact that a large part of the methane coming from the CO₂ purification section is removed by the PSA columns, reducing the energy cost in the compression of gases and the amount of refrigerant to condense this gas.

5.2 Perspectives

This study creates the need for continuous improvement in the process of separation of effluent gases from OCM. Therefore, the following is recommended:

It is necessary to experimentally measure the ethylene breakthrough curves at different temperatures and pressures in order to explore other alternatives in bed regeneration.

It is desirable to implement the mathematical model in open source software to couple the PSA process to the general OCM process.

It is recommended to perform a global optimization of the PSA system in order to increase bed productivity and reduce capital costs in the implementation of this system to the downstream section.

A. Annex A

Apply mechanical energy balance for a differential volume, where the flow pass through the bed:

$$\frac{\Delta P}{\rho_g} + \Delta \frac{u_0^2}{2} + g\Delta Z + \mathfrak{S} + w_s = 0 \quad (A.1)$$

If the cross-sectional area of the bed (A) is constant and there is no shaft work between the inlet bed and outlet bed, the mechanical energy balance can be reduced to:

$$\rho_g g h_0 + \rho_g \mathfrak{S} = -\Delta P \quad (A.2)$$

For a packed bed, the frictional losses is given by

$$\mathfrak{S} = 3 f_F \frac{1 - \varepsilon}{\varepsilon^3} u_0^2 \frac{L}{D_p} \quad (A.3)$$

Where, the friction factor (f_F) is expressed as follow

$$f_F = \frac{1}{3} \left[\frac{150}{Re} + 1.75 \right] \quad (A.4)$$

Here, $\frac{150}{Re}$ represent the laminar region and 1.75 the turbulent region.

Substituting the above expressions

$$(P_1 - P_2) = \left[\frac{150 (1 - \varepsilon) u_f}{\rho_g u_0 D_p} + 1.75 \right] \rho_g u_0^2 \frac{L}{D_p} \frac{1 - \varepsilon}{\varepsilon^3} + \rho_g g h_0 \quad (A.5)$$

To derive an equation for the minimum fluidization velocity, it is assumed that the fluidization of the packed bed begins when the pressure drop across the bed is equal the weight of the bed per unit of area

$$\frac{\text{weight of the bed}}{\text{area}} = (1 - \varepsilon)\rho_s h_0 g + \varepsilon \rho_g h_0 g \quad (\text{A.6})$$

Where, $(1 - \varepsilon)\rho_s h_0 g$ is the weight of particles and $\varepsilon \rho_g h_0 g$ is the weight of fluid between particles.

Equating

$$\left[\frac{150 (1 - \varepsilon) u_f}{\rho_g u_0 D_p} + 1.75 \right] \rho_g u_0^2 \frac{L}{D_p} \frac{1 - \varepsilon}{\varepsilon^3} + \rho_g g h_0 = (1 - \varepsilon)\rho_s h_0 g + \varepsilon \rho_g h_0 g \quad (\text{A.7})$$

Where, the above expression is rearranging

$$\left(1.75 \frac{\rho_f}{D_p \varepsilon_i^3} \right) u^2 + \left(150 \frac{(1 - \varepsilon_i) \mu_f}{D_p^2 \varepsilon_i} \right) u + (-g(\rho_s - \rho_f)) = 0 \quad (\text{A.8})$$

References

- [1] P. Reeder, "Analysis: Naphtha's challenge in the age of petrochemical feedstock boom," *S&P Global*, 2018. [Online]. Available: <https://www.spglobal.com/platts/en/market-insights/latest-news/petrochemicals/031518-analysis-naphthas-challenge-in-the-age-of-petrochemical-feedstock-boom>. [Accessed: 22-Sep-2018].
- [2] J. S. Plotkin, "Beyond the Ethylene Steam Cracker - American Chemical Society." [Online]. Available: <https://www.acs.org/content/acs/en/pressroom/cutting-edge-chemistry/beyond-the-ethylene-steam-cracker.html>. [Accessed: 28-Feb-2019].
- [3] D. Salerno Paredes, "Optimal Synthesis of Downstream Processes using the Oxidative Coupling of Methane Reaction," Technische Universitat Berlin, 2013.
- [4] Repsol, "Ethylene," *chemical*, 2018. [Online]. Available: <https://www.repsol.com/en/products-and-services/chemicals/product-range/ethylene/index.cshtml>.
- [5] H.-R. Godini *et al.*, "Concurrent Reactor Engineering , Separation Enhancement and Process Intensification; Comprehensive Unicat Approach for Oxidative Coupling of Methane (OCM)," *Tech. Trans.*, vol. 109, pp. 63–74, 2012.
- [6] none, "Materials for Separation Technologies. Energy and Emission Reduction Opportunities," May 2005.
- [7] I. Amghizar, L. A. Vandewalle, K. M. Van Geem, and G. B. Marin, "New Trends in Olefin Production," *Engineering*, 2017.
- [8] Marshall Frank, "US Ethylene Plant Development; Announcement, Plans,

- and New Technology.” [Online]. Available: <https://blog.ihrdc.com/marshall-frank/recent-developments-in-ethylene/>. [Accessed: 27-Jan-2019].
- [9] D. Salerno, H. Arellano-Garcia, and G. Wozny, “Ethylene separation by feed-splitting from light gases,” *Energy*, vol. 36, no. 7, pp. 4518–4523, 2011.
- [10] G. E. Keller and M. M. Bhasin, “Synthesis of ethylene via oxidative coupling of methane. I. Determination of active catalysts,” *Journal of Catalysis*, vol. 73, no. 1, pp. 9–19, 1982.
- [11] Z. Stansch, L. Mleczko, and M. Baerns, “Comprehensive Kinetics of Oxidative Coupling of Methane over the $\text{La}_2\text{O}_3/\text{CaO}$ Catalyst,” *Ind. Eng. Chem. Res.*, vol. 36, no. 7, pp. 2568–2579, 1997.
- [12] A. Penteado, E. Esche, D. Salerno, H. R. Godini, and G. Wozny, “Design and Assessment of a Membrane and Absorption Based Carbon Dioxide Removal Process for Oxidative Coupling of Methane,” *Ind. Eng. Chem. Res.*, vol. 55, no. 27, pp. 7473–7483, 2016.
- [13] “BP Statistical Review of World Energy 2015,” 2015.
- [14] R. W. Triebe, F. H. Tezel, and K. C. Khulbe, “Adsorption of methane, ethane and ethylene on molecular sieve zeolites,” vol. 10, no. 1, pp. 81–84, 1996.
- [15] L. Garcia, “Síntesis, Aglomeración y Caracterización de un Tamiz Molecular a partir de Zeolita 5A a Escala Piloto para la Separación de los Gases Provenientes del Proceso de Acoplamiento Oxidativo de Metano (OCM),” Universidad Nacional de Colombia, 2017.
- [16] M. Salmasi, M. Doroudian Rad, S. Fatemi, and S. Hosseinpour, “An Experimental Design Study for CH_4 , C_2H_6 and C_2H_4 Adsorption and $\text{C}_2\text{s}/\text{CH}_4$ Selectivity on 10X Zeolite,” *J. Chem. Pet. Eng.*, vol. 45, no. 1, pp. 71–82, 2011.
- [17] J. Jee, M. Kim, and C. Lee, “Adsorption Characteristics of Hydrogen Mixtures in a Layered Bed: Binary, Ternary, and Five-Component Mixtures,” *Ind. Eng. Chem. Res.*, vol. 40, pp. 868–878, 2001.
- [18] D. M. Ruthven and S. Farooq, “Air separation by pressure swing adsorption,” *Gas Sep. Purif.*, 1990.

- [19] P. da Silva Barcia, "Separation of Light Naphtha for the Octane Upgrading of Gasoline: Adsorption and Membrane Technologies and New Adsorbents," University of Porto, 2010.
- [20] J. D. Seader, E. J. Henley, and D. K. Roper, *Separation Process Principles: Chemical and Biochemical Operations*, 3rd ed. John Wiley & Sons, Inc., 2011.
- [21] S. Brunauer, L. S. Deming, W. E. Deming, and E. Teller, "On a Theory of the van der Waals Adsorption of Gases," *J. Am. Chem. Soc.*, 1940.
- [22] M. D. LeVan, G. Carta, and C. M. Yon, *Section 16: Adsorption and Ion Exchange*. 2007.
- [23] D. D. Do, *Adsorption Analysis: Equilibria and Kinetics*. Imperial College Press, 1998.
- [24] H. G. Karge and J. Weitkamp, *Adsorption and Diffusion*. Springer-Verlag Berlin Heidelberg, 2008.
- [25] F. Keil, *Diffusion und Chemische Reaktionen in der Gas/Feststoff-Katalyse*. Springer-Verlag Berlin Heidelberg, 1999.
- [26] E. Glueckauf, "Theory of chromatography: Part 10. - Formula for diffusion into spheres and their application to chromatography," *Trans. Faraday Soc.*, 1955.
- [27] H.-J. Bart, "Adsorption," in *Ullmann's Encyclopedia of Industrial Chemistry*,. Kaiserslautern: Wiley-VCH, 2012, p. 72.
- [28] AspenTech, "Aspen Adsim™ 12.1 Adsorption Reference Guide." AspenTech, p. 324, 2003.
- [29] S. M. Auerbach, K. A. Carrado, and P. K. Dutta, *Handbook of Zeolite Science and Technology*. New York: Marcel Dekker, Inc., 2003.
- [30] A. R. Garcıa-Soto, G. Rodrıguez-Nino, and C. A. Trujillo, "Zeolite LTA synthesis: Optimising synthesis conditions by using the modified sequential simplex method," *Ing. e Investig.*, vol. 33, no. 3, pp. 22–27, 2013.
- [31] S. M. Auerbach, K. A. Carrado, and P. K. Dutta, *Handbook of Zeolite Science and Technology*. CRC Press, 2013.

- [32] W. Lutz, "Zeolite Y: Synthesis, Modification, and Properties—A Case Revisited," *Adv. Mater. Sci. Eng.*, vol. 2014, pp. 1–20, 2014.
- [33] A. Julbe and M. Drobek, "Zeolite X: Type," in *Encyclopedia of Membranes*, Berlin, Heidelberg: Springer Berlin Heidelberg, 2014, pp. 1–2.
- [34] S. Kulprathipanja, *Zeolites in Industrial Separation and Catalysis*. Wiley-VCH, 2010.
- [35] S. Hosseinpour, S. Fatemi, Y. Mortazavi, M. Gholamhoseini, and M. T. Ravanchi, "Performance of Cax Zeolite for separation of C₂H₆, C₂H₄, and CH₄ by adsorption process; capacity, selectivity, and dynamic adsorption measurements," *Sep. Sci. Technol.*, vol. 46, no. 2, pp. 349–355, 2011.
- [36] D. M. Ruthven, S. Farooq, and K. S. Knaebel, *Pressure Swing Adsorption*. VCH Publishers, 1994.
- [37] A. Gabelman, "Adsorption Basics: Part 1 | AIChE," 2017. [Online]. Available: <https://www.aiche.org/resources/publications/cep/2017/july/adsorption-basics-part-1>. [Accessed: 26-Sep-2018].
- [38] W. McCabe, J. C. Smith, and P. Harriot, *Unit Operations of Chemical Engineering*. McGraw-Hill Education, 2004.
- [39] P. M. Mathias and F. Corp, "Reactions and Separations," no. December, pp. 30–37, 2009.
- [40] P. Li. N N, *Recent Developments in Separation Science Volume 2*. Chapman and Hall/CRC, 2018.
- [41] J. E. Bachman *et al.*, "Enabling alternative ethylene production through its selective adsorption in the metal–organic framework Mn₂(m-dobdc)," *Energy Environ. Sci.*, vol. 11, no. 9, pp. 2423–2431, Sep. 2018.
- [42] J. A. Delgado, V. I. Agueda, M. A. Uguina, J. L. Sotelo, and P. Brea, "Hydrogen recovery from off-gases with nitrogen-rich impurity by pressure swing adsorption using CaX and 5A zeolites," *Adsorption*, vol. 21, no. 1–2, pp. 107–123, Feb. 2015.
- [43] I. T. Program, "Materials for Separation Technologies: Energy and Emission Reduction Opportunities," 2005.
- [44] A. Rivera Guerrero, "Desarrollo y aplicación de un modelo computacional

- del arranque y operacion de un proceso de adsorción por cambios oscilatorios de presión para la deshidratación de etanol azeotrópico,” National University of Colombia, 2014.
- [45] M. Mehdipour and S. Fatemi, “Modeling of a PSA-TSA process for separation of CH₄ from C₂ products of OCM reaction,” *Sep. Sci. Technol.*, vol. 47, no. 8, pp. 1199–1212, 2012.
- [46] D. M. (Douglas M. Ruthven, *Principles of adsorption and adsorption processes*. Wiley, 1984.
- [47] N. Wakao and J. M. Smith, “Diffusion in catalyst pellets,” *Chem. Eng. Sci.*, 1962.
- [48] O. Levenspiel, *Engineering Flow and Heat Exchange*. Boston, MA: Springer US, 2014.
- [49] S. Sircar and J. R. Hufton, “Why does the linear driving force model for adsorption kinetics work?,” *Adsorption*, vol. 6, no. 2, pp. 137–147, 2000.
- [50] A. Gorbach, M. Stegmaier, and G. Eigenberger, “Measurement and Modeling of Water Vapor Adsorption on Zeolite 4A—Equilibria and Kinetics,” *Adsorption*, vol. 10, no. 1, pp. 29–46, Jan. 2004.
- [51] AspenTech, *Aspen Adsim 12.1*. Cambridge: Aspen Technology, Inc., 2003.
- [52] K. R. Wood, Y. A. (Yih A. Liu, and Y. Yu, *Design, simulation and optimization of adsorptive and chromatographic separations : a hands-on approach*. .
- [53] “Pressure swing adsorption for the purification of hydrogen cláudia rubina spínola franco dissertação de mestrado apresentada à faculdade de engenharia da universidade do porto em engenharia química,” 2014.
- [54] D. Ko, R. Siriwardane, and L. T. Biegler, “Optimization of a Pressure-Swing Adsorption Process Using Zeolite 13X for CO₂ Sequestration,” *Ind. Eng. Chem. Res.*, vol. 42, no. 2, pp. 339–348, Jan. 2003.
- [55] “Anesthetic Structure Database.” [Online]. Available: <http://molfield.org/>. [Accessed: 08-Jul-2019].
- [56] N. Wakao and T. Funazkri, “Effect of fluid dispersion coefficients on particle-

- to-fluid mass transfer coefficients in packed beds: Correlation of sherwood numbers,” *Chem. Eng. Sci.*, vol. 33, no. 10, pp. 1375–1384, Jan. 1978.
- [57] “Transport phenomena, R. B. Bird, W. E. Stewart, and E. N. Lightfoot, John Wiley and Sons, Inc., New York(1960). 780 pages.\$11.50,” *AIChE J.*, 1961.
- [58] R. C. Reid, J. M. Prausnitz, and T. K. Sherwood, *The properties of gases and liquids, 4th ed.* 1987.
- [59] L. García *et al.*, “Adsorption separation of oxidative coupling of methane effluent gases. Mini-plant scale experiments and modeling,” *J. Nat. Gas Sci. Eng.*, 2019.
- [60] A. I. Sarker, A. Aroonwilas, and A. Veawab, “Equilibrium and Kinetic Behaviour of CO₂ Adsorption onto Zeolites, Carbon Molecular Sieve and Activated Carbons,” *Energy Procedia*, vol. 114, pp. 2450–2459, Jul. 2017.
- [61] W. J. Thomas and B. D. (Barry D. . Crittenden, *Adsorption technology and design.* Butterworth-Heinemann, 1998.
- [62] *,† Marco J. G. Linders, † Martijn B. L. van der Weijst, ‡ Jacques J. G. M. van Bokhoven, † and Freek Kapteijn, and J. A. Moulijn†, “Design of an Industrial Adsorption Process with Activated Carbon for the Removal of Hexafluoropropylene from Wet Air,” 2001.
- [63] M. Asgari, H. Anisi, H. Mohammadi, and S. Sadighi, “Designing a commercial scale pressure swing adsorber for hydrogen purification,” *Pet. Coal*, vol. 56, no. 5, pp. 552–561, 2014.
- [64] W. D. Seider, D. R. Lewin, J. D. Seader, S. (Chemical engineer) Widagdo, R. (Rafiqul) Gani, and K. M. Ng, *Product and process design principles : synthesis, analysis and evaluation.* .
- [65] H. J. Sandler and E. T. Luckiewicz, *Practical process engineering : a working approach to plant design.* McGraw-Hill B. Co, 1987.
- [66] S. Jain, A. S. Moharir, P. Li, and G. Wozny, “Heuristic design of pressure swing adsorption: A preliminary study,” *Sep. Purif. Technol.*, 2003.
- [67] L. M. Z. F. K. Volova, “Equilibrium of coexisting liquid and gas phases in the binary system methane - ethylene (in Russian),” vol. 14, no. 268, 1940.
- [68] R. (Chemical engineer) Smith, *Chemical process design and integration.*

- Wiley, 2005.
- [69] J. A. Delgado, M. A. Uguina, J. L. Sotelo, and B. Ruíz, "Modelling of the fixed-bed adsorption of methane/nitrogen mixtures on silicalite pellets," *Sep. Purif. Technol.*, vol. 50, no. 2, pp. 192–203, Jun. 2006.
- [70] S. Cavenati, C. A. Grande, and A. E. Rodrigues, "Separation of methane and nitrogen by adsorption on carbon molecular sieve," *Sep. Sci. Technol.*, vol. 40, no. 13, pp. 2721–2743, Oct. 2005.
- [71] Alibaba, "Zeolite Cax Zeolite Molecular Sieve - Buy Zeolite Cax, Zeolite Cax, Zeolite Cax Product on Alibaba.com." [Online]. Available: https://www.alibaba.com/product-detail/Zeolite-CaX-Zeolite-molecular-sieve_60012325363.html?spm=a2700.7724838.2017115.1.4aad1c67yEcpk. [Accessed: 22-Jun-2019].
- [72] D. Garred, "APPENDIX 1 EQUIPMENT COST ESTIMATES," 2012.
- [73] J. R. Couper, *Chemical process equipment : selection and design*. Elsevier/Butterworth-Heinemann, 2012.
- [74] R. Turton, J. A. Shaeiwitz, D. Bhattacharyya, and W. B. Whiting, *Analysis, synthesis, and design of chemical processes*. .
- [75] D. Ulrich and P. T. Vasudevan, "How to Estimate Utility Costs - Chemical Engineering | Page 1," 2016. [Online]. Available: <https://www.chemengonline.com/how-to-estimate-utility-costs/>. [Accessed: 23-Jun-2019].
- [76] Purity gas Canada, "Costs of nitrogen gas - how much should you be paying? | Purity Gas." [Online]. Available: <https://puritygas.ca/nitrogen-gas-costs/>. [Accessed: 23-Jun-2019].
- [77] ICIS, "OUTLOOK '19: New capacity may lengthen US ethylene, keep upstream costs volatile - ICIS Explore," 2019. [Online]. Available: <https://www.icis.com/explore/resources/news/2019/01/02/10300667/outlook-19-new-capacity-may-lengthen-us-ethylene-keep-upstream-costs-volatile/>. [Accessed: 16-Jun-2019].